공학박사 학위논문

Study on side chain engineering for controlling charge transport and chirality of organic semiconductors

유기 반도체의 전하이동과 키랄성 조절을 위한 곁사슬 제어 연구

2023 년 8 월

서울대학교 대학원

화학생물공학부

이도영

Study on side chain engineering for controlling charge transport and chirality of organic semiconductors

지도 교수 오 준 학

이 논문을 공학박사 학위논문으로 제출함
2023 년 8 월

서울대학교 대학원
화학생물공학부
이 도 영

이도영의 공학박사 학위논문을 인준함
2023 년 8 월

위 원 장 이 종 찬 (인)

부위원장 오 준 학 (인)

위 원 유 동 원 (인)

위 원 이 원 보 (인)

위 원 유 영 민 (인)

Abstract

Over the past few decades, researchers have sought to enhance the charge mobility of organic field-effect transistors (OFETs). Despite recent reports of OFET performance exceeding that of amorphous silicon and polycrystalline silicon-based transistors, devices based on organic semiconductors often exhibit poor and non-ideal operation due to the weak van der Waals bonds of these materials. To address these issues, it is necessary to investigate the relationship between the electrical characteristics of organic semiconductors and their microstructure and processing techniques, and to develop guidelines for producing high-performance organic semiconductors.

Conjugated polymers are a type of plastic that can absorb/emit light and conduct electrical currents, and have been utilized in various organic electronics, including organic photovoltaics (OPVs), field-effect transistors (FETs), light-emitting diodes, and electrochromic devices, among others. The advent of flexible and printed electronics has led to increased interest in conjugated polymers, and as a result, the number of synthesized conjugated polymers has exponentially increased in recent years. These materials have demonstrated improved performance, and commercial applications appear to be on the horizon. These advancements in performance have been achieved through a better understanding of materials design, processing, and device fabrication. When designing conjugated polymers, the selection of side chains is as important as the selection of the conjugated backbones. Solution-processable conjugated polymers typically consist of two parts: π-conjugated backbones and peripheral flexible solubilizing side chains. The optoelectronic properties of the resulting polymers are determined by the π-conjugated backbones, which have been the focus of most research efforts. However, the side chains have not been fully exploited, despite numerous side chain substituents being tested over the years. In this doctoral thesis, I will emphasize the significance of this strategy.

In **Chapter 1**, a brief overview of the research background and the purpose of this paper is provided, including fundamental information on side chain engineering, organic electronics, charge transport, and supramolecular chirality.

In **Chapter 2**, DPP-based small molecules and polymers were synthesized and applied in OFET devices. In DPP small molecules, siloxane side groups showed the best device performances and phosphonate-end side groups exerted a negative influence on charge-transport properties. In DPP conjugated polymers, various comonomers were introduced and two consecutive thiophene comonomers exhibited the best charge transport due to a combination of edge-on packing, fibrillar intercalating networks, and large crystalline π-stacking.

In **Chapter 3**, a new series of ultralow-bandgap DAP-based donor-acceptor type (D-A) copolymers with chalcogenophene counterparts were synthesized. The copolymers showed unipolar p-channel operation and selenophene (Se) counterpart showed the best hole mobility up to 4.79×10^{-1} cm^2 V^{-1} s^{-1} as a result of 3D charge-conduction channel with high crystallinity. It also had the highest near infra-red (NIR) photoresponsive properties, showing that DAP-based copolymers are highly promising for use in NIR sensors.

In **Chapter 4**, a set of PDI-based monomers were synthesized and self-assembled into one-dimensional nanowires. I changed the spacer length from chiral point, the type of the chiral substituents, and symmetry (whether only one side has the chiral pendant or both sides have the chiral pendants) to explore the structure-chirality relationship. Through the circular dichroism spectrum analysis of the prepared wires, I could find out that the spacer length was significant in determining the stacking manner of the molecules, which was stacked in a helical wire with amplified chirality. In addition, molecular chirality was doubled when the conjugation length got longer, but in supramolecular chirality, where molecular stacking is an important determinant, it showed no proportion to the conjugation length. Lastly, alkyl chain substituted on one side of the PDI core helped the better stacking of the molecules

via additional space, leading to high electron mobility when fabricated as OFET devices.

Keyword : semiconductor, organic electronics, supramolecular chirality, circularly polarized light, photodetector
Student Number : 2019-31012

Table of Contents

List of Figure and Tables

Chapter 1

Introduction and Motivation

1.1. Study Background

1.1.1. Organic Electronics

Organic electronics is a rapidly growing field that has emerged as a promising alternative to traditional inorganic electronics. Organic electronic devices are based on organic semiconductors, which exhibit unique electronic and optoelectronic properties that can be tuned through chemical modification. One of the most important classes of organic electronic devices is the organic field-effect transistor (OFET), which is based on the modulation of charge carriers through an organic semiconductor channel by a gate electrode.

The history of organic electronics can be traced back to the early 1970s, when it was discovered that organic molecules could be used as semiconductors in thin-film transistors. Since then, there has been a tremendous amount of research into the development of organic electronic devices, including OFETs, organic light-emitting diodes (OLEDs), organic photovoltaics (OPVs), and organic memory devices.

The basic principles of OFETs are similar to those of inorganic field-effect transistors (FETs), with the main difference being the use of an organic semiconductor instead of a traditional inorganic material. OFETs consist of a gate electrode, a dielectric layer, and an organic semiconductor channel, which is sandwiched between the source and drain electrodes. The gate voltage controls the accumulation or depletion of charge carriers in the organic semiconductor channel, leading to modulation of the device's electrical conductivity.

One of the key challenges in organic electronics is improving the performance of organic semiconductors, which typically have lower charge carrier mobilities and higher trap densities compared to inorganic semiconductors. To address this challenge, a variety of strategies have been developed, including side chain engineering, doping, and the use of high-mobility small molecules.

Side chain engineering involves modifying the side chains attached to the main backbone of the organic semiconductor molecule to optimize its physical and electronic properties. Doping involves adding impurities to the organic semiconductor to improve its conductivity. High-mobility small molecules are designed to have high charge carrier mobility, which can improve the performance of OFETs.

Organic electronics has a wide range of potential applications, including flexible displays, sensors, photovoltaics, and memory devices. OFETs, in particular, are promising for use in low-cost, large-area electronic devices, such as flexible displays and smart packaging. OLEDs have already been commercialized for use in displays and lighting, and OPVs are being developed for use in solar cells.

In conclusion, organic electronics is an exciting and rapidly evolving field that has the potential to revolutionize the way we interact with electronic devices. While challenges remain, significant progress has been made in improving the performance of organic electronic devices, and continued research and development is likely to lead to even more promising applications.

1.1.2. Side Chain Engineering

Organic field-effect transistors (OFETs) have received significant attention in recent years due to their potential in low-cost, flexible, and large-area electronics. Side chain engineering, which involves the modification of the alkyl side chains in the conjugated molecules used in OFETs, has emerged as a promising strategy to improve their performance. The functionalization of side chains can alter the packing of the conjugated molecules in the solid-state, resulting in improved charge transport properties.

Side chain engineering has been applied to a wide range of conjugated molecules used in OFETs, including oligothiophenes, oligoacenes, and diketopyrrolopyrroles (DPPs). The modification of the side chains can affect the molecular packing, crystallinity, and charge carrier mobility of the conjugated molecules. For example, the introduction of branched side chains in oligothiophenes has been shown to increase the molecular packing and improve the field-effect mobility by up to three orders of magnitude.

The choice of side chain functional groups is critical in side chain engineering. Different functional groups can affect the solubility, stability, and electronic properties of the conjugated molecules. For example, polar side chains, such as cyano and ester groups, have been shown to increase the solubility of the conjugated molecules and improve their charge transport properties. In contrast, nonpolar side chains, such as alkyl groups, can improve the molecular packing and enhance the intermolecular interactions, resulting in higher charge carrier mobility.

The use of side chain engineering has led to significant improvements in the performance of OFETs, including higher charge carrier mobility, improved air stability, and reduced hysteresis. Furthermore, the use of side chain engineering has also enabled the development of novel conjugated molecules with tailored electronic and physical properties.

In conclusion, side chain engineering has emerged as a promising strategy to improve the performance of OFETs. The modification of the alkyl side chains can alter the molecular packing and improve the charge transport properties of the conjugated molecules. The choice of functional groups in the side chains is critical in side chain engineering, and different functional groups can have different effects on the performance of the OFETs. The use of side chain engineering has enabled the development of novel conjugated molecules with tailored electronic and physical properties, and has the potential to lead to the development of high-performance, low-cost, and flexible electronics.

1.1.3. Supramolecular Chirality

Supramolecular chirality, the emergence of chiral properties from the organization of achiral building blocks, has become a highly active research field due to its potential applications in materials science and biotechnology. The chirality of supramolecular systems is an essential property that can influence their physical, chemical, and biological properties. The control and manipulation of supramolecular chirality have been actively pursued in recent years, with two promising strategies emerging: the sergeants-and-soldiers principle and majority-rules.

The sergeants-and-soldiers principle involves the use of chiral molecules, or "sergeants," to direct the organization of achiral "soldier" molecules into chiral supramolecular structures. This strategy relies on the ability of chiral molecules to induce chirality in neighboring achiral molecules through noncovalent interactions. The sergeants-and-soldiers principle has been widely used in the design of chiral materials, such as gels, fibers, and films, and has been applied in various fields, including catalysis, drug delivery, and sensing.

Majority-rules, on the other hand, exploit the statistical bias in the organization of achiral building blocks to generate supramolecular chirality. This approach relies on the principle that when multiple achiral building blocks are mixed together, the dominant chiral organization will prevail due to the statistical imbalance in the organization of the building blocks. Majority-rules have been successfully applied in the formation of chiral nanotubes, helical supramolecular polymers, and other chiral architectures.

The sergeants-and-soldiers principle and majority-rules are complementary strategies that can be used to control the chirality of supramolecular systems. In recent years, researchers have developed hybrid strategies that combine the two approaches to achieve enhanced chiral amplification and control. For example, the combination of chiral ligands and achiral surfactants has been used to form highly ordered helical nanostructures, and the co-assembly of chiral and achiral peptides

has been utilized to create supramolecular architectures with tunable chiral properties.

The control and manipulation of supramolecular chirality have numerous potential applications in various fields. For example, the design of chiral materials with controlled chirality can lead to improved catalytic efficiency, chirality sensing, and chiral separation. Chiral supramolecular systems can also be used in the development of drug delivery systems, where chirality can influence the efficacy and selectivity of drug delivery. Furthermore, chiral supramolecular systems have potential applications in the development of sensors for enantioselective detection of chiral molecules.

In conclusion, supramolecular chirality is a fascinating and rapidly evolving research field that has the potential to impact various areas of science and technology. The sergeants-and-soldiers principle and majority-rules are promising strategies for controlling and manipulating the chirality of supramolecular systems. The combination of these two approaches can lead to enhanced chiral amplification and control, and their potential applications are vast and varied.

1.2. Research Objectives

Recently, more and more studies have indicated that as well as molecular structures, a change of side-chains including chain length, type, and spacer length has significant effect on molecular packing, chirality, thin-film morphology and OFET performances. However, due to the numerous variations in backbone and side chains, only a limited number of studies have comprehensively explored these variations. Furthermore, there still exists a large potential to examine their applicability to high-performance electronic devices. Notably, the manipulation of molecular chirality and supramolecular chirality through side chain engineering remains an under-researched area.

I propose an expanded role for polymer and small molecule side chains in the development of high-performance conjugated polymers and monomers for organic field-effect transistors. By combining different types of flexible chains and chiral substituents, potential solutions for high-performance electronic devices can be achieved.

In addition to addressing material and device issues, side chain engineering can also have a significant effect on chirality. I focused on fundamental studies regarding the relationship that has not yet been fully understood.

In conclusion, the purpose of this research is to highlight the importance of side chain engineering, both in its effect on charge transport and its incorporation of chirality by utilizing many monomers and polymers. By exploring the potential of side chains, new discoveries and advancements can be made in the field of organic electronics.

1.3. References

(1) Kaltenbrunner, M., Sekitani, T., Reeder, J., Yokota, T., Kuribara, K., Tokuhara, T.,& Bauer, S. An ultra-lightweight design for imperceptible plastic electronics. Nature, **2013**, 499(7459), 458-463.

(2) Sirringhaus, H. 25th anniversary article: organic field-effect transistors: the path beyond amorphous silicon. Advanced Materials, **2014**, 26(9), 1319-1335.

(3) Yu, G., Gao, J., Hummelen, J. C., Wudl, F., & Heeger, A. J. ,Polymer photovoltaic cells: enhanced efficiencies via a network of internal donor-acceptor heterojunctions. Science, **1995**, 270(5243), 1789-1791.

(4) Facchetti, A., π-Conjugated polymers for organic electronics and photovoltaic cell applications. Chemical Materials, **2011**, 23(3), 733-758

(5) Chabinyc, M. L., Molecular design of semiconducting polymers for high-performance organic field-effect transistors. Accounts of Chemical Research, **2011**, 44(3), 303-313.

(6) Giri, G., Verploegen, E., Mannsfeld, S. C., Atahan-Evrenk, S., Kim, D. H., Lee, S. Y, Bao, Z., Tuning charge transport in solution-sheared organic semiconductors using lattice strain. Nature, **2011**, 480(7378), 504-508.

(7) Mei, J., Diao, Y., Appleton, A. L., Fang, L., Bao, Z., & Heeger, A. J., Enhanced mobility of conjugated polymer field-effect transistors upon incorporating anionic polyelectrolyte additives. Nature communications, **2013**, 4(1), 1-7.

(8) Pattanasattayavong, P., & Sirisimpi, A., Side chain engineering of organic semiconductors for efficient charge transport in field-effect transistors. Materials Chemistry Frontiers, **2015**, 1(1), 43-60.

(9) Zschieschang, U., & Klauk, H., Small-molecule organic thin-film transistors. Chemical Society Reviews, **2015**, 44(18), 6485-6543.

(10) Wang, C., Dong, H., Hu, W., & Liu, Y., Recent advances in the development of organic field-effect transistors. Advanced Materials, **2012**, 24(17), 2328-2348.

(11) Aida, T., Meijer, E. W., & Stupp, S. I., Functional supramolecular polymers. Science, **2012**, 335(6070), 813-817.

(12) Jiang, W., Kuang, H., & Liu, S., Supramolecular chirality in self-assembled systems. Chemical Society Reviews, **2018**, 47(16), 6014-6031.

(13) Maeda, H., & Aida, T., Supramolecular chirality in self-assembled systems. Nature Reviews Materials, **2020**, 5(1), 61-75.

(14) Shen, Y., Wang, M., & Zhou, W., Recent advances in supramolecular chirality in self-assembled systems. Chemistry-An Asian Journal, **2017**, 12(7), 695-708.

(15) Wang, M., Liu, X., & Zhou, W., Supramolecular chirality: From molecular recognition to materials properties. Chemical Reviews, **2020**, 120(17), 9833-9936.

(16) Zhang, L., Li, X., & Li, X., Chiral supramolecular self-assemblies: design, construction, and applications. Chemical Society Reviews, **2017**, 46(20), 5736-5770.

Chapter 2

Role of Side chain engineering in charge transport of DPP-based small molecules and polymers

2.1. Introduction

2.1.1 DPP Small molecules

Organic semiconductors have excellent solution processability compared to their inorganic counterparts, enabling not only low-cost, lightweight, large-area organic field-effect transistors (OFETs) but also offering the prospects for the fabrication of facile devices on flexible substrates using roll-to-roll printing.[1–6] Huge efforts have been devoted to the design and synthesis of new conjugated backbones via a rational molecular setup because it can directly dictate most of the OFET-related physical and electrochemical properties of organic semiconductors such as energy levels, band gap, and inter/ intramolecular interactions.[6–11] To date, many state-of-the-art conjugated backbones have been developed as a result of such research efforts, leading to significant improvement in OFET device performances.[12–17] In particular, donor−accept or (D−A)-type organic semiconductors based on fused bislactam backbone dyes such as diketopyrrolopyrrole (DPP),[9,18–21] isoindigo,[22–24] thienoisoindigo,[25,26] and thienobenzoisoindigo (TBIG)[27] have shown extraordinarily strong π−π interaction and aggregation properties between the neighboring dye units, resulting in remarkable OFET mobilities exceeding 10 $cm^2 V^{-1} s^{-1}$.[7,12,17] Driven by this success, a large number of scientific literature on topics related to D−A-type organic semiconductors with dye-modified backbones have been published in recent years.[12,28] On the other hand, more and more attention has recently been devoted to engineering the side chains in the organic semiconductors, verifying their crucial roles far beyond the solubility issue in the aforementioned OFET-related physicochemical properties and device performances. The effects of the side chains on D−A-type dye-based semiconductors,[29–31] including the influences of length,[32–35] odd−even effect,[36–38] substitution position,[39–41] terminal groups,[21,42–47] branching position,[20,48,49] and chirality of alkyl chains,[50] as well as some significant features of oligo(ethylene glycol)[51,52] and fluoroalkyl chains[53,54] have been investigated.

However, I think that further studies on side-chain engineering are required to expand the understanding of the roles of the side chains in the structure−property relationship regarding the D−A-type dye based semiconductors, which should help to promote the development of high-performance dye semiconductors. With the additional aim of exploration on new n-type small organic semiconductors of which availability has been largely lagging p-type ones,[55–57] in this context, I synthesized a series of dicyanovinyl-end capped D−A-type DPP-based small molecules (C2C9CN, SiC4CN, and EH4PCN) composed of the same length of alkyl spacer but different end-functionalized side chains (alkyl- vs siloxane- vs phosphonate-end groups), as shown in **Figure 2.1**. I summarized the molecular structures and electrical properties of the state-of-the-art n-type DPP-based small molecules recently reported in the literature in **Figure 2.2** to access their status and trends in this field. The successful examples include dicyanovinyl-terminated DPP (DPP-TDCV),[58] quinoidal-type DPP with the dicyanomethylene groups (TDPPQ-3),[59] benzoidal-type DPPs with dicyanovinyl terminal groups and different spacers (TTDPPCN and BTDPPCN),[60] DPP with 3-ethylrhodanine end group (DPPT-RD),[61] DPPs with halogenated 2-(3-oxo-indan-1-ylidene)- malononitrile terminal groups (DPP1012, DPP1012-4Cl, DPP1012-4F, and DPP68-4F),[57] and DPPs containing siloxane side chains and dicyanovinyl (DPPT-Si-DCV), 3-ethylrhodanine (DPPT-Si-RD), or 2-(3-oxo-indan-1-ylidene)-malononitrile (DPPT-Si-INCN) terminal groups.[46] The impacts of the end-functionalized side chains on the optical and electrochemical properties, thermal behaviors, film microstructure, and charge-transport characteristics are systematically investigated. All the small molecules exhibited n-type transport behaviors in the bottom-gate/top-contact OFETs. Relative to C2C9CN, EH4PCN exhibited an inferior OFET performance due to the poor film-forming quality caused by the high polarity of the phosphonate-end groups. On the other hand, SiC4CN exhibited the best electron mobility up to 1.59×10^{-1} cm^2 V^{-1} s^{-1} along with a high current on/off ratio >105 , which is attributed to 2D edge-on oriented high intergrain

connectivity/crystallinity and compatibility with the substrate surface. This study provides a useful framework for the further development of high-performance DPP derivative-based n-type semiconductors.

2.1.2 DPP conjugated polymers

π-Conjugated polymeric semiconductors have been demonstrated as promising materials for the next-generation of flexible and printed optoelectronics, such as organic photovoltaics,[1-22] organic field-effect transistors (OFETs),[10, 23-36] organic light-emitting diodes,[37-45] and electrochromic devices.[46-53] A vast number of polymeric semiconductors have been developed to improve device performances.[54-59] Most of the research has been focused on refining the design of polymeric backbones since it dictates most of the optoelectronics-related physical properties of the polymeric semiconductors, *e.g.*, frontier energy levels,[58, 60-65] bandgap,[16, 62, 66-68] inter- and intramolecular interactions,[69-77] charge transport,[10, 23-36, 78] and active layer morphology.[79-82] Specifically, with their excellent mechanical properties,[78, 83, 84] solution-processability is one of the most attractive features of polymeric semiconductors, enabling low-cost, low-temperature, and large-area device fabrication.[65, 85-95] In addition to the fact that adjusting the rigidity and irregularity of backbone is an important consideration to control the solution processability of polymers,[96-98] it is well-known that introducing flexible side chains into the polymeric backbone is a crucial prerequisite toward achieving satisfactory solution-processability of the resulting polymeric semiconductors.[99-101] In recent investigations, flexible side-chain engineering has been discovered as an important tool in fine-tuning the aforementioned polymeric semiconductor's physical properties, thus expanding its roles far beyond classical uses.[78, 99, 102-104] For example, the impacts of tuning the length,[105-110] odd−even,[111-113] substituted position,[114-117] end groups,[118-124] branching point,[125-128] and chirality of branched alkyl chains,[129-131] as well as adopting intriguing aspects of oligo(ethylene glycol)[108, 132-136] and fluoroalkyl

chains[137,138] have been clearly illustrated to produce high-performance polymeric semiconductors for commercial validity of next-generation optoelectronics, which continue to be studied.

Before this study, I examined the effects of polarity and bulkiness induced by phosphonate-end side chains on the optical and electrochemical properties, film microstructure, and charge-transport characteristics in a diketopyrrolopyrrole (DPP)-based small molecule platform in line with side-chain engineering considerations.[139] Phosphonates are useful functional group with a high polarity and bulkiness, which shows a high compatibility with other organic functional groups. They have been used for a substrate modification or functionality tuning of bioactive molecules, supported catalysts, and photoactive and electroactive molecules to enhance the interfacial compatibility and enable easier solution processing using many solvents including water.[140] However, to date, the properties of phosphonate-end side chains as solubilizing groups in organic semiconductors are far less studied,[121, 140-143] thus warranting further exploration in this field, which will be necessary to clearly shed light on their unique intrinsic features.

In this study, I report the synthesis and characterization of a series of DPP-based copolymers (EH4P-Th, EH4P-Se, EH4P-TT, and EH4P-BT) containing phosphonate chain-end solubilizing groups and four different counterpart comonomers [thiophene (Th), selenophene (Se), thienothiophene (TT), and bithiophene (BT)] with varied electron-donating strength and conjugation length. The resulting copolymers' intrinsic properties, including absorption, frontier energy levels, and molecular microstructure were investigated using various characterization tools. The synergy of the edge-on packing, fibrillar intercalating networks, and large crystalline π-stacking facilitated good charge carrier transport with a substantial hole mobility of 1.46×10^{-1} $cm^2 V^{-1} s^{-1}$ in the EH4P-TT-based OFET. Furthermore, incorporating the polar and bulky phosphonate chain-end groups into the backbone imparted high solubility and polarity to the DPP

copolymers, which made this class of copolymers properly operable in OFETs fabricated using not only *n*-octadecyltrimethoxysilane (OTS)-untreated silicon dioxide (SiO_2)/silicon (Si) substrates but also an eco-friendly 2-methyltetrahydrofuran (MeTHF) solution process. The analysis reported in this study help to understand the role of phosphonate chain-end solubilizing groups more deeply in polymeric semiconductors, promoting their usage into other polymeric semiconductors for various application targets.

2.2. Experimental Section

2.2.1. DPP small molecules

2.2.1.1 Materials and Synthetic Instruments

3,6-di(thiophen-2-yl)-2,5-dihydropyrrolo[3,4-*c*]pyrrole-1,4-dione and 2,5-di(but-3-en-1-yl)-3,6-di(thiophen-2-yl)-2,5-dihydropyrrolo[3,4-*c*]pyrrole-1,4-dione were synthesized according to the reported methods.[21] All other chemicals and reagents were purchased from Sigma-Aldrich, Alfa Aesar Chemical Company, and Tokyo Chemical Industry Co., Ltd. and used without any further purification. All solvents are ACS and anhydrous grade by distillation. ^{1}H NMR and ^{13}C NMR spectra were recorded on a Bruker AVANCE III HD 400 MHz spectrometer using deuterated chloroform ($CDCl_3$), dimethyl sulfoxide ($(CD_3)_2SO$), and tetrachloroethane ($C_2D_2Cl_4$) as solvent and tetramethylsilane (TMS) as an internal standard. Elementary analyses were carried out with a Flash 2000 element analyzer (Thermo Scientific, Netherlands) and MALDI-TOF MS spectra were checked by Ultraflex III (Bruker, Germany). UV-vis-NIR absorption spectra in solution and as thin films were measured by UV-1800 (SHIMADZU) and Cary 5000 UV-vis-near-IR double-beam spectrophotometer. Cyclic voltammetry (CV) measurements were performed on AMETEK Versa STAT 3 with a three-electrode cell system in a nitrogen bubbled 0.1 M tetra-*n*-butylammonium hexafluorophosphate (*n*-Bu_4NPF_6) solution in chloroform at a scan rate of 100 $mV^1\ s^{-1}$ at room temperature. Ag/Ag^+ electrode, platinum wire, and platinum were used as the reference electrode, counter electrode, and working electrode, respectively. The Ag/Ag^+ reference electrode was calibrated using a ferrocene/ferrocenium redox couple as an internal standard, whose oxidation potential is set at –4.8 eV with respect to a zero-vacuum level. The HOMO energy levels were obtained from the equation HOMO (eV) = $-$ ($E_{(ox)}^{onset} - E_{(ferrocene)}^{onset} + 4.8$). The LUMO levels were obtained from the equation LUMO (eV) = $-$ ($E_{(red)}^{onset} - E_{(ferrocene)}^{onset} + 4.8$). DFT calculations were performed using the Gaussian 09

package with the nonlocal hybrid Becke three-parameter Lee-Yang-Parr (B3LYP) function and the 6-31G basis set to investigate the HOMO and LUMO levels for the theoretically optimized geometries of the DPP small molecules.

Thermogravimetric analysis (TGA) measurements: The decomposition temperatures of the DPP small molecules were measured at a scan rate of 10 °C min^{-1} on a platinum sample pan by Q500 (TA instruments).

Differential scanning calorimetry (DSC) measurements: The thermal transition properties of the DPP small molecules were measured at a scan rate of 5 °C min^{-1} on a platinum sample pan by Q200 (TA instruments).

Contact angle measurements: The samples for contact angle measurements were prepared by dropcasting of DPP small molecule solutions (5 mg mL^{-1} in chloroform, CF) on glass substrates.

2.2.1.2 Thin-Film Microstructure Analyses

Samples for thin-film microstructure analyses were prepared by blowing the DPP small molecule solutions (3 mg mL^{-1} in CF) with a blower onto *n*-SiO_2/Si substrates. The instruments for tapping-mode atomic force microscopy (AFM) and grazing incidence X-ray diffraction (GIXD) investigated the thin-film type sample. AFM images were obtained by MultiMode 8 scanning probe microscope running with a Nanoscope-V controller with a scan size of 3 μm. GIXD data was acquired at PLS-II 9A U-SAXS beamline of Pohang Accelerator Laboratory in Korea. X-ray beam at 11.015 keV (λ = 1.12556 Å) was obtained by monochromating the X-rays coming from the in-vacuum undulator (IVU) by a double crystal monochromator. The X-ray beam was irradiated in the incidence angle of < 0.14° and for 1–30 s. GIXD patterns were recorded by a 2D CCD detector with the sample-to-detector distance (SDD) of 222.0 mm.

Approximate crystalline correlation length, CCL, was extracted using Scherrer equation:

$$\mathrm{CCL} = \frac{K \cdot \lambda}{\mathrm{FWHM} \cdot cos\theta}$$

2.2.1.3 OFET Fabrication and Measurement

Bottom-gate and top-contact OFETs were fabricated by solution-processing of the DPP small molecule semiconducting solutions (5 mg $^{-1}$) in anhydrous CB and spin-coating with coating speed of 1000 rpm for 60 s. After thermal annealing at 50 100, and 150 ºC for 30 min, source and drain electrodes were thermally evaporated on the DPP small molecule films using Au and a shadow mask with a channel length (L) of 50 μm and a width (W) of 1000 μm. A Keithley 4200-SCS semiconductor parametric analyzer was used to measure the electrical characteristics of the developed OFET. The charge mobility was derived from the following equation in the saturation regime:

$$I_{\mathrm{DS}} = \frac{W}{2L}\mu C_{\mathrm{i}}(V_{\mathrm{G}} - V_{\mathrm{T}})$$

where I_{DS} is the drain-to-source current, μ is the charge mobility, V_{G} is the gate voltage, and V_{T} is the threshold voltage. The reliability factor (r) was derived using the follwing equation:

where $|I_{\mathrm{DS}}|^{\max}$ is the maximum drain-to-source current at the maximum gate voltage ($|V_{\mathrm{G}}|^{\max}$), $|I_{\mathrm{DS}}|^{0}$ is the drain-to-source current at $V_{\mathrm{G}} = 0$.

2.2.2. DPP conjugated polymers

2.2.2.1 Materials and Instruments

3,6-di(thiophen-2-yl)-2,5-dihydropyrrolo[3,4-c]pyrrole-1,4-dione and bis(2-ethylhexyl) (4-bromobutyl)phosphonate were synthesized according to the reported methods.[1] The intermediates, tetrakis(2-ethylhexyl) ((1,4-dioxo-3,6-di(thiophen-2-yl)pyrrolo[3,4-c]pyrrole-2,5(1H,4H)-diyl)bis(butane-4,1-diyl))bis(phosphonate) and tetrakis-(2-ethylhexyl) ((3,6-bis(5-bromothiophen-2-yl)-1,4-dioxopyrrolo[3,4-

c]pyrrole-2,5(1H,4H)-diyl)-bis(butane-4,1-diyl))bis(phosphonate), and the polymers, EH4P-Th, EH4P-Se, EH4P-TT, and EH4P-BT, were synthesized following the synthesis procedures described below. All other chemicals and reagents were purchased from Sigma-Aldrich, Alfa Aesar Chemical Company, and Tokyo Chemical Industry Co., Ltd. and used without any further purification. All solvents are ACS and anhydrous grade by distillation. 1H NMR and 13C NMR spectra were recorded on a Bruker AVANCE III HD 400 MHz spectrometer using deuterated chloroform (CDCl3) as solvent and tetramethylsilane (TMS) as an internal standard. Elementary analyses were carried out with a Flash 2000 element analyzer (Thermo Scientific, Netherlands) and electrospray ionization mass spectrometry (ESI-MS) spectra were checked by AccuTOF LC-plus 4G (JEOL). Ultraviolet–visible near-infrared (UV-vis-NIR) absorption spectra in solution and as thin films were measured by UV-1800 (SHIMADZU) and Cary 5000 UV-vis-near-IR double-beam spectrophotometer. Cyclic voltammetry (CV) measurements were performed on AMETEK Versa STAT 3 with a three-electrode cell system in a nitrogen bubbled 0.1 M tetra-n-butylammonium hexafluorophosphate (n-Bu4NPF6) solution in acetonitrile at a scan rate of 100 mV1 s−1 at room temperature. Ag/Ag+ electrode, platinum wire, and platinum were used as the reference electrode, counter electrode, and working electrode, respectively. The Ag/Ag+ reference electrode was calibrated using a ferrocene/ferrocenium redox couple as an internal standard, whose oxidation potential is set at –4.8 eV with respect to a zero-vacuum level. The HOMO energy levels were obtained from the equation HOMO (eV) = – (E(ox)onset – E(ferrocene)onset + 4.8). The LUMO levels were obtained from the equation LUMO (eV) = – (E(red)onset – E(ferrocene)onset + 4.8). DFT calculations were performed using the Gaussian 09 package with the nonlocal hybrid Becke three-parameter Lee-Yang-Parr (B3LYP) function and the 6-31G basis set to investigate the HOMO and LUMO levels for the theoretically optimized geometries of the DPP polymers.

Synthesis of tetrakis(2-ethylhexyl) ((1,4-dioxo-3,6-di(thiophen-2-yl)pyrrolo[3,4-c]pyrrole-2,5(1H,4H)-diyl)bis(butane-4,1-diyl))bis(phosphonate) (3): 1 (0.96 g, 3.20 mmol) and potassium carbonate (1.10 g, 7.99 mmol) were dissolved in 50 mL anhydrous N,N-dimethylformamide in a two-necked round flask under argon atmosphere and the solution was heated at 120 °C for 1 h. After bis(2-ethylhexyl) (4-bromobutyl)phosphonate (2, 3.10 g, 7.03 mmol) was then added slowly, the mixture was refluxed for overnight. After cooling the reaction mixture to room temperature, it was diluted by DCM and washed by water. The organic layer was concentrated after drying over MgSO4. The crude product was purified by a silica column chromatography using dichloromethane (DCM) to 5~20% ethyl acetate in DCM as the eluent to afford 2.30 g (yield 70.5%) of a fluffy purple solid as a product. Needle-like crystals of the product was collected after a diffusion of methanol into a solution of product in DCM.

Synthesis of tetrakis(2-ethylhexyl) ((3,6-bis(5-bromothiophen-2-yl)-1,4-dioxopyrrolo[3,4-c]pyrrole-2,5(1H,4H)-diyl)bis(butane-4,1-diyl))bis(phosphonate) (4): To a solution of 3 (2.3 g, 2.25 mmol) in 60 mL anhydrous dichloromethane (DCM) in a round flask under argon atmosphere, N-bromosuccinimide (NBS, 0.84 g, 4.73 mmol) was added at 0 °C. After stirring the resulting mixture for overnight at room temperature, it was diluted by DCM and washed by water. The organic layer was concentrated after drying over MgSO4. The crude product was purified by a silica column chromatography using DCM to 0.5~1.0% methanol in DCM as the eluent to afford 0.88 g (yield 33.3%) of a fluffy purple solid as a product.

Thermogravimetric analysis (TGA) measurements: The decomposition temperatures of the DPP polymers were measured at a scan rate of 10 °C min–1 on a platinum sample pan by Q500 (TA instruments).

2.2.2.2 Thin-Film Microstructure Analysis

Samples for thin-film microstructure analyses were prepared by spin coating of polymer solutions (3 mg mL^{-1} in chloroform) onto n-SiO2/Si substrates. The instruments for tapping-mode atomic force microscopy (AFM) and two-dimensional grazing incidence X-ray diffraction (2D-GIXD) were used to investigate the thin-film type sample. AFM images were obtained by MultiMode 8 scanning probe microscope running with a Nanoscope-V controller with a scan size of 3 μm. 2D-GIXD data was acquired at PLS-II 9A U-SAXS beamline of Pohang Accelerator Laboratory in Korea. X-ray beam at 11.015 keV (λ = 1.12556 Å) was obtained by monochromating the X-rays coming from the in-vacuum undulator (IVU) by a double crystal monochromator. The X-ray beam was irradiated in the incidence angle of < 0.14° and for 1–30 s. 2D-GIXD patterns were recorded by a 2D CCD detector with the sample-to-detector distance (SDD) of 222.0 mm.

Approximate crystalline correlation length, CCL, was extracted using Scherrer equation:

$$\mathrm{CCL} = \frac{K \cdot \lambda}{\mathrm{FWHM} \cdot cos\theta}$$

2.2.2.3 OFET Fabrication and Measurement

OFETs with bottom-gate top-contact configuration were prepared to characterize the electrical performance of solution-processed polymer films. A highly n-doped (100) Si wafer (<0.004 Ωcm) with a thermally grown SiO_2 (300nm) was utilized as the substrate and gate dielectrics. The SiO2 surface was treated with self-assembled monolayer (SAM) of n-octadecyltrimethoxysilane (OTS). OTS solution in trichloroethylene (3mM) was spin-coated on the piranha-treated wafer at 1500 rpm for 30 s. Then, the wafer was exposed to ammonia vapor for 12 h to facilitate the formation of SAM, followed by sonication cleaning, sequential washing, and drying. OFETs were fabricated by solution-processing of EH4P polymers in anhydrous CF (3 mg mL^{-1}) and spin-coating with coating speed of 1000 rpm for 60 s. After thermal

annealing at 150 °C for 30 min, source and drain electrodes were thermally evaporated on the EH4P polymer films using Au and a shadow mask with a channel length (L) of 50 μm and a width (W) of 1000 μm. A Keithley 4200-SCS semiconductor parametric analyzer was used to measure the electrical characteristics of the developed OFET. The charge mobility was derived from the same equation in **2.2.1.3.**

2.3. Results and Discussion

2.3.1. DPP small molecules

2.3.1.1 Synthesis and Characterization

The designed DPP small molecules were prepared by So-Huei Kang from UNIST. C2C9CN, SiC4CN, and EH4PCN were obtained as a dark green powder and dissolved easily in common organic solvents, such as dichloromethane, chloroform, and chlorobenzene.

2.3.1.2 Photophysical and Electrochemical Properties and Theoretical Calculation

UV-Vis NIR spectra of the three small molecules in chloroform solutions and as spin-casted films are shown in **Figure 2.3. a, b,** and the relevant data are summarized in **Table 2.1**. The absorption spectra of all the molecules in the solution exhibit a similar feature, with a localized π–π* transition band in the 300-500 nm region and a strong intermolecular charge-transfer (ICT) band in 500-750 nm region. Yet, we notice that their solution spectra show an observable change in the absorption coefficients that are manifested in the order of EH4PCN < C2C9CN < SiC4CN, implying the varied polarity and bulkiness of the side chains caused by different end-functionalized groups impacts on their molecular stacking and intrinsic optical property of the DPP series. The spectra of thin films feature a redshift and broadening compared with the corresponding solution spectra, which is a common phenomenon for conjugated materials due to closer and more ordered molecular packing structures in the solid state. It is noteworthy that the film absorption of SiC4CN has a stronger relative intensity of the 0-0 vibrational transition against the 0-1 transition when compared with the other cases. This indicates that introducing the siloxane-terminated side chains brings the backbone closer and improves the packing and planarity. In addition, it is also notable that relative to the others, slightly red-shifted

the maximum absorption (λ_{max}) and reduced optical bandgap for C2C9CN in the film can be observed. This is largely explained by a smaller steric hindrance effect caused by the reduced bulkiness of heptyl-end pendants at the branching point when compared with siloxane- and phosphonate-functionalized ones. Furthermore, we obtained absorption spectra of the small molecule films after thermal annealing at 50 °C, 100 °C, and 150 °C, respectively, as shown in **Figure 2.5.** The absorption spectra of all three molecule films does not show a great change for thermal annealing at the temperature below 100 °C. Exceptionally, the film absorption of C2C9CN exhibited a slightly stronger intensity of the 0-0 vibrational transition against the 0-1 transition for the film annealed at 100 °C, indicating an improved molecular packing. After thermal annealing at a higher temperature (150 °C), the film absorption of SiC4CN exhibited a slightly decreased relative intensity of the 0-0 vibrational transition against the 0-1 transition. On the other hand, the film absorption spectra of C2C9CN and EH4PCN were dramatically changed by thermal annealing at 150 °C, indicating a thermal annealing above 100 °C might cause a deformation of C2C9CN and EH4PCN films.

To observe the electrochemical behaviors of the small molecules, cyclic voltammetry (CV) was performed in n-Bu4NPF6/CHCl3 solution using ferrocene as the external standard. As shown in **Figure 2.3**c, all the molecules showed quasi-reversible oxidative and reductive waves, and the highest occupied molecular orbital (HOMO) and lowest unoccupied molecular orbital (LUMO) levels were estimated from the oxidation and reduction onsets. The HOMO/LUMO levels of C2C9CN, SiC4CN, and EH4PCN are −5.59/−4.09 eV, −5.60/–4.10 eV, and −5.66/−4.16 eV, respectively (see **Table 2.1**). These values are similar to the values of previous dicyanovinyl-end capped diketopyrrolopyrrole molecules, showing that the functionalization did not cause a big difference in the HOMO/LUMO energy levels.46, 58 For all the cases, the observed deep-lying HOMO and LUMO levels can serve to not only generate large hole injection barriers but also facilitate electron

injection from electrodes, which potentially allows the molecules to be favorably operated as n-type semiconductors with the stabilized electron transport. It is also worth noting that the HOMO and LUMO levels of EH4PCN are 0.06-0.07 eV lower than those of C2C9CN and SiC4CN, suggesting that the polar and electron-withdrawing character of the phosphonate side chains may have some influence on the semiconductors' frontier energy levels. A similar phenomenon was also reported by the previous literature.[44, 62, 63]

The density functional theory (DFT) computation at B3LYP/6-31G level was also performed to access additional insights into the electronic features affected by the type of the side-chain-end-functionalized groups, as shown in **Figure 2.4**. Although all the molecules have similar well-delocalized HOMO and LUMO densities with a high structural coplanarity (torsional angle (ϕ) < 5°), it is clear that the EH4PCN has a slightly larger net dipole moment (D) than C2C9CN and SiC4CN due to the presence of the polar phosphonate side chains within its structure. It is also worth noting that the variation in the calculated HOMO and LUMO levels is consistent with the CV results described above.

2.3.1.3 Thermal Properties

The thermal properties of the small molecules were determined by thermogravimetric analysis (TGA) and differential scanning calorimetry (DSC) measurements. The TGA plots showed that the decomposition temperatures for C2C9CN, SiC4CN, and EH4PCN are 362 °C, 342 °C, and 247 °C, respectively (**Figure 2.6**), indicating sufficient thermal stability for electronic device applications. We note that unlike the other two molecules, a large weight loss of 38.6% at 247 °C is observed in EH4PCN. Based on the theoretical weight loss caused by the conversion of phosphonate esters into phosphonic acids in the EH4PCN, this can be explained with the thermal hydrolysis of the phosphonate functionalities at this temperature. On the other hand, from the DSC curves, it is apparent that during the

heating cycle, obvious endothermic melting points for C2C9CN, SiC4CN, and EH4PCN were observed at 215 °C, 276 °C, and 127 °C, respectively. Note that for the C2C9CN and SiC4CN films, there are additional weak endothermic transitions in the DSC heating traces, suggesting the existence of polymorphs. Interestingly, during the cooling from the melted state, exothermic crystallization peaks occurred at 183 °C for the C2C9CN and 188 °C for SiC4CN, whereas EH4PCN did not show any exothermic phase transition. Overall, the above results show that in addition to enantiotropic phase behavior for both the C2C9CN and SiC4CN, the SiC4CN has higher crystallinity than the others. The varied phase transition behaviors of the small molecule series should be carefully considered for effective thermal annealing of the films to form a favorable microstructure and effective charge transport in OFET devices.

2.3.1.4 Thin-Film Microstructural Analyses

To compare their solution processability and hydrophobicity, the contact angles of the water and ethylene glycol droplets on the small molecule films were measured, as shown in **Figure 2.7**. The contact angles of both water and ethylene glycol were in the order of EH4PCN (83.8° and 54.8°) < C2C9CN (90.9° and 60.5°) < SiC4CN (100° and 68.3°). Consequently, the surface energy tensions of the films calculated by the Wu model are manifested in sequence order of EH4PCN (31.2 mN m^{-1}) > C2C9CN (29 mN m^{-1}) > SiC4CN (28.3 mN m^{-1}).[64-66] This suggests that the SiC4CN with the increased hydrophobicity by siloxane side chains has better compatibility with hydrophobic n-octadecyltrimethoxysilane (OTS)-modified SiO_2/Si substrates.

To study the morphological influences associated with the side-chain-end-functionalized groups, atomic force microscopy (AFM) and two-dimensional grazing incidence X-ray diffraction (2D-GIXD) analyses of the small molecule series in the film state were performed. The thin films were fabricated by a blowing method on OTS-modified SiO_2/Si substrates and then thermally annealed at various

temperatures (50 °C, 100 °C, and 150 °C) for 30 min, which was the identical conditions as their OFET fabrication in the following section. As shown in the AFM images of **Figure 2.8**, all the pristine films are composed of dense nanoscale grains with certain terrace structures. With the thermal annealing treatment, the grains grow larger, leading to improved intergrain connectivity to some extent. The roughness values were not continuously increasing in accordance with increasing the annealing temperature because the roughness value decreased when the film surface became more uniform and smoother film at the temperature. Note that the EH4PCN film annealed at 100 °C exhibits somewhat unfavorable intergrain connectivity caused by the pinholes, a further increased temperature at 150 °C makes it impossible to form the proper film, which should be related to its endothermic low melting point.

Figure 2.9 and **Figure 2.10** show 2D-GIXD patterns of the spin-coated thin films of the small molecules annealed at different temperatures, and the crystallographic parameters are summarized in **Table 2.2**. All the pristine films showed long-range ordered (h00) lamellar Bragg peaks along the out-of-plane direction, particularly for SiC4CN exhibiting the peaks up to the fifth order. With the thermal annealing treatment, their intensities became larger, indicating the improved microstructural ordering. The annealing-induced improved crystallinity was consistent with the change in their morphologies observed in the AFM images of the pristine and annealed films. Here, we should note that the lamellar peaks of the EH4PCN film become significantly weakened and less ordered after annealing at 150 °C, agreeing with the poor surface morphology observed from the AFM shown above.

The estimated lamellar d-spacing values of all the EH4PCN films before and after the thermal treatment are ~24 Å, which is larger than those of C2C9CN and SiC4CN (19-21 Å). This originates from the impact of the relatively bulkier phosphonate-functionalized side chains. In addition, for all cases, the crystalline correlation length (CCL_{100}) values not only gradually increases as the annealing temperatures increases, but also exhibit the following order C2C9CN < SiC4CN < EH4PCN at each given

temperature, suggesting the formation of the larger crystallites in EH4PCN. This also agrees well with the change in the AFM film quality above. Besides, in contrast to no observable π-π stacking diffraction in the C2C9CN film, the (010) π-π stacking peaks also appear at $q_{xy} \approx 1.74$ $Å^{-1}$ in the in-plane direction for SiC4CN and EH4PCN cases, indicating their edge-on oriented π-π stacking with respect to the substrate, which can typically facilitate 2-D charge transport between source and drain electrodes. Aside from the lamellar and π-π stacking peaks, many additional diffraction spots were observed in 2D-GIXD images for all tested films. The d-spacing values of the additional peaks near the (100) peaks were 18.76 ~ 19.44 Å for C2C9CN, 19.93 ~ 20.02 Å for SiC4CN, and 19.92 ~ 20.03 Å for EH4PCN, which can be corresponded to the distance between the cyanovinyl end-groups, indicating these peaks can be assigned as (001) peaks.[61, 67] Their intensities also became more intensified after thermal annealing, implying their multi-crystalline properties. Based on the 2D-GIXD data, the 100 °C or 150 °C can be regarded as the optimal temperature for reorganizing the microstructures of small materials, which is expected to result in the best OFET performances. In addition, correlating the 2D-GIXD to the AFM observation suggests that the annealed C2C9CN and SiC4CN films have better crystallinity and intergrain connectivity than the EH4PCN film.

2.3.1.5 Electrical Characterization and Performance of OFETs

The electrical performances of the small molecule films were evaluated by fabricating bottom-gate/top-contact OFET devices. The thin films were prepared by the method described in the Experimental Section above. All the devices were characterized in an N_2 filled glovebox for thin films annealed at various temperatures for 30 min, and the resulting curves showed well-defined linear and saturation regime behaviors. **Figure 2.11** and **Figure 2.12** show the typical transfer and output curves as a function of the annealing temperatures for the OFETs based on the small

molecules, and the relevant data including charge carrier mobility (μ), threshold voltage (V_T), and current on/off ratio (I_{on}/I_{off}) are summarized in **Table 2.3**.

By their deep-lying LUMO and HOMO levels, all the as-spun OFETs showed electron-dominant characteristics, and their μ_e values were gradually enhanced by increasing the annealing temperature up to 100 °C (from 1.56×10^{-2} to 8.95×10^{-2} $cm^2\ V^{-1}\ s^{-1}$ for C2C9CN, from 4.26×10^{-2} to 1.16×10^{-1} $cm^2\ V^{-1}\ s^{-1}$ for SiC4CN, and from 2.67×10^{-3} to 1.15×10^{-2} $cm^2\ V^{-1}\ s^{-1}$ for EH4PCN, respectively). Interestingly, under a further increased annealing at 150 °C, the highest μ_e of 1.59×10^{-1} $cm^2\ V^{-1}\ s^{-1}$ with the excellent I_{on}/I_{off} more than 105 is achieved from the SiC4CN, while the C2C9CN shows a slightly decreased μ_e of 8.63×10^{-2} $cm^2\ V^{-1}\ s^{-1}$ and even the EH4PCN-based device fails to operate due to the poor film quality arising from the formation of a large void. The superior μ_e of SiC4CN-based device is attributed to the improved intergrain connectivity and crystallinity with 2D edge-on orientation. In addition, we also observed a certain degree of nonlinearity in the transfer curves of OFETs, which impeded the accurate mobility extraction. Thus, we calculated the reliability factor (r_{sat}) and re-estimated the effective mobility (μ_{eff}) to prevent mobility overestimation as shown in **Table 2.3**. The values of μ_{eff}s were slightly lower than those of the maximum μ_es, but exhibited the same trend as those of μ_{max}s.

2.3.2. DPP conjugated polymers

2.3.2.1 Synthesis and Characterization

Phosphonate chain-end functionalized DPP copolymers were prepared by So-Huei Kang from UNIST. The molecular weight (M_v) values of EH4P-Th, EH4P-Se, EH4P-TT, and EH4P-BT were determined as 74.6, 60.5, 44.7, and 58.8 kDa, respectively. However, there can be a deviation in determining the M_v values due to low viscosity of polymer solutions in chloroform in a concentration range of 0.5-1.5

mg mL^{-1} and the different polarities of PDPPTT and the phosphonate chain-end functionalized copolymers.

2.3.2.2 Photophysical, Electrochemical, and Thermal Properties and Theoretical Calculations

The ultraviolet–visible near-infrared absorption spectra of the phosphonate chain-end functionalized DPP copolymers in chlorobenzene solutions and spin-casted films were measured as shown in **Figure 2.13**, and the relevant data are summarized in **Table 2.4**. The absorption spectra of the copolymers in both solution and films exhibit a similar feature, with a localized π–π* transition band in the 300-550-nm region and a strong intermolecular charge-transfer band in the 550-950-nm region. Taking in a closer look, it was found that the absorption maxima (λ_{max}) and absorption onset (λ_{onset}) values are manifested in the sequence of EH4P-BT < EH4P-TT < EH4P-Th < EH4P-Se as a reflection of the combined effects of varied electron-donating ability and conjugation length of the counterpart comonomers and different effective conjugation length of the polymers.[98, 144-146] When copolymers were solidified from solution to film, the absorption spectra shifted differently as a function of the counterpart comonomers: (i) EH4P-TT exhibited almost no spectral shift; (ii) EH4P-Th and EH4P-BT showed a red-shift, which is a common observation with most conjugated polymers; and (iii) a small blue-shift was observed from EH4P-Se. These phenomena indicate different aggregation capabilities of the copolymers depending on the choice of counterpart comonomer. Based on the λ_{onset}s of the copolymer films, the optical bandgaps (E_g^{opt}s) were estimated to be EH4P-Th (1.29 eV), EH4P-Se (1.27 eV), EH4P-TT (1.31 eV), and EH4P-BT (1.33 eV), respectively.

To observe the electrochemical behavior of the copolymers, cyclic voltammetry was performed in n-Bu4NPF6/CH3CN solution using ferrocene as the external standard. As shown in **Figure 2.14**, all the copolymers showed quasi-reversible

oxidative and reductive waves. The highest occupied molecular orbital (HOMO) and lowest unoccupied molecular orbital (LUMO) levels of the copolymers were estimated according to the equations HOMO (eV) = –(E(ox)^{onset} – E(ferrocene)^{onset} + 4.8) and HOMO (eV) = –(E(red)^{onset} – E(ferrocene)^{onset} + 4.8). The HOMO/LUMO levels of EH4P-Th, EH4P-Se, EH4P-TT, and EH4P-BT are −5.18/−3.61 eV, −5.13/−3.58 eV, −5.09/−3.51 eV, and −5.07/−3.44 eV, respectively (see **Table 2.4**). Judging from their high-lying HOMO and LUMO levels, all the copolymers would be favorably operated as p-type semiconductors with stabilized hole transport when an Au electrode with a work function of −5.1 eV is used.

The thermal properties of the copolymers were evaluated by thermogravimetric analysis. The decomposition temperatures (T_ds) of EH4P-Th, EH4P-Se, EH4P-TT, and EH4P-BT were determined to be 272 ℃, 275 ℃, 275 ℃, and 272 ℃, respectively, indicating sufficient thermal stability for the fabrication process and operation of electronic devices. The large weight loss at the T_ds can involve the thermal hydrolysis process of the pendent phosphonate groups.

Density functional theory was also performed to access additional insights into the electronic features of the copolymers, where two repeating units were taken as each model for the calculation (**Figure 2.15** and **Table 2.5**). In addition to the similarly high structural coplanarity and dipole moment (D) (1.08–1.31 D), all model compounds showed well-delocalized HOMO and LUMO densities.

2.3.2.3 Thin-Film Microstructural Analyses

The film surface morphology and microstructure of the copolymer films were investigated using tapping-mode atomic-force microscopy (AFM) and two-dimensional grazing incidence X-ray diffraction (2D-GIXD) analyses. The detailed methods are described in Experimental Section above. The copolymers were spin-coated onto OTS-treated SiO_2/Si substrates, and then thermally annealed at the optimal condition (150 ℃ for 30 min), which was identical to those of OFET

fabrication in the section given below except that no dielectric or gate electrodes were deposited.

As shown in **Figure 2.16**, the as-spun EH4P-Se, EH4P-TT, and EH4P-BT films have smooth and uniform surfaces and small grains with root-mean-square roughness (R_{RMS}) values of 0.627–0.920 nm, whereas EH4P-Th film exhibits significantly coarse domains including some cavities with a high R_{RMS} value of 2.315 nm. After thermal annealing treatment, the R_{RMS} values of EH4P-Se, EH4P-TT, and EH4P-BT films were slightly increased by up to 25%, showing a higher interconnection and tighter granular packing in those films, which can contribute to efficient charge carrier transport by providing more lowly resistant pathways for charge transport in OFETs.[147-149] On the other hand, the EH4P-Th film became somewhat smoother with a decreased R_{RMS} value of 1.723 nm after thermal annealing and showed an enhanced interconnection of grains with decreased pinholes, which can contribute to stronger intermolecular interactions and larger crystalline size in addition to more efficient charge transport in OFETs. However, EH4P-Th film still have large pinholes and a high roughness, which might lead to a lower charge mobility compared to other polymers.

From the 2D-GIXD patterns of the copolymer films (**Figure 2.17**), it can be seen that the as-spun films show long-range ordered (h00) lamellar Bragg peaks along the out-of-plane (OOP) direction (up to the fourth order for EH4P-Th and fifth order for EH4P-Se, EH4P-TT, and EH4P-BT). Besides, the π-stacking (010) peak along both the OOP and in-plane (IP) directions is also observed for all as-spun films. The (100) d-spacings and (010) π–π stacking distances are similarly about 25–26 Å and ~3.6 Å, respectively. Note that EH4P-Th and EH4P-Se show a more intense π-stacking (010) peak along OOP rather than IP, revealing the signature of face-on dominant π-stacking with respect to the substrate, while the adverse tendency appears for EH4P-TT and EH4P-BT, as evidence of an edge-on dominant packing motif. After thermal annealing at 150 °C, the diffraction patterns of all films became more distinctive and

sharper (see **Figure 2.17** and the corresponding line-cut profiles in **Figure 2.18**), indicating their improved microstructural ordering. The detailed crystallographic parameters are summarized in **Table 2.6**. The annealed EH4P-TT and EH4P-BT films exhibit smaller d(100) values relative to the other annealed films, indicating a denser side-chain packing / interdigitation. We also calculated the peak coherence length (L_c), which is defined as the length over which a crystalline structure is preserved.[150] It was found that in addition to the sufficient and large lamellar L_c establishment for all films, both EH4P-TT and EH4P-BT possess larger π–π L_cs [L_c(010)] than those of EH4P-Th and EH4P-Se, indicating strong π–π interactions between the DPP unit and BT or TT segment with edge-on oriented polymer backbone chains. For all cases, these values obviously increase upon thermal annealing, which agrees well with the increased R_{RMS} values, higher interconnection, and tighter granular packing in annealed EH4P-Se, EH4P-TT, and EH4P-BT films and enhanced intermolecular interconnection of grains in annealed EH4P-Th film in AFM results. Herein, we note that the annealed EH4P-TT demonstrates the greatest L_c(010) of 78.14 nm among all copolymer films in this study.

2.3.2.4 Electrical Characterization of Organic Field-Effect Transistors

The electrical performances of the copolymer films were evaluated from OFET devices in a bottom-gate/top-contact configuration. Thin films were prepared on OTS-treated substrates, followed by thermal deposition of Au electrodes through a shadow mask. The experimental details of device fabrication and measurements are described in Experimental Section above. The highest performing devices were thermally annealed at 150 ℃ for 30 min before the top-contact deposition. All fabrication, annealing, and device testing were performed in a N_2-filled glovebox. As shown in **Figure 2.19**, the transfer curves of the OFET devices display well-defined linear and saturation regime behavior. Corresponding typical output curves are given in **Figure 2.20** and **Figure 2.21**. The relevant data including hole mobility

(μ_h), threshold voltage (V_T), and current on/off ratio (I_{on}/I_{off}) are summarized in **Table 2.7**. All devices exhibited unipolar p-type field-effect behavior because of the low energetic barriers for hole transport concerning Au contacts.

The non-annealed devices exhibited μ_h values of 1.67×10^{-2}, 2.26×10^{-2}, 9.63×10^{-2}, and 6.45×10^{-2} $cm^2 V^{-1} s^{-1}$ for EH4P-Th, EH4P-Se, EH4P-TT, and EH4P-BT, respectively. The thermal annealing treatment enhanced the electrical properties of all devices. The annealed EH4P-TT and EH4P-BT showed better OFET performances than the annealed EH4P-Th and EH4P-Se; specifically, EH4P-TT had the highest μ_h value of 1.46×10^{-1} $cm^2 V^{-1} s^{-1}$, due to the improved quality in the film morphology and microstructure [e.g., highly interconnected fibrillar networks, favorable edge-on-oriented π–π stacking, and larger $L_c(010)$] that were evident from the above morphology study.

The polar phosphonate chain-end groups within the copolymers show strong interaction with metal oxides, possibly allowing for uniform self-assembly on the bare SiO_2/Si substrate.[121, 140-143] With this consideration in mind, we fabricated OFETs on top of bare oxygen plasma-treated SiO_2/Si substrates and followed the same optimized conditions as described above. For all cases, even though the annealed OTS-untreated devices exhibited saturation under p-channel operation with similar variation trends in OFET characteristics, about one or two orders of magnitude lower μ_h values were observed compared to the corresponding OTS-treated devices (**Figure 2.22** and **Table 2.8**).

We also investigated the film morphology of the annealed films on OTS-untreated SiO_2/Si substrates. The AFM images of all films illustrated uniform surface features (**Figure 2.23**), implying good interfacial compatibility of the copolymers and OTS-untreated SiO_2/Si surface. Besides, their 2D-GIXD results demonstrated a similar trend in polymer-packing orientation, yet slightly increased (010) π–π stacking distances with smaller L_c values compared to the corresponding films on the OTS-treated surface (**Figures 2.24**–**2.25**, and **Table 2.9**). Although the film morphology

and microstructure on OTS-untreated SiO_2/Si surface are in a good condition due to the polar nature of phosphonate-chain end functionality of the side chains, the film morphology is different from that on OTS-untreated substrate due to the large surface energy difference between OTS-untreated SiO_2 dielectric surface and hydrophobic polymer films, which reduce the interfacial compatibility and lead to uneven aggregation of polymer chains and poor coverage of the film on surface, which are appeared as white and black dots in the AFM images, respectively. After OTS treatment, the long hydrophobic tail of octadecylsilanes can passivate the dielectric SiO_2 surface, and thus the surface energy difference can be drastically reduced, enabling a uniform arrangement of hydrophobic polymer chains on substrate, increasing the grain size and crystallinity of film, and significantly decreasing the molecular aggregation and interfacial trap states.[151] Consequently, despite the proper OFET operation of OTS-untreated devices based on the copolymers, the observed inferior electrical properties can be explained by the looser π-stacking and formation of crystalline domains with reduced size on OTS-untreated surface. Additionally, considering the excellent solubility observed in eco-friendly MeTHF, the OFET devices were made by spin-coating copolymer solution from MeTHF onto OTS-treated substrates, followed by thermal annealing using the same optimized conditions above. The OFET characteristics showed good saturation behavior and clear saturation currents with μ_h values in the range 2.03 - 4.43×10^{-2} $cm^2\ V^{-1}\ s^{-1}$ and I_{on}/I_{off} between 10^2 and 10^4 (**Figure 2.22** and **Table 2.10**).

2.4. Conclusion

2.4.1. DPP small molecules

We have prepared three dicyanovinyl-end-capped D-A DPP-based n-type small molecules (C2C9CN, SiC4CN, and EH4PCN) with the same length of alkyl spacer yet different end-functionalized side chains. By bringing together the photophysical, electrochemical, and thermal properties of the resulting small molecules in conjunction with the film morphology and charge-transport characteristics, we determined the influence of the polarity and bulkiness of the end-functionalized side chains on their intrinsic molecular features. All the small molecules exhibited n-type transporting behavior in OFET devices; the polar phosphonate side chains in EH4PCN exerted a negative influence on charge-transport properties arising from the poor film-forming quality, while the SiC4CN showed the best device performances with μe up to 1.59×10^{-1} cm^2 V^{-1} s^{-1} with $I_{on}/I_{off} > 105$, which stems from a combination of the 2D edge-on oriented high intergrain connectivity/crystallinity and compatibility with OTS surface induced by end-siloxane pendants. Our comparative study significantly facilitates the understanding of the unique roles of alkyl- vs. siloxane- vs. phosphonate-end side groups in structure-property correlation.

2.4.2. DPP conjugated polymers

In summary, we have prepared a novel DPP monomer containing phosphonate chain-end solubilizing groups that upon copolymerization with various counterpart comonomers (Th, Se, TT, and BT) afforded a series of highly soluble phosphonate chain-end functionalized DPP copolymers (EH4P-Th, EH4P-Se, EH4P-TT, and EH4P-BT). The incorporation of different counterpart comonomers of varying electron-donating strength and conjugation length into DPP-copolymers facilitated tuning of photophysical properties, electronic structure (HOMO/LUMO energy

levels), film morphology, and charge transport characteristics in OFETs. The optimized p-channel OFET with a μ_h value as high as 1.46×10^{-1} cm^2 V^{-1} s^{-1} was demonstrated in EH4P-TT due to a combination of edge-on packing, fibrillar intercalating networks, and large crystalline π-stacking. It is particularly significant that the polar and bulky phosphonate chain-end groups in the resulting copolymers enable proper operation behavior in OFETs fabricated using not only OTS-untreated SiO_2/Si substrates but also eco-friendly MeTHF solution process. We advocate that this strategy of using phosphonate chain-end groups can advance better designs for next-generation semiconducting polymers for various applications.

2. 5. References

2.5.1. DPP small molecules

(1) Forrest, S. R. The Path to Ubiquitous and Low-Cost Organic Electronic Appliances on Plastic. Nature **2004**, 428, 911−918.

(2) Baeg, K.-J.; Caironi, M.; Noh, Y.-Y. Toward Printed Integrated Circuits based on Unipolar or Ambipolar Polymer Semiconductors. Adv. Mater. **2013**, 25, 4210−4244.

(3) Gu, X.; Zhou, Y.; Gu, K.; Kurosawa, T.; Guo, Y.; Li, Y.; Lin, H.; Schroeder, B. C.; Yan, H.; Molina-Lopez, F.; Tassone, C. J.; Wang, C.; Mannsfeld, S. C. B.; Yan, H.; Zhao, D.; Toney, M. F.; Bao, Z. Roll-to-Roll Printed Large-Area All-Polymer Solar Cells with 5% Efficiency Based on a Low Crystallinity Conjugated Polymer Blend. Adv. Energy Mater. **2017**, 7, 1602742.

(4) Min, S.-Y.; Kim, T.-S.; Kim, B. J.; Cho, H.; Noh, Y.-Y.; Yang, H.; Cho, J. H.; Lee, T.-W. Large-Scale Organic Nanowire Lithography and Electronics. Nat. Commun. **2013**, 4, 1773.

(5) Schmatz, B.; Yuan, Z.; Lang, A. W.; Hernandez, J. L.; Reichmanis, E.; Reynolds, J. R. Aqueous Processing for Printed Organic Electronics: Conjugated Polymers with Multistage Cleavable Side Chains. ACS Cent. Sci. **2017**, 3, 961−967.

(6) Yuen, J. D.; Wudl, F. Strong acceptors in donor-acceptor polymers for high performance thin film transistors. Energy Environ. Sci. **2013**, 6, 392−406.

(7) Dong, H.; Fu, X.; Liu, J.; Wang, Z.; Hu, W. 25th Anniversary Article: Key Points for High-Mobility Organic Field-Effect Transistors. Adv. Mater. **2013**, 25, 6158−6183.

(8) Marrocchi, A.; Facchetti, A.; Lanari, D.; Petrucci, C.; Vaccaro, L. Current methodologies for a sustainable approach to π-conjugated organic semiconductors. Energy Environ. Sci. **2016**, 9, 763−786.

(9) Yi, Z.; Wang, S.; Liu, Y. Design of High-Mobility Diketopyrrolopyrrole-Based π-Conjugated Copolymers for Organic Thin-Film Transistors. Adv. Mater. **2015**, 27, 3589−3606.

(10) Tsao, H. N.; Cho, D.; Andreasen, J. W.; Rouhanipour, A.; Breiby, D. W.; Pisula, W.; Müllen, K. The Influence of Morphology on High-Performance Polymer Field-Effect Transistors. Adv. Mater. **2009**, 21, 209−212.

(11) Dou, L.; Liu, Y.; Hong, Z.; Li, G.; Yang, Y. Low-Bandgap NearIR Conjugated Polymers/Molecules for Organic Electronics. Chem. Rev. **2015**, 115, 12633−12665.

(12) Shi, L.; Guo, Y.; Hu, W.; Liu, Y. Design and Effective Synthesis Methods for High-Performance Polymer Semiconductors in Organic Field-Effect Transistors. Mater. Chem. Front. **2017**, 1, 2423−2456.

(13) Sui, Y.; Deng, Y.; Du, T.; Shi, Y.; Geng, Y. Design Strategies of n-Type Conjugated Polymers for Organic Thin-Film Transistors. Mater. Chem. Front. **2019**, 3, 1932−1951.

(14) Yamashita, Y.; Hinkel, F.; Marszalek, T.; Zajaczkowski, W.; Pisula, W.; Baumgarten, M.; Matsui, H.; Müllen, K.; Takeya, J. Mobility Exceeding 10 cm^2 /(V·s) in Donor−Acceptor Polymer Transistors with Band-like Charge Transport. Chem. Mater. **2016**, 28, 420−424.

(15) Tatsuo, H.; Jun, T. Organic Field-Effect Transistors Using Single Crystals. Sci. Technol. Adv. Mater. **2009**, 10, 024314.

(16) Ni, Z.; Dong, H.; Wang, H.; Ding, S.; Zou, Y.; Zhao, Q.; Zhen, Y.; Liu, F.; Jiang, L.; Hu, W. Quinoline-Flanked Diketopyrrolopyrrole Copolymers Breaking through Electron Mobility over 6 cm2 V−1 s −1 in Flexible Thin Film Devices. Adv. Mater. **2018**, 30, 1704843.

(17) Ren, Y.; Yang, X.; Zhou, L.; Mao, J. Y.; Han, S. T.; Zhou, Y. Recent Advances in Ambipolar Transistors for Functional Applications. Adv. Funct. Mater. **2019**, 29, 1902105.

(18) Chen, H.; Guo, Y.; Yu, G.; Zhao, Y.; Zhang, J.; Gao, D.; Liu, H.; Liu, Y. Highly π-Extended Copolymers with Diketopyrrolopyrrole Moieties for High-Performance Field-Effect Transistors. Adv. Mater. **2012**, 24, 4618−4622.

(19) Yu, H.; Park, K. H.; Song, I.; Kim, M.-J.; Kim, Y.-H.; Oh, J. H. Effect of the Alkyl Spacer Length on the Electrical Performance of Diketopyrrolopyrrole-Thiophene Vinylene Thiophene Polymer Semiconductors. J. Mater. Chem. C **2015**, 3, 11697−11704.

(20) Han, A.-R.; Dutta, G. K.; Lee, J.; Lee, H. R.; Lee, S. M.; Ahn, H.; Shin, T. J.; Oh, J. H.; Yang, C. ε-Branched Flexible Side Chain Substituted Diketopyrrolopyrrole-Containing Polymers Designed for High Hole and Electron Mobilities. Adv. Funct. Mater. **2015**, 25, 247− 254.

(21) Lee, J.; Han, A.-R.; Yu, H.; Shin, T. J.; Yang, C.; Oh, J. H. Boosting the Ambipolar Performance of Solution-Processable Polymer Semiconductors via Hybrid Side-Chain Engineering. J. Am. Chem. Soc. **2013**, 135, 9540−9547.

(22) Park, W.-T.; Kim, G.; Yang, C.; Liu, C.; Noh, Y.-Y. Effect of Donor Molecular Structure and Gate Dielectric on Charge-Transporting Characteristics for Isoindigo-Based Donor-Acceptor Conjugated Polymers. Adv. Funct. Mater. **2016**, 26, 4695−4703.

(23) Lei, T.; Cao, Y.; Fan, Y.; Liu, C.-J.; Yuan, S.-C.; Pei, J. High-Performance Air-Stable Organic Field-Effect Transistors: Isoindigo-Based Conjugated Polymers. J. Am. Chem. Soc. **2011**, 133, 6099− 6101.

(24) Shin, E.-S.; Ha, Y. H.; Gann, E.; Lee, Y.-J.; Kwon, S.-K.; McNeill, C. R.; Noh, Y.-Y.; Kim, Y.-H. Design of New Isoindigo-Based Copolymer for Ambipolar Organic Field-Effect Transistors. ACS Appl. Mater. Interfaces **2018**, 10, 13774−13782.

(25) Kim, G.; Kang, S.-J.; Dutta, G. K.; Han, Y.-K.; Shin, T. J.; Noh, Y.-Y.; Yang, C. A Thienoisoindigo-Naphthalene Polymer with Ultrahigh Mobility of 14.4 cm^2 /V·s

That Substantially Exceeds Benchmark Values for Amorphous Silicon Semiconductors. J. Am. Chem. Soc. **2014**, 136, 9477−9483.

(26) Ashraf, R. S.; Kronemeijer, A. J.; James, D. I.; Sirringhaus, H.; McCulloch, I. A New Thiophene Substituted Isoindigo Based Copolymer for High Performance Ambipolar Transistors. Chem. Commun. **2012**, 48, 3939−3941.

(27) Lee, J.; Shin, E.-S.; Kim, Y.-J.; Noh, Y.-Y.; Yang, C. Controlling the Ambipolarity of Thieno-Benzo-Isoindigo Polymer-based Transistors: the Balance of Face-on and Edge-on Populations. J. Mater. Chem. C **2020**, 8, 296−302.

(28) Zhan, X.; Facchetti, A.; Barlow, S.; Marks, T. J.; Ratner, M. A.; Wasielewski, M. R.; Marder, S. R. Rylene and Related Diimides for Organic Electronics. Adv. Mater. **2011**, 23, 268−284.

(29) Lei, T.; Wang, J.-Y.; Pei, J. Roles of Flexible Chains in Organic Semiconducting Materials. Chem. Mater. **2014**, 26, 594−603.

(30) Mei, J.; Bao, Z. Side Chain Engineering in Solution-Processable Conjugated Polymers. Chem. Mater. **2014**, 26, 604−615.

(31) Yang, Y.; Liu, Z.; Zhang, G.; Zhang, X.; Zhang, D. The Effects of Side Chains on the Charge Mobilities and Functionalities of Semiconducting Conjugated Polymers beyond Solubilities. Adv. Mater. **2019**, 31, 1903104.

(32) Park, Y. D.; Kim, D. H.; Jang, Y.; Cho, J. H.; Hwang, M.; Lee, H. S.; Lim, J. A.; Cho, K. Effect of Side Chain Length on Molecular Ordering and Field-Effect Mobility in Poly(3-alkylthiophene) Transistors. Org. Electron. **2006**, 7, 514−520.

(33) Ma, Z.; Geng, H.; Wang, D.; Shuai, Z. Influence of alkyl side chain length on the carrier mobility in organic semiconductors: herringbone vs. pi-pi stacking. J. Mater. Chem. C **2016**, 4, 4546−4555.

(34) Cabanetos, C.; El Labban, A.; Bartelt, J. A.; Douglas, J. D.; Mateker, W. R.; Fréchet, J. M. J.; McGehee, M. D.; Beaujuge, P. M. Linear Side Chains in Benzo[1,2-b:4,5-b′]dithiophene-Thieno[3,4-c]pyrrole-4,6-dione Polymers Direct Self-Assembly and Solar Cell Performance. J. Am. Chem. Soc. **2013**, 135, 4656−4659.

(35) Back, J. Y.; An, T. K.; Cheon, Y. R.; Cha, H.; Jang, J.; Kim, Y.; Baek, Y.; Chung, D. S.; Kwon, S.-K.; Park, C. E.; Kim, Y.-H. Alkyl Chain Length Dependence of the Field-Effect Mobility in Novel Anthracene Derivatives. ACS Appl. Mater. Interfaces **2015**, 7, 351− 358.

(36) Akkerman, H. B.; Mannsfeld, S. C. B.; Kaushik, A. P.; Verploegen, E.; Burnier, L.; Zoombelt, A. P.; Saathoff, J. D.; Hong, S.; Atahan-Evrenk, S.; Liu, X.; Aspuru-Guzik, A.; Toney, M. F.; Clancy, P.; Bao, Z. Effects of Odd-Even Side Chain Length of AlkylSubstituted Diphenylbithiophenes on First Monolayer Thin Film Packing Structure. J. Am. Chem. Soc. **2013**, 135, 11006−11014.

(37) Burnett, E. K.; Ai, Q.; Cherniawski, B. P.; Parkin, S. R.; Risko, C.; Briseno, A. L. Even-Odd Alkyl Chain-Length Alternation Regulates Oligothiophene Crystal Structure. Chem. Mater. **2019**, 31, 6900−6907.

(38) Hu, Y.; Miao, K.; Zha, B.; Miao, X.; Xu, L.; Deng, W. Side Chain Position, Length and Odd/Even Effects on the 2D Self Assembly of Mono-Substituted Anthraquinone Derivatives at the Liquid/Solid interface. RSC Adv. **2015**, 5, 93337−93346.

(39) Fei, Z.; Pattanasattayavong, P.; Han, Y.; Schroeder, B. C.; Yan, F.; Kline, R. J.; Anthopoulos, T. D.; Heeney, M. Influence of Side Chain Regiochemistry on the Transistor Performance of High Mobility, All-Donor Polymers. J. Am. Chem. Soc. **2014**, 136, 15154− 15157.

(40) Kang, S.-H.; Lee, H. R.; Dutta, G. K.; Lee, J.; Oh, J. H.; Yang, C. A Role of Side-Chain Regiochemistry of Thienylene-Vinylene-Thienylene (TVT) in the Transistor Performance of Isomeric Polymers. Macromolecules **2017**, 50, 884−890.

(41) Hu, Y.; Miao, K.; Zha, B.; Xu, L.; Miao, X.; Deng, W. STM Investigation of Structural Isomers: Alkyl Chain Position Induced Self-Assembly at the Liquid/Solid Interface. Phys. Chem. Chem. Phys. **2016**, 18, 624−634.

(42) Kim, Y.; Long, D. X.; Lee, J.; Kim, G.; Shin, T. J.; Nam, K.-W.; Noh, Y.-Y.; Yang, C. A Balanced Face-On to Edge-On Texture Ratio in Naphthalene Diimide-

Based Polymers with Hybrid Siloxane Chains Directs Highly Efficient Electron Transport. Macromolecules **2015**, 48, 5179−5187.

(43) Yang, Y.; Liu, Z.; Chen, L.; Yao, J.; Lin, G.; Zhang, X.; Zhang, G.; Zhang, D. Conjugated Semiconducting Polymer with Thymine Groups in the Side Chains: Charge Mobility Enhancement and Application for Selective Field-Effect Transistor Sensors toward CO and H_2S. Chem. Mater. **2019**, 31, 1800−1807.

(44) Kim, G.; Song, S.; Lee, J.; Kim, T.; Lee, T. H.; Walker, B.; Kim, J. Y.; Yang, C. Control of Charge Dynamics via Use of Nonionic Phosphonate Chains and Their Effectiveness for Inverted Structure Solar Cells. Adv. Energy Mater. **2015**, 5, 1500844.

(45) Han, A.-R.; Lee, J.; Lee, H. R.; Lee, J.; Kang, S.-H.; Ahn, H.; Shin, T. J.; Oh, J. H.; Yang, C. Siloxane Side Chains: A Universal Tool for Practical Applications of Organic Field-Effect Transistors. Macromolecules **2016**, 49, 3739−3748.

(46) Prakoso, S. P.; Kumar, S.; Wu, S.-L.; Ciou, G.-T.; Ke, Y.-J.; Venkateswarlu, S.; Tao, Y.-T.; Wang, C.-L. n-Type Thin-Film Transistors Based on Diketopyrrolopyrrole Derivatives: Role of Siloxane Side Chains and Electron-Withdrawing Substituents. ACS Appl. Mater. Interfaces **2020**, 12, 1169−1178.

(47) Kim, K.-H.; Yu, H.; Kang, H.; Kang, D. J.; Cho, C.-H.; Cho, H.- H.; Oh, J. H.; Kim, B. J. Influence of Intermolecular Interactions of Electron Donating Small Molecules on Their Molecular Packing and Performance in Organic Electronic Devices. J. Mater. Chem. A **2013**, 1, 14538−14547.

(48) Fu, B.; Baltazar, J.; Sankar, A. R.; Chu, P.-H.; Zhang, S.; Collard, D. M.; Reichmanis, E. Enhancing Field-Effect Mobility of Conjugated Polymers Through Rational Design of Branched Side Chains. Adv. Funct. Mater. **2014**, 24, 3734−3744.

(49) Kang, I.; Yun, H.-J.; Chung, D. S.; Kwon, S.-K.; Kim, Y.-H. Record High Hole Mobility in Polymer Semiconductors via Side Chain Engineering. J. Am. Chem. Soc. **2013**, 135, 14896−14899.

(50) He, T.; Leowanawat, P.; Burschka, C.; Stepanenko, V.; Stolte, M.; Würthner, F. Impact of 2-Ethylhexyl Stereoisomers on the Electrical Performance of Single-Crystal Field-Effect Transistors. Adv. Mater. **2018**, 30, 1804032.

(51) Meng, B.; Liu, J.; Wang, L. Oligo(Ethylene Glycol) as Side Chains of Conjugated Polymers for Optoelectronic Applications. Polym. Chem. **2020**, 11, 1261−1270.

(52) Kang, B.; Wu, Z.; Kim, M. J.; Woo, H. Y.; Cho, J. H. Aqueous Alcohol-Processable High-Mobility Semiconducting Copolymers with Engineered Oligo(ethylene glycol) Side Chains. Chem. Mater. **2020**, 32, 1111−1119.

(53) Yeh, M.-L.; Wang, S.-Y.; Martínez Hardigree, J. F.; Podzorov, V.; Katz, H. E. Effect of Side Chain Length on Film Structure and Electron Mobility of Core-Unsubstituted Pyromellitic Diimides and Enhanced Mobility of the Dibrominated Core Using the Optimized Side Chain. J. Mater. Chem. C **2015**, 3, 3029−3037.

(54) Kang, B.; Kim, R.; Lee, S. B.; Kwon, S.-K.; Kim, Y.-H.; Cho, K. Side-Chain-Induced Rigid Backbone Organization of Polymer Semiconductors through Semifluoroalkyl Side Chains. J. Am. Chem. Soc. **2016**, 138, 3679−3686.

(55) Yang, J.; Zhao, Z.; Wang, S.; Guo, Y.; Liu, Y. Insight into High Performance Conjugated Polymers for Organic Field-Effect Transistors. Chem **2018**, 4, 2748−2785.

(56) Quinn, J. T. E.; Zhu, J.; Li, X.; Wang, J.; Li, Y. Recent Progress in the Development of n-Type Organic Semiconductors for Organic Field Effect Transistors. J. Mater. Chem. C **2017**, 5, 8654−8681.

(57) Zhou, Q.; Jiang, Y.; Du, T.; Wang, Z.; Liang, Z.; Han, Y.; Deng, Y.; Tian, H.; Geng, Y. Diketopyrrolopyrrole-Based Small Molecules for Solution-Processed n-Channel Organic Thin Film Transistors. J. Mater. Chem. C **2019**, 7, 13939−13946.

(58) Yoon, W. S.; Park, S. K.; Cho, I.; Oh, J.-A.; Kim, J. H.; Park, S. Y. High-Mobility n-Type Organic Transistors Based on a Crystallized Diketopyrrolopyrrole Derivative. Adv. Funct. Mater. **2013**, 23, 3519− 3524.

(59) Wang, C.; Qin, Y.; Sun, Y.; Guan, Y.-S.; Xu, W.; Zhu, D. Thiophene-Diketopyrrolopyrrole-Based Quinoidal Small Molecules as Solution-Processable and Air-Stable Organic Semiconductors: Tuning of the Length and Branching Position of the Alkyl Side Chain toward a High-Performance n-Channel Organic Field-Effect Transistor. ACS Appl. Mater. Interfaces **2015**, 7, 15978−15987.

(60) Lin, G.; Qin, Y.; Zhang, J.; Guan, Y.-S.; Xu, H.; Xu, W.; Zhu, D. Ambipolar organic field-effect transistors based on diketopyrrolopyrrole derivatives containing different π-conjugating spacers. J. Mater. Chem. C **2016**, 4, 4470−4477.

(61) Wu, S.-L.; Huang, Y.-F.; Hsieh, C.-T.; Lai, B.-H.; Tseng, P.-S.; Ou, J.-T.; Liao, S.-T.; Chou, S.-Y.; Wu, K.-Y.; Wang, C.-L. Roles of 3- Ethylrhodanine in Attaining Highly Ordered Crystal Arrays of Ambipolar Diketopyrrolopyrrole Oligomers. ACS Appl. Mater. Interfaces **2017,** 9, 14967−14973.

(62) Duan, C.; Zhong, C.; Liu, C.; Huang, F.; Cao, Y. Highly Efficient Inverted Polymer Solar Cells Based on an Alcohol Soluble Fullerene Derivative Interfacial Modification Material. Chem. Mater. **2012**, 24, 1682−1689.

(63) Chen, D.; Zhou, H.; Liu, M.; Zhao, W.-M.; Su, S.-J.; Cao, Y. Novel Cathode Interlayers Based on Neutral Alcohol-Soluble Small Molecules with a Triphenylamine Core Featuring Polar Phosphonate Side Chains for High-Performance Polymer Light-Emitting and Photovoltaic Devices. Macromol. Rapid Commun. **2013**, 34, 595−603.

(64) Comyn, J. Contact Angles and Adhesive Bonding. Int. J. Adhes. Adhes. **1992**, 12, 145−149.

(65) Wu, S. Polar and Nonpolar Interactions in Adhesion. J. Adhes. **1973**, 5, 39−55.

(66) Chen, S.; Cho, H. J.; Lee, J.; Yang, Y.; Zhang, Z.-G.; Li, Y.; Yang, C. Modulating the Molecular Packing and Nanophase Blending via a Random Terpolymerization Strategy toward 11% Efficiency Nonfullerene Polymer Solar Cells. Adv. Energy Mater. **2017**, 7, 1701125.

(67) Pickett, A.; Torkkeli, M.; Mukhopadhyay, T.; Puttaraju, B.; Laudari, A.; Lauritzen, A. E.; Bikondoa, O.; Kjelstrup-Hansen, J.; Knaapila, M.; Patil, S.; Guha, S. Correlating Charge Transport with Structure in Deconstructed Diketopyrrolopyrrole Oligomers: A Case Study of a Monomer in Field-Effect Transistors. ACS Appl. Mater. Interfaces **2018**, 10, 19844−19852.

2.5.2. DPP conjugated polymers

(1) Zhang, T.; An, C.; Bi, P.; Lv, Q.; Qin, J.; Hong, L.; Cui, Y.; Zhang, S.; Hou, J. A Thiadiazole-Based Conjugated Polymer with Ultradeep HOMO Level and Strong Electroluminescence Enables 18.6% Efficiency in Organic Solar Cell. **2021**, 11, 2101705.

(2) Zhang, Z.-G.; Wang, J. Structures and Properties of Conjugated Donor-Acceptor Copolymers for Solar Cell Applications. J. Mater. Chem. **2012**, 22, 4178-4187.

(3) He, Z.; Xiao, B.; Liu, F.; Wu, H.; Yang, Y.; Xiao, S.; Wang, C.; Russell, T. P.; Cao, Y. Single-Junction Polymer Solar Cells with High Efficiency and Photovoltage. Nat. Photon. **2015**, 9, 174-179.

(4) Chen, J.-D.; Cui, C.; Li, Y.-Q.; Zhou, L.; Ou, Q.-D.; Li, C.; Li, Y.; Tang, J.-X. Single-Junction Polymer Solar Cells Exceeding 10% Power Conversion Efficiency. Adv. Mater. **2015**, 27, 1035-1041.

(5) Nguyen, T. L.; Choi, H.; Ko, S. J.; Uddin, M. A.; Walker, B.; Yum, S.; Jeong, J. E.; Yun, M. H.; Shin, T. J.; Hwang, S.; Kim, J. Y.; Woo, H. Y. Semi-Crystalline Photovoltaic Polymers with Efficiency Exceeding 9% in a ~300 nm thick Conventional Single-Cell Device. Energy Environ. Sci. **2014**, 7, 3040-3051.

(6) Gurney, R. S.; Lidzey, D. G.; Wang, T. A Review of Non-Fullerene Polymer Solar Cells: from Device Physics to Morphology Control. Rep. Prog. Phys. **2019**, 82, 036601.

(7) Zhang, S.; Ye, L.; Zhao, W.; Yang, B.; Wang, Q.; Hou, J. Realizing over 10% Efficiency in Polymer Solar Cell by Device Optimization. Sci. China: Chem. **2015**, 58, 248-256.

(8) Li, G.; Zhu, R.; Yang, Y. Polymer Solar Cells. Nat. Photon. **2012**, 6, 153-161.

(9) Beaujuge, P. M.; Fréchet, J. M. J. Molecular Design and Ordering Effects in π-Functional Materials for Transistor and Solar Cell Applications. J. Am. Chem. Soc. **2011**, 133, 20009-20029.

(10) Dou, L.; Liu, Y.; Hong, Z.; Li, G.; Yang, Y. Low-Bandgap Near-IR Conjugated Polymers/Molecules for Organic Electronics. Chem. Rev. **2015**, 115, 12633-12665.

(11) Zhou, E.; Hashimoto, K.; Tajima, K. Low Band Gap Polymers for Photovoltaic Device with Photocurrent Response Wavelengths over 1000 nm. Polymer **2013**, 54, 6501-6509.

(12) Lo, C. K.; Wolfe, R. M. W.; Reynolds, J. R. From Monomer to Conjugated Polymer: A Perspective on Best Practices for Synthesis. Chem. Mater. **2021**, 33, 4842-4852.

(13) Jo, J. W.; Jung, J. W.; Jung, E. H.; Ahn, H.; Shin, T. J.; Jo, W. H. Fluorination on Both D and A units in D-A type Conjugated Copolymers based on Difluorobithiophene and Benzothiadiazole for Highly Efficient Polymer Solar Cells. Energy Environ. Sci. **2015**, 8, 2427-2434.

(14) Chen, M.-H.; Hou, J.; Hong, Z.; Yang, G.; Sista, S.; Chen, L.-M.; Yang, Y. Efficient Polymer Solar Cells with Thin Active Layers Based on Alternating Polyfluorene Copolymer/Fullerene Bulk Heterojunctions. Adv. Mater. **2009**, 21, 4238-4242.

(15) Vohra, V.; Kawashima, K.; Kakara, T.; Koganezawa, T.; Osaka, I.; Takimiya, K.; Murata, H. Efficient Inverted Polymer Solar Cells Employing Favourable Molecular Orientation. Nat. Photon. **2015**, 9, 403-408.

(16) Kularatne, R. S.; Magurudeniya, H. D.; Sista, P.; Biewer, M. C.; Stefan, M. C. Donor–Acceptor Semiconducting Polymers for Organic Solar Cells. J. Polym. Sci., Part A: Polym. Chem. **2013**, 51, 743-768.

(17) Lee, J. W.; Ahn, H.; Jo, W. H. Conjugated Random Copolymers Consisting of Pyridine- and Thiophene-Capped Diketopyrrolopyrrole as Co-Electron Accepting Units To Enhance both JSC and VOC of Polymer Solar Cells. Macromolecules **2015**, 48, 7836-7842.

(18) R. Murad, A.; Iraqi, A.; Aziz, S. B.; N. Abdullah, S.; Brza, M. A. Conducting Polymers for Optoelectronic Devices and Organic Solar Cells: A Review. **2020**, 12, 2627.

(19) Yang, J.; Xiao, B.; Tang, A.; Li, J.; Wang, X.; Zhou, E. Aromatic-Diimide-Based n-Type Conjugated Polymers for All-Polymer Solar Cell Applications. Adv. Mater. **2019**, 31, 1804699.

(20) Liu, Y.; Zhao, J.; Li, Z.; Mu, C.; Ma, W.; Hu, H.; Jiang, K.; Lin, H.; Ade, H.; Yan, H. Aggregation and Morphology Control Enables Multiple Cases of High-Efficiency Polymer Solar Cells. Nat. Commun. **2014**, 5, 5293.

(21) Zhao, X.; Zhan, X. Electron Transporting Semiconducting Polymers in Organic Electronics. Chem. Soc. Rev. **2011**, 40, 3728-3743.

(22) Zhan, X.; Tan, Z. a.; Domercq, B.; An, Z.; Zhang, X.; Barlow, S.; Li, Y.; Zhu, D.; Kippelen, B.; Marder, S. R. A High-Mobility Electron-Transport Polymer with Broad Absorption and Its Use in Field-Effect Transistors and All-Polymer Solar Cells. J. Am. Chem. Soc. **2007**, 129, 7246-7247.

(23) Yuen, J. D.; Wudl, F. Strong Acceptors in Donor–Acceptor Polymers for High Performance Thin Film Transistors. Energy Environ. Sci. **2013**, 6, 392-406.

(24) Lee, J. Physical Modeling of Charge Transport in Conjugated Polymer Field-Effect Transistors. J. Phys. D: Appl. Phys. **2021**, 54, 143002.

(25) Murphy, A. R.; Fréchet, J. M. J. Organic Semiconducting Oligomers for Use in Thin Film Transistors. Chem. Rev. **2007**, 107, 1066-1096.

(26) Surya, S. G.; Raval, H. N.; Ahmad, R.; Sonar, P.; Salama, K. N.; Rao, V. R. Organic Field Effect Transistors (OFETs) in Environmental Sensing and Health Monitoring: A review. TrAC, Trends Anal. Chem. **2019**, 111, 27-36.

(27) Ashraf, R. S.; Kronemeijer, A. J.; James, D. I.; Sirringhaus, H.; McCulloch, I. A New Thiophene Substituted Isoindigo Based Copolymer for High Performance Ambipolar Transistors. Chem. Commun. **2012**, 48, 3939-3941.

(28) Tsao, H. N.; Cho, D.; Andreasen, J. W.; Rouhanipour, A.; Breiby, D. W.; Pisula, W.; Müllen, K. The Influence of Morphology on High-Performance Polymer Field-Effect Transistors. Adv. Mater. **2009**, 21, 209-212.

(29) Tseng, H.-R.; Phan, H.; Luo, C.; Wang, M.; Perez, L. A.; Patel, S. N.; Ying, L.; Kramer, E. J.; Nguyen, T.-Q.; Bazan, G. C.; Heeger, A. J. High-Mobility Field-Effect Transistors Fabricated with Macroscopic Aligned Semiconducting Polymers. Adv. Mater. **2014**, 26, 2993-2998.

(30) Chen, H.; Guo, Y.; Yu, G.; Zhao, Y.; Zhang, J.; Gao, D.; Liu, H.; Liu, Y. Highly π-Extended Copolymers with Diketopyrrolopyrrole Moieties for High-Performance Field-Effect Transistors. Adv. Mater. **2012**, 24, 4618-4622.

(31) Kim, M.; Ryu, S. U.; Park, S. A.; Choi, K.; Kim, T.; Chung, D.; Park, T. Donor–Acceptor-Conjugated Polymer for High-Performance Organic Field-Effect Transistors: A Progress Report. Adv. Funct. Mater. **2020**, 30, 1904545.

(32) Chen, C.-H.; Wang, Y.; Michinobu, T.; Chang, S.-W.; Chiu, Y.-C.; Ke, C.-Y.; Liou, G.-S. Donor–Acceptor Effect of Carbazole-Based Conjugated Polymer Electrets on Photoresponsive Flash Organic Field-Effect Transistor Memories. ACS Appl. Mater. Interfaces **2020**, 12, 6144-6150.

(33) Sirringhaus, H. Device Physics of Solution-Processed Organic Field-Effect Transistors. Adv. Mater. **2005**, 17, 2411-2425.

(34) Yi, Z.; Wang, S.; Liu, Y. Design of High-Mobility Diketopyrrolopyrrole-Based π-Conjugated Copolymers for Organic Thin-Film Transistors. Adv. Mater. **2015**, 27, 3589-3606.

(35) Marrocchi, A.; Facchetti, A.; Lanari, D.; Petrucci, C.; Vaccaro, L. Current Methodologies for a Sustainable Approach to π-Conjugated Organic Semiconductors. Energy Environ. Sci. **2016**, 9, 763-786.

(36) Dong, H.; Fu, X.; Liu, J.; Wang, Z.; Hu, W. 25th Anniversary Article: Key Points for High-Mobility Organic Field-Effect Transistors. Adv. Mater. **2013**, 25, 6158-6183.

(37) Kelly, T. L.; Wolf, M. O. Template Approaches to Conjugated Polymer Micro- and Nanoparticles. Chem. Soc. Rev. **2010**, 39, 1526-1535.

(38) Sekine, C.; Tsubata, Y.; Yamada, T.; Kitano, M.; Doi, S. Recent Progress of High Performance Polymer OLED and OPV Materials for Organic Printed Electronics. Sci. Technol. Adv. Mater. **2014**, 15, 034203.

(39) AlSalhi, M. S.; Alam, J.; Dass, L. A.; Raja, M. Recent Advances in Conjugated Polymers for Light Emitting Devices. Int. J. Mol. Sci. **2011**, 12, 2036-2054.

(40) Crossley, D. L.; Urbano, L.; Neumann, R.; Bourke, S.; Jones, J.; Dailey, L. A.; Green, M.; Humphries, M. J.; King, S. M.; Turner, M. L.; Ingleson, M. J. Post-polymerization C–H Borylation of Donor–Acceptor Materials Gives Highly Efficient Solid State Near-Infrared Emitters for Near-IR-OLEDs and Effective Biological Imaging. ACS Appl. Mater. Interfaces **2017**, 9, 28243-28249.

(41) Gross, M.; Müller, D. C.; Nothofer, H.-G.; Scherf, U.; Neher, D.; Bräuchle, C.; Meerholz, K. Improving the Performance of Doped π-Conjugated Polymers for Use in Organic Light-Emitting Diodes. Nature **2000**, 405, 661-665.

(42) Zhang, X.; Chen, Z.; Yang, C.; Li, Z.; Zhang, K.; Yao, H.; Qin, J.; Chen, J.; Cao, Y. Highly Efficient Polymer Light-Emitting Diodes Using Color-Tunable Carbazole-based Iridium Complexes. Chem. Phys. Lett. **2006**, 422, 386-390.

(43) MacFarlane, L. R.; Shaikh, H.; Garcia-Hernandez, J. D.; Vespa, M.; Fukui, T.; Manners, I. Functional Nanoparticles through π-Conjugated Polymer Self-Assembly. Nat. Rev. Mater. **2021**, 6, 7-26.

(44) Palani, P.; Karpagam, S. Conjugated Polymers – a Versatile Platform for Various Photophysical, Electrochemical and Biomedical Applications: a Comprehensive Review. New J. Chem. **2021**, 45, 19182-19209.

(45) Jadoun, S.; Riaz, U., Conjugated Polymer Light-Emitting Diodes. In Polymers for Light-Emitting Devices and Displays, **2020**; pp 77-98.

(46) Rai, V.; Singh, R. S.; Blackwood, D. J.; Zhili, D. A Review on Recent Advances in Electrochromic Devices: A Material Approach. Adv. Eng. Mater. **2020**, 22, 2000082.

(47) Xiong, S.; Yin, S.; Wang, Y.; Kong, Z.; Lan, J.; Zhang, R.; Gong, M.; Wu, B.; Chu, J.; Wang, X. Organic/Inorganic Electrochromic Nanocomposites with Various Interfacial Interactions: A Review. Mater. Sci. Eng., B **2017**, 221, 41-53.

(48) Beverina, L.; Pagani, G. A.; Sassi, M. Multichromophoric Electrochromic Polymers: Colour Tuning of Conjugated Polymers through the Side Chain Functionalization Approach. Chem. Commun. **2014**, 50, 5413-5430.

(49) Wang, H.; Barrett, M.; Duane, B.; Gu, J.; Zenhausern, F. Materials and Processing of Polymer-based Electrochromic Devices. Mater. Sci. Eng., B **2018**, 228, 167-174.

(50) Thakur, V. K.; Ding, G.; Ma, J.; Lee, P. S.; Lu, X. Hybrid Materials and Polymer Electrolytes for Electrochromic Device Applications (Adv. Mater. 30/2012). Adv. Mater. **2012**, 24, 4070-4070.

(51) Mortimer, R. J. Electrochromic Materials. Annu. Rev. Mater. Res. **2011**, 41, 241-268.

(52) Kim, J.; Rémond, M.; Kim, D.; Jang, H.; Kim, E. Electrochromic Conjugated Polymers for Multifunctional Smart Windows with Integrative Functionalities. Adv. Mater. Technol. **2020**, 5, 1900890.

(53) Neo, W. T.; Ye, Q.; Chua, S.-J.; Xu, J. Conjugated Polymer-based Electrochromics: Materials, Device Fabrication and Application Prospects. J. Mater. Chem. C **2016**, 4, 7364-7376.

(54) Ren, Y.; Yang, X.; Zhou, L.; Mao, J.-Y.; Han, S.-T.; Zhou, Y. Recent Advances in Ambipolar Transistors for Functional Applications. Adv. Funct. Mater. **2019**, 29, 1902105.

(55) Ni, Z.; Dong, H.; Wang, H.; Ding, S.; Zou, Y.; Zhao, Q.; Zhen, Y.; Liu, F.; Jiang, L.; Hu, W. Quinoline-Flanked Diketopyrrolopyrrole Copolymers Breaking through Electron Mobility over 6 cm2 V−1 s−1 in Flexible Thin Film Devices. Adv. Mater. **2018**, 30, 1704843.

(56) Tatsuo, H.; Jun, T. Organic Field-Effect Transistors Using Single Crystals. Sci. Technol. Adv. Mater. **2009**, 10, 024314.

(57) Yamashita, Y.; Hinkel, F.; Marszalek, T.; Zajaczkowski, W.; Pisula, W.; Baumgarten, M.; Matsui, H.; Müllen, K.; Takeya, J. Mobility Exceeding 10 $cm^2/(V·s)$ in Donor–Acceptor Polymer Transistors with Band-like Charge Transport. Chem. Mater. **2016**, 28, 420-424.

(58) Sui, Y.; Deng, Y.; Du, T.; Shi, Y.; Geng, Y. Design Strategies of n-Type Conjugated Polymers for Organic Thin-Film Transistors. Mater. Chem. Front. **2019**, 3, 1932-1951.

(59) Shi, L.; Guo, Y.; Hu, W.; Liu, Y. Design and Effective Synthesis Methods for High-Performance Polymer Semiconductors in Organic Field-Effect Transistors. Mater. Chem. Front. **2017**, 1, 2423-2456.

(60) Zhang, L.; Pei, K.; Yu, M.; Huang, Y.; Zhao, H.; Zeng, M.; Wang, Y.; Gao, J. Theoretical Investigations on Donor–Acceptor Conjugated Copolymers Based on Naphtho[1,2-c:5,6-c]bis[1,2,5]thiadiazole for Organic Solar Cell Applications. The Journal of Physical Chemistry C **2012**, 116, 26154-26161.

(61) Li, Y. Molecular Design of Photovoltaic Materials for Polymer Solar Cells: Toward Suitable Electronic Energy Levels and Broad Absorption. Acc. Chem. Res. **2012**, 45, 723-733.

(62) Ran, N. A.; Love, J. A.; Takacs, C. J.; Sadhanala, A.; Beavers, J. K.; Collins, S. D.; Huang, Y.; Wang, M.; Friend, R. H.; Bazan, G. C.; Nguyen, T.-Q. Harvesting the Full Potential of Photons with Organic Solar Cells. Adv. Mater. **2016**, 28, 1482-1488.
(63) Janssen, R. A. J.; Nelson, J. Factors Limiting Device Efficiency in Organic Photovoltaics. Adv. Mater. **2013**, 25, 1847-1858.
(64) Kim, B.-G.; Ma, X.; Chen, C.; Ie, Y.; Coir, E. W.; Hashemi, H.; Aso, Y.; Green, P. F.; Kieffer, J.; Kim, J. Energy Level Modulation of HOMO, LUMO, and Band-Gap in Conjugated Polymers for Organic Photovoltaic Applications. **2013**, 23, 439-445.
(65) Coakley, K. M.; McGehee, M. D. Conjugated Polymer Photovoltaic Cells. Chem. Mater. **2004**, 16, 4533-4542.
(66) Gierschner, J.; Cornil, J.; Egelhaaf, H.-J. Optical Bandgaps of π-Conjugated Organic Materials at the Polymer Limit: Experiment and Theory. Adv. Mater. **2007**, 19, 173-191.
(67) Li, X.; Guo, J.; Yang, L.; Chao, M.; Zheng, L.; Ma, Z.; Hu, Y.; Zhao, Y.; Chen, H.; Liu, Y. Low Bandgap Donor-Acceptor π-Conjugated Polymers From Diarylcyclopentadienone-Fused Naphthalimides. **2019**, 7.
(68) Scharber, M. C.; Sariciftci, N. S. Low Band Gap Conjugated Semiconducting Polymers. **2021**, 6, 2000857.
(69) Wu, W.; Liu, Y.; Zhu, D. π-Conjugated Molecules with Fused Rings for Organic Field-Effect Transistors: Design, Synthesis and Applications. Chem. Soc. Rev. **2010**, 39, 1489-1502.
(70) Sarkar, T.; Schneider, S. A.; Ankonina, G.; Hendsbee, A. D.; Li, Y.; Toney, M. F.; Frey, G. L. Tuning Intra and Intermolecular Interactions for Balanced Hole and Electron Transport in Semiconducting Polymers. Chem. Mater. **2020**, 32, 7338-7346.
(71) Jheng, J.-F.; Lai, Y.-Y.; Wu, J.-S.; Chao, Y.-H.; Wang, C.-L.; Hsu, C.-S. Influences of the Non-Covalent Interaction Strength on Reaching High Solid-State

Order and Device Performance of a Low Bandgap Polymer with Axisymmetrical Structural Units. Adv. Mater. **2013**, 25, 2445-2451.

(72) Shi, X.; Bao, W. Hydrogen-Bonded Conjugated Materials and Their Application in Organic Field-Effect Transistors. **2021**, 9, 723718.

(73) Wang, S.; Fabiano, S.; Himmelberger, S.; Puzinas, S.; Crispin, X.; Salleo, A.; Berggren, M. Experimental Evidence that Short-Range Intermolecular Aggregation is Sufficient for Efficient Charge Transport in Conjugated Polymers. Proc. Natl. Acad. Sci. **2015**, 112, 10599-10604.

(74) Liu, Y.; Song, J.; Bo, Z. Designing High Performance Conjugated Materials for Photovoltaic Cells with the Aid of Intramolecular Noncovalent Interactions. Chem. Commun. **2021**, 57, 302-314.

(75) Jackson, N. E.; Savoie, B. M.; Kohlstedt, K. L.; Olvera de la Cruz, M.; Schatz, G. C.; Chen, L. X.; Ratner, M. A. Controlling Conformations of Conjugated Polymers and Small Molecules: The Role of Nonbonding Interactions. J. Am. Chem. Soc. **2013**, 135, 10475-10483.

(76) Yu, Z.-D.; Lu, Y.; Wang, J.-Y.; Pei, J. Conformation Control of Conjugated Polymers. **2020**, 26, 16194-16205.

(77) Holliday, S.; Donaghey, J. E.; McCulloch, I. Advances in Charge Carrier Mobilities of Semiconducting Polymers Used in Organic Transistors. Chem. Mater. **2014**, 26, 647-663.

(78) Ashizawa, M.; Zheng, Y.; Tran, H.; Bao, Z. Intrinsically Stretchable Conjugated Polymer Semiconductors in Field Effect Transistors. Prog. Polym. Sci. **2020**, 100, 101181.

(79) Liu, F.; Wang, C.; Baral, J. K.; Zhang, L.; Watkins, J. J.; Briseno, A. L.; Russell, T. P. Relating Chemical Structure to Device Performance via Morphology Control in Diketopyrrolopyrrole-Based Low Band Gap Polymers. J. Am. Chem. Soc. **2013**, 135, 19248-19259.

(80) Afzal, T.; Iqbal, M. J.; Iqbal, M. Z.; Sajjad, A.; Raza, M. A.; Riaz, S.; Kamran, M. A.; Numan, A.; Naseem, S. Effect of Post-Deposition Annealing Temperature on the Charge Carrier Mobility and Morphology of DPPDTT based Organic Field Effect Transistors. Chem. Phys. Lett. **2020**, 750, 137507.

(81) Generali, G.; Dinelli, F.; Capelli, R.; Toffanin, S.; di Maria, F.; Gazzano, M.; Barbarella, G.; Muccini, M. Correlation among Morphology, Crystallinity, and Charge Mobility in OFETs Made of Quaterthiophene Alkyl Derivatives on a Transparent Substrate Platform. The Journal of Physical Chemistry C **2011**, 115, 23164-23169.

(82) Galindo, S.; Tamayo, A.; Leonardi, F.; Mas-Torrent, M. Control of Polymorphism and Morphology in Solution Sheared Organic Field-Effect Transistors. **2017**, 27, 1700526.

(83) Ding, Z.; Liu, D.; Zhao, K.; Han, Y. Optimizing Morphology to Trade Off Charge Transport and Mechanical Properties of Stretchable Conjugated Polymer Films. Macromolecules **2021**, 54, 3907-3926.

(84) Choudhary, K.; Chen, A. X.; Pitch, G. M.; Runser, R.; Urbina, A.; Dunn, T. J.; Kodur, M.; Kleinschmidt, A. T.; Wang, B. G.; Bunch, J. A.; Fenning, D. P.; Ayzner, A. L.; Lipomi, D. J. Comparison of the Mechanical Properties of a Conjugated Polymer Deposited Using Spin Coating, Interfacial Spreading, Solution Shearing, and Spray Coating. ACS Appl. Mater. Interfaces **2021**, 13, 51436-51446.

(85) Baeg, K.-J.; Caironi, M.; Noh, Y.-Y. Toward Printed Integrated Circuits based on Unipolar or Ambipolar Polymer Semiconductors. Adv. Mater. **2013**, 25, 4210-4244.

(86) Gu, X.; Zhou, Y.; Gu, K.; Kurosawa, T.; Guo, Y.; Li, Y.; Lin, H.; Schroeder, B. C.; Yan, H.; Molina-Lopez, F.; Tassone, C. J.; Wang, C.; Mannsfeld, S. C. B.; Yan, H.; Zhao, D.; Toney, M. F.; Bao, Z. Roll-to-Roll Printed Large-Area All-Polymer Solar Cells with 5% Efficiency Based on a Low Crystallinity Conjugated Polymer Blend. Adv. Energy. Mater. **2017**, 7, 1602742.

(87) Tang, W.; Huang, Y.; Han, L.; Liu, R.; Su, Y.; Guo, X.; Yan, F. Recent Progress in Printable Organic Field Effect Transistors. J. Mater. Chem. C **2019**, 7, 790-808.

(88) Kang, B.; Lee, W. H.; Cho, K. Recent Advances in Organic Transistor Printing Processes. ACS Appl. Mater. Interfaces **2013**, 5, 2302-2315.

(89) Bao, Z.; A. Rogers, J.; E. Katz, H. Printable Organic and Polymeric Semiconducting Materials and Devices. J. Mater. Chem. **1999**, 9, 1895-1904.

(90) Baude, P. F.; Ender, D. A.; Haase, M. A.; Kelley, T. W.; Muyres, D. V.; Theiss, S. D. Pentacene-based Radio-Frequency Identification Circuitry. Appl. Phys. Lett. **2003**, 82, 3964-3966.

(91) Forrest, S. R. The Path to Ubiquitous and Low-Cost Organic Electronic Appliances on Plastic. Nature **2004**, 428, 911-918.

(92) Brabec, C. J.; Cravino, A.; Meissner, D.; Sariciftci, N. S.; Fromherz, T.; Rispens, M. T.; Sanchez, L.; Hummelen, J. C. Origin of the Open Circuit Voltage of Plastic Solar Cells. Adv. Funct. Mater. **2001**, 11, 374-380.

(93) Brown, A. R.; Pomp, A.; Hart, C. M.; de Leeuw, D. M. Logic Gates Made from Polymer Transistors and Their Use in Ring Oscillators. Science **1995**, 270, 972-974.

(94) Crone, B.; Dodabalapur, A.; Gelperin, A.; Torsi, L.; Katz, H. E.; Lovinger, A. J.; Bao, Z. Electronic Sensing of Vapors with Organic Transistors. Appl. Phys. Lett. **2001**, 78, 2229-2231.

(95) Someya, T.; Kim, P.; Nuckolls, C. Conductance Measurement of Single-Walled Carbon Nanotubes in Aqueous Environment. Appl. Phys. Lett. **2003**, 82, 2338-2340.

(96) Ji, Y.; Xiao, C.; Wang, Q.; Zhang, J.; Li, C.; Wu, Y.; Wei, Z.; Zhan, X.; Hu, W.; Wang, Z.; Janssen, R. A. J.; Li, W. Asymmetric Diketopyrrolopyrrole Conjugated Polymers for Field-Effect Transistors and Polymer Solar Cells Processed from a Nonchlorinated Solvent. Adv. Mater. **2016**, 28, 943-950.

(97) Kang, S.-H.; Jeong, A.; Lee, H. R.; Oh, J. H.; Yang, C. Bioderived and Eco-Friendly Solvent-Processed High-Mobility Ambipolar Plastic Transistors through Controlled Irregularity of the Polymer Backbone. Chem. Mater. **2019**, 31, 3831-3839.

(98) Yi, Z.; Ma, L.; Chen, B.; Chen, D.; Chen, X.; Qin, J.; Zhan, X.; Liu, Y.; Ong, W. J.; Li, J. Effect of the Longer β-Unsubstituted Oliogothiophene Unit (6T and 7T) on the Organic Thin-Film Transistor Performances of Diketopyrrolopyrrole-Oliogothiophene Copolymers. Chem. Mater. **2013**, 25, 4290-4296.

(99) Mei, J.; Bao, Z. Side Chain Engineering in Solution-Processable Conjugated Polymers. Chem. Mater. **2014**, 26, 604-615.

(100) Lei, T.; Wang, J.-Y.; Pei, J. Roles of Flexible Chains in Organic Semiconducting Materials. Chem. Mater. **2014**, 26, 594-603.

(101) Yang, Y.; Liu, Z.; Zhang, G.; Zhang, X.; Zhang, D. The Effects of Side Chains on the Charge Mobilities and Functionalities of Semiconducting Conjugated Polymers beyond Solubilities. Adv. Mater. **2019**, 31, 1903104.

(102) Kleinschmidt, A. T.; Lipomi, D. J. Stretchable Conjugated Polymers: A Case Study in Topic Selection for New Research Groups. Acc. Chem. Res. **2018**, 51, 3134-3143.

(103) Higashihara, T. Strategic design and synthesis of π-conjugated polymers suitable as intrinsically stretchable semiconducting materials. Polym. J. **2021**, 53, 1061-1071.

(104) Ding, Y.; Yuan, Y.; Wu, N.; Wang, X.; Zhang, G.; Qiu, L. Intrinsically Stretchable n-Type Polymer Semiconductors through Side Chain Engineering. Macromolecules **2021**, 54, 8849-8859.

(105) Grand, C.; Zajaczkowski, W.; Deb, N.; Lo, C. K.; Hernandez, J. L.; Bucknall, D. G.; Müllen, K.; Pisula, W.; Reynolds, J. R. Morphology Control in Films of Isoindigo Polymers by Side-Chain and Molecular Weight Effects. ACS Appl. Mater. Interfaces **2017**, 9, 13357-13368.

(106) Cabanetos, C.; El Labban, A.; Bartelt, J. A.; Douglas, J. D.; Mateker, W. R.; Fréchet, J. M. J.; McGehee, M. D.; Beaujuge, P. M. Linear Side Chains in Benzo[1,2-b:4,5-b′]dithiophene−Thieno[3,4-c]pyrrole-4,6-dione Polymers Direct Self-Assembly and Solar Cell Performance. J. Am. Chem. Soc. **2013**, 135, 4656-4659.

(107) Ma, Z.; Geng, H.; Wang, D.; Shuai, Z. Influence of Alkyl Side-Chain Length on the Carrier Mobility in Organic Semiconductors: Herringbone vs. pi–pi Stacking. J. Mater. Chem. C **2016**, 4, 4546-4555.

(108) Sugiyama, F.; Kleinschmidt, A. T.; Kayser, L. V.; Rodriquez, D.; Finn, M.; Alkhadra, M. A.; Wan, J. M. H.; Ramírez, J.; Chiang, A. S. C.; Root, S. E.; Savagatrup, S.; Lipomi, D. J. Effects of Flexibility and Branching of Side Chains on the Mechanical Properties of Low-Bandgap Conjugated Polymers. Polym. Chem. **2018**, 9, 4354-4363.

(109) Park, Y. D.; Kim, D. H.; Jang, Y.; Cho, J. H.; Hwang, M.; Lee, H. S.; Lim, J. A.; Cho, K. Effect of Side Chain Length on Molecular Ordering and Field-Effect Mobility in Poly(3-alkylthiophene) Transistors. Org. Electron. **2006**, 7, 514-520.

(110) Back, J. Y.; An, T. K.; Cheon, Y. R.; Cha, H.; Jang, J.; Kim, Y.; Baek, Y.; Chung, D. S.; Kwon, S.-K.; Park, C. E.; Kim, Y.-H. Alkyl Chain Length Dependence of the Field-Effect Mobility in Novel Anthracene Derivatives. ACS Appl. Mater. Interfaces **2015**, 7, 351-358.

(111) Hu, Y.; Miao, K.; Zha, B.; Miao, X.; Xu, L.; Deng, W. Side Chain Position, Length and Odd/Even Effects on the 2D Self-Assembly of Mono-Substituted Anthraquinone Derivatives at the Liquid/Solid interface. RSC Adv. **2015**, 5, 93337-93346.

(112) Burnett, E. K.; Ai, Q.; Cherniawski, B. P.; Parkin, S. R.; Risko, C.; Briseno, A. L. Even–Odd Alkyl Chain-Length Alternation Regulates Oligothiophene Crystal Structure. Chem. Mater. **2019**, 31, 6900-6907.

(113) Akkerman, H. B.; Mannsfeld, S. C. B.; Kaushik, A. P.; Verploegen, E.; Burnier, L.; Zoombelt, A. P.; Saathoff, J. D.; Hong, S.; Atahan-Evrenk, S.; Liu, X.; Aspuru-Guzik, A.; Toney, M. F.; Clancy, P.; Bao, Z. Effects of Odd–Even Side Chain Length of Alkyl-Substituted Diphenylbithiophenes on First Monolayer Thin Film Packing Structure. J. Am. Chem. Soc. **2013**, 135, 11006-11014.

(114) Hu, Y.; Miao, K.; Zha, B.; Xu, L.; Miao, X.; Deng, W. STM Investigation of Structural Isomers: Alkyl Chain Position Induced Self-Assembly at the Liquid/Solid Interface. Phys. Chem. Chem. Phys. **2016**, 18, 624-634.

(115) Kang, S.-H.; Lee, H. R.; Dutta, G. K.; Lee, J.; Oh, J. H.; Yang, C. A Role of Side-Chain Regiochemistry of Thienylene–Vinylene–Thienylene (TVT) in the Transistor Performance of Isomeric Polymers. Macromolecules **2017**, 50, 884-890.

(116) Fei, Z.; Pattanasattayavong, P.; Han, Y.; Schroeder, B. C.; Yan, F.; Kline, R. J.; Anthopoulos, T. D.; Heeney, M. Influence of Side-Chain Regiochemistry on the Transistor Performance of High-Mobility, All-Donor Polymers. J. Am. Chem. Soc. **2014**, 136, 15154-15157.

(117) Cho, S.; Seo, J. H.; Kim, S. H.; Song, S.; Jin, Y.; Lee, K.; Suh, H.; Heeger, A. J. Effect of Substituted Side Chain on Donor-Acceptor Conjugated Copolymers. Appl. Phys. Lett. **2008**, 93, 263301.

(118) Han, A. R.; Lee, J.; Lee, H. R.; Lee, J.; Kang, S.-H.; Ahn, H.; Shin, T. J.; Oh, J. H.; Yang, C. Siloxane Side Chains: A Universal Tool for Practical Applications of Organic Field-Effect Transistors. Macromolecules **2016**, 49, 3739-3748.

(119) Prakoso, S. P.; Kumar, S.; Wu, S.-L.; Ciou, G.-T.; Ke, Y.-J.; Venkateswarlu, S.; Tao, Y.-T.; Wang, C.-L. n-Type Thin-Film Transistors Based on Diketopyrrolopyrrole Derivatives: Role of Siloxane Side Chains and Electron-Withdrawing Substituents. ACS Appl. Mater. Interfaces **2020**, 12, 1169-1178.

(120) Lim, B.; Sun, H.; Noh, Y.-Y. Highly Soluble Small-Molecule Organic Semiconductor with Trihexylsilyloxy Side Chain for High-Performance Organic Field-Effect Transistors with Mobility of up to 3.10 cm2 V−1 s−1. Dyes Pigm. **2017**, 142, 17-23.

(121) Kim, G.; Song, S.; Lee, J.; Kim, T.; Lee, T. H.; Walker, B.; Kim, J. Y.; Yang, C. Control of Charge Dynamics via Use of Nonionic Phosphonate Chains and Their Effectiveness for Inverted Structure Solar Cells. Adv. Energy. Mater. **2015**, 5, 1500844.

(122) Yang, Y.; Liu, Z.; Chen, L.; Yao, J.; Lin, G.; Zhang, X.; Zhang, G.; Zhang, D. Conjugated Semiconducting Polymer with Thymine Groups in the Side Chains: Charge Mobility Enhancement and Application for Selective Field-Effect Transistor Sensors toward CO and H2S. Chem. Mater. **2019**, 31, 1800-1807.

(123) Lee, J.; Han, A. R.; Yu, H.; Shin, T. J.; Yang, C.; Oh, J. H. Boosting the Ambipolar Performance of Solution-Processable Polymer Semiconductors via Hybrid Side-Chain Engineering. J. Am. Chem. Soc. **2013**, 135, 9540-9547.

(124) Kim, Y.; Long, D. X.; Lee, J.; Kim, G.; Shin, T. J.; Nam, K.-W.; Noh, Y.-Y.; Yang, C. A Balanced Face-On to Edge-On Texture Ratio in Naphthalene Diimide-Based Polymers with Hybrid Siloxane Chains Directs Highly Efficient Electron Transport. Macromolecules **2015**, 48, 5179-5187.

(125) Han, A.-R.; Dutta, G. K.; Lee, J.; Lee, H. R.; Lee, S. M.; Ahn, H.; Shin, T. J.; Oh, J. H.; Yang, C. ε-Branched Flexible Side Chain Substituted Diketopyrrolopyrrole-Containing Polymers Designed for High Hole and Electron Mobilities. Adv. Funct. Mater. **2015**, 25, 247-254.

(126) Kang, I.; Yun, H.-J.; Chung, D. S.; Kwon, S.-K.; Kim, Y.-H. Record High Hole Mobility in Polymer Semiconductors via Side-Chain Engineering. J. Am. Chem. Soc. **2013**, 135, 14896-14899.

(127) Fu, B.; Baltazar, J.; Sankar, A. R.; Chu, P.-H.; Zhang, S.; Collard, D. M.; Reichmanis, E. Enhancing Field-Effect Mobility of Conjugated Polymers Through Rational Design of Branched Side Chains. Adv. Funct. Mater. **2014**, 24, 3734-3744.

(128) Yu, H.; Kim, H. N.; Song, I.; Ha, Y. H.; Ahn, H.; Oh, J. H.; Kim, Y.-H. Effect of Alkyl Chain Spacer on Charge Transport in n-Type Dominant Polymer Semiconductors with a Diketopyrrolopyrrole-Thiophene-Bithiazole Acceptor–Donor–Acceptor Unit. J. Mater. Chem. C **2017**, 5, 3616-3622.

(129) Huang, S.; Yu, H.; Li, Q. Supramolecular Chirality Transfer toward Chiral Aggregation: Asymmetric Hierarchical Self-Assembly. Adv. Sci. **2021**, 8, 2002132.

(130) He, T.; Leowanawat, P.; Burschka, C.; Stepanenko, V.; Stolte, M.; Würthner, F. Impact of 2-Ethylhexyl Stereoisomers on the Electrical Performance of Single-Crystal Field-Effect Transistors. Adv. Mater. **2018**, 30, 1804032.

(131) Li, C.; Zhai, H.; Liu, X.; Zhang, W.; Huang, Y. Effect of Stereoisomerism of the Alkyl Chain on the Gas Sensing Properties based on Perylene Dyes. J. Mater. Chem. C **2015**, 3, 2778-2782.

(132) Chen, C.-A.; Wang, S.-C.; Tung, S.-H.; Su, W.-F. Oligo(Ethylene Glycol) Side Chain Effect on the Physical Properties and Molecular Arrangement of Oligothiophene–Isoindigo based Conjugated Polymers. Soft Matter **2019**, 15, 9468-9473.

(133) Meng, B.; Liu, J.; Wang, L. Oligo(Ethylene Glycol) as Side Chains of Conjugated Polymers for Optoelectronic Applications. Polym. Chem. **2020**, 11, 1261-1270.

(134) Lee, E.; Hammer, B.; Kim, J.-K.; Page, Z.; Emrick, T.; Hayward, R. C. Hierarchical Helical Assembly of Conjugated Poly(3-hexylthiophene)-block-poly(3-triethylene glycol thiophene) Diblock Copolymers. J. Am. Chem. Soc. **2011**, 133, 10390-10393.

(135) Yang, S.-F.; Zhang, X.; Chen, P.-L.; Liu, Z.-T.; Tian, J.-W.; Zhang, G.-X.; Zhang, D.-Q. Diketopyrrolopyrrole-Based Semiconducting Polymer with Both Hydrophobic Alkyl and Hydrophilic Tetraethylene Glycol Chains for Monolayer Transistor and Sensing Application. Adv. Electron. Mater. **2017**, 3, 1700120.

(136) Kang, B.; Wu, Z.; Kim, M. J.; Woo, H. Y.; Cho, J. H. Aqueous-Alcohol-Processable High-Mobility Semiconducting Copolymers with Engineered Oligo(ethylene glycol) Side Chains. Chem. Mater. **2020**, 32, 1111-1119.

(137) Kang, B.; Kim, R.; Lee, S. B.; Kwon, S.-K.; Kim, Y.-H.; Cho, K. Side-Chain-Induced Rigid Backbone Organization of Polymer Semiconductors through Semifluoroalkyl Side Chains. J. Am. Chem. Soc. **2016**, 138, 3679-3686.

(138) Yeh, M.-L.; Wang, S.-Y.; Martínez Hardigree, J. F.; Podzorov, V.; Katz, H. E. Effect of Side Chain Length on Film Structure and Electron Mobility of Core-Unsubstituted Pyromellitic Diimides and Enhanced Mobility of the Dibrominated Core Using the Optimized Side Chain. J. Mater. Chem. C **2015**, 3, 3029-3037.

(139) Kang, S.-H.; Lee, D.; Kim, H.; Choi, W.; Oh, J.; Oh, J. H.; Yang, C. Effects of the Polarity and Bulkiness of End-Functionalized Side Chains on the Charge Transport of Dicyanovinyl-End-Capped Diketopyrrolopyrrole-Based n-Type Small Molecules. ACS Appl. Mater. Interfaces **2021**, 13, 52840-52849.

(140) Queffélec, C.; Petit, M.; Janvier, P.; Knight, D. A.; Bujoli, B. Surface Modification Using Phosphonic Acids and Esters. Chem. Rev. **2012**, 112, 3777-3807.

(141) Zhou, G.; Qian, G.; Ma, L.; Cheng, Y.; Xie, Z.; Wang, L.; Jing, X.; Wang, F. Polyfluorenes with Phosphonate Groups in the Side Chains as Chemosensors and Electroluminescent Materials. Macromolecules **2005**, 38, 5416-5424.

(142) Chen, D.; Zhou, H.; Liu, M.; Zhao, W.-M.; Su, S.-J.; Cao, Y. Novel Cathode Interlayers Based on Neutral Alcohol-Soluble Small Molecules with a Triphenylamine Core Featuring Polar Phosphonate Side Chains for High-Performance Polymer Light-Emitting and Photovoltaic Devices. Macromol. Rapid Commun. **2013**, 34, 595-603.

(143) Duan, C.; Zhong, C.; Liu, C.; Huang, F.; Cao, Y. Highly Efficient Inverted Polymer Solar Cells Based on an Alcohol Soluble Fullerene Derivative Interfacial Modification Material. Chem. Mater. **2012**, 24, 1682-1689.

(144) Rissler, J. Effective Conjugation Length of π-Conjugated Systems. Chem. Phys. Lett. **2004**, 395, 92-96.

(145) Jiang, X.; Xu, Y.; Wang, X.; Wu, Y.; Feng, G.; Li, C.; Ma, W.; Li, W. Non-Fullerene Organic Solar Cells based on Diketopyrrolopyrrole Polymers as Electron Donors and ITIC as an Electron Acceptor. Phys. Chem. Chem. Phys. **2017**, 19, 8069-8075.

(146) Heintges, G. H. L.; Janssen, R. A. J. On the Homocoupling of Trialkylstannyl Monomers in the Synthesis of Diketopyrrolopyrrole Polymers and Its Effect on the Performance of Polymer-Fullerene Photovoltaic Cells. RSC Adv. **2019**, 9, 15703-15714.

(147) Lei, T.; Cao, Y.; Zhou, X.; Peng, Y.; Bian, J.; Pei, J. Systematic Investigation of Isoindigo-Based Polymeric Field-Effect Transistors: Design Strategy and Impact of Polymer Symmetry and Backbone Curvature. Chem. Mater. **2012**, 24, 1762-1770.

(148) Kim, B. J.; Lee, H.-S.; Lee, J. S.; Cho, S.; Kim, H.; Son, H. J.; Kim, H.; Ko, M. J.; Park, S.; Kang, M. S.; Oh, S. Y.; Kim, B.; Cho, J. H. Correlation between Crystallinity, Charge Transport, and Electrical Stability in an Ambipolar Polymer Field-Effect Transistor Based on Poly(naphthalene-alt-diketopyrrolopyrrole). The Journal of Physical Chemistry C **2013**, 117, 11479-11486.

(149) Yang, S. Y.; Shin, K.; Park, C. E. The Effect of Gate-Dielectric Surface Energy on Pentacene Morphology and Organic Field-Effect Transistor Characteristics. **2005**, 15, 1806-1814.

(150) Patterson, A. L. The Scherrer Formula for X-Ray Particle Size Determination. Phys. Rev. **1939**, 56, 978-982.

(151) Virkar, A.; Mannsfeld, S.; Oh, J. H.; Toney, M. F.; Tan, Y. H.; Liu, G.-y.; Scott, J. C.; Miller, R.; Bao, Z. The Role of OTS Density on Pentacene and C60 Nucleation, Thin Film Growth, and Transistor Performance. **2009**, 19, 1962-1970.

2.6. Figures and Tables

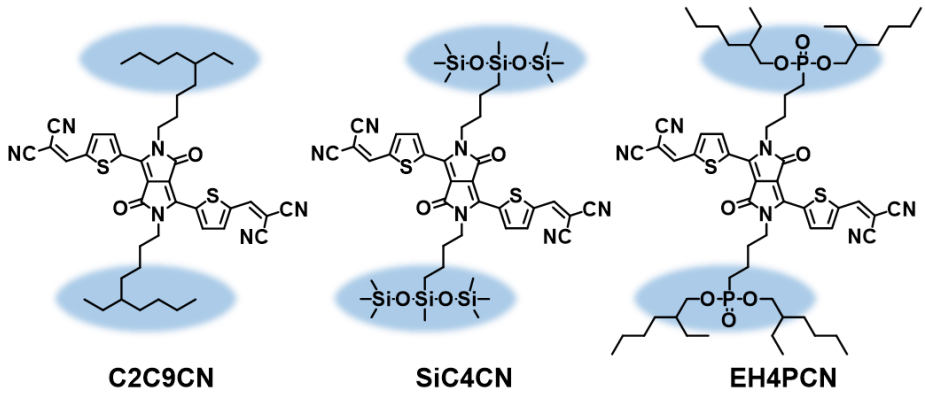

Figure 2.1. Structure of DPP small molecules used in this study.

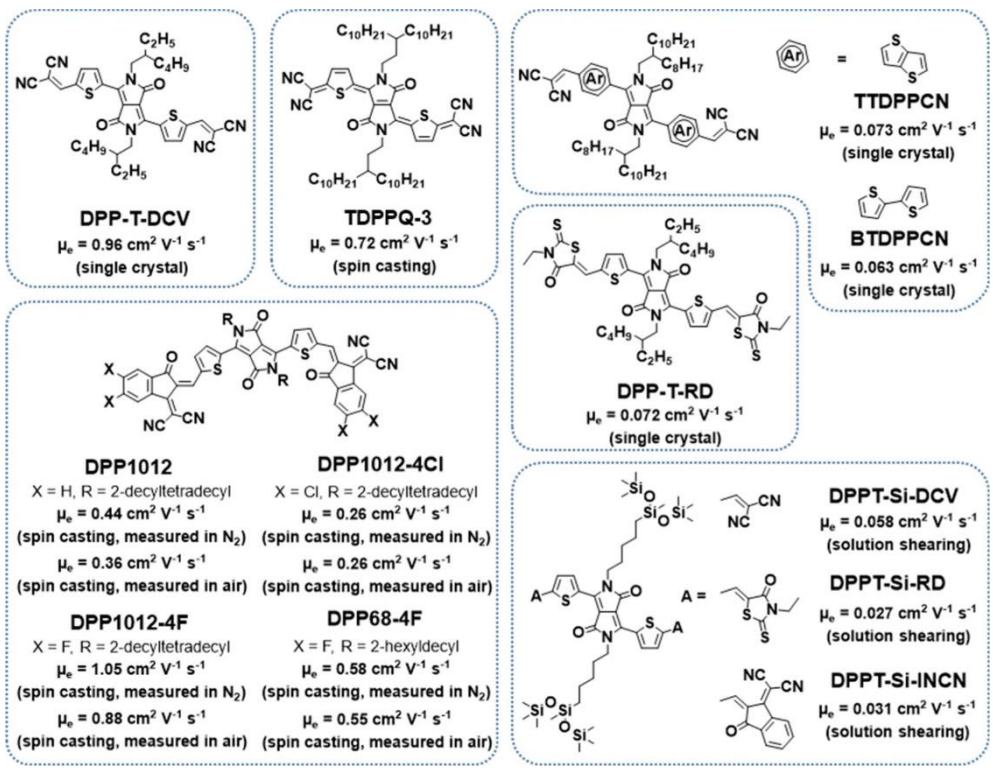

Figure 2.2. Representative n-type DPP-based small molecules used for OFET applications.

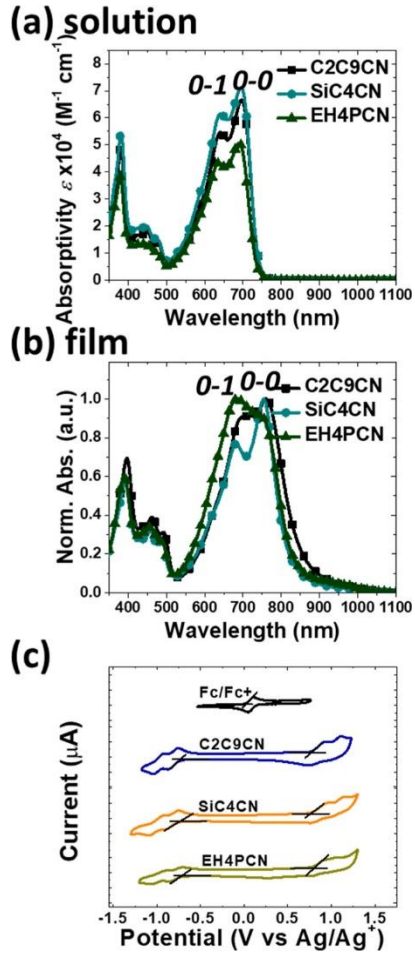

Figure 2.3. (a,b) UV–vis–NIR absorption spectra and (c) cyclic voltammograms.

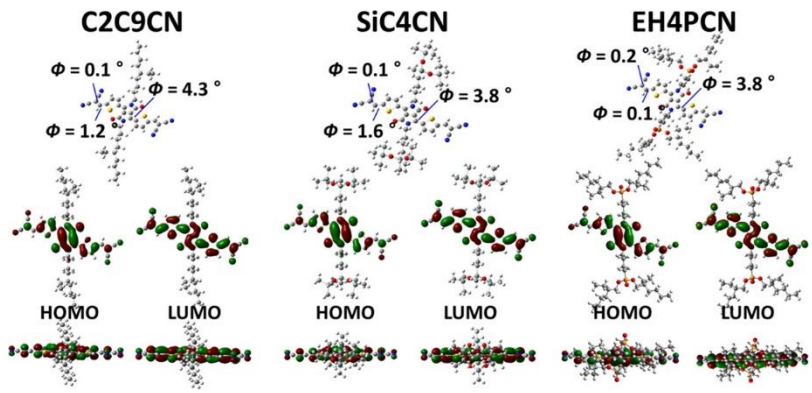

Figure 2.4. DFT-optimized geometries and charge-density isosurfaces.

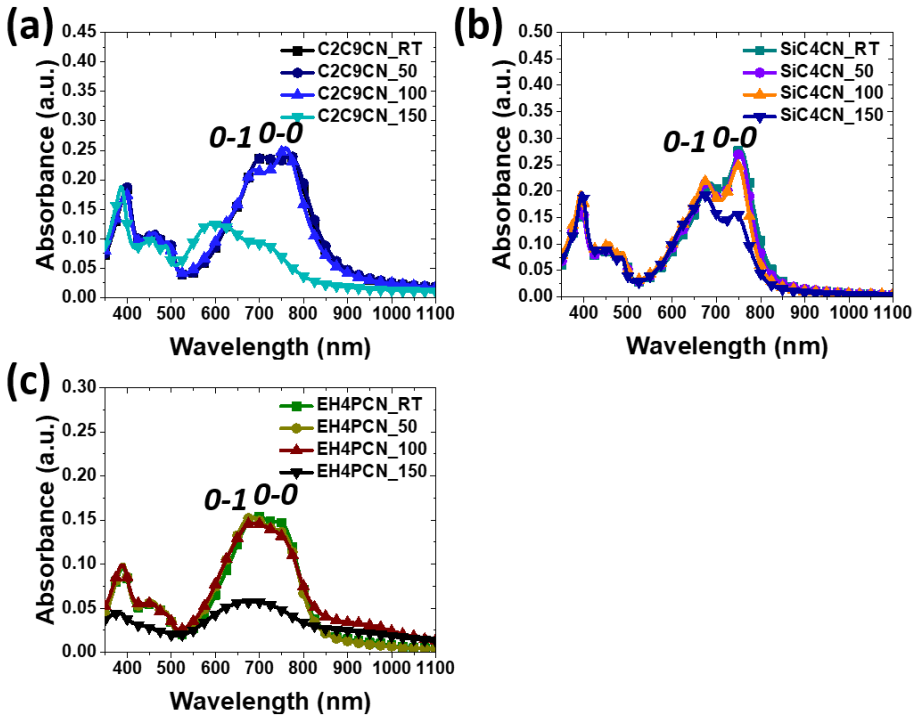

Figure 2.5. UV-Vis-NIR absorption spectra of the thermally annealed films of (a) C2C9CN, (b) SiC4CN, and (c) EH4PCN.

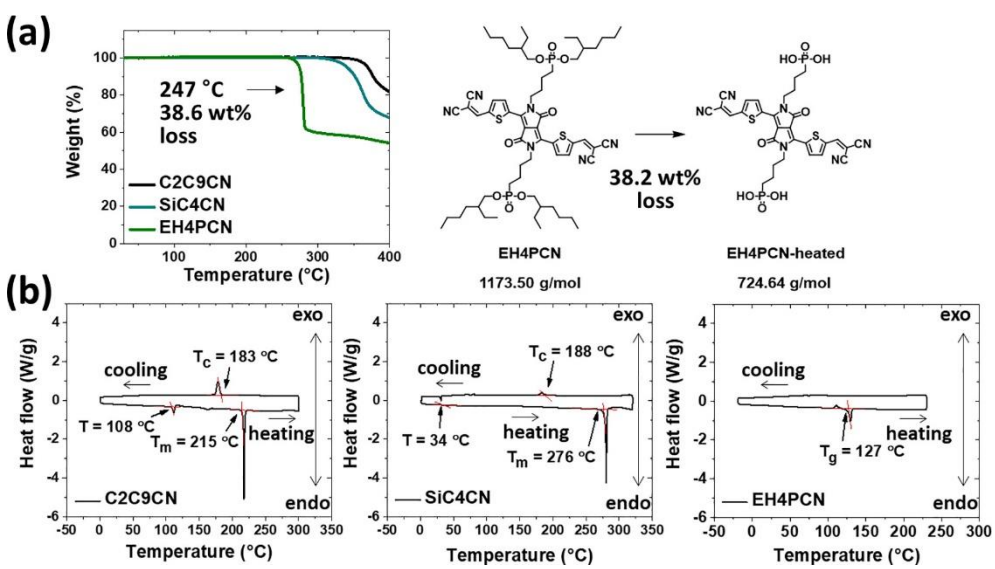

Figure 2.6. (a) TGA and (b) DSC curves.

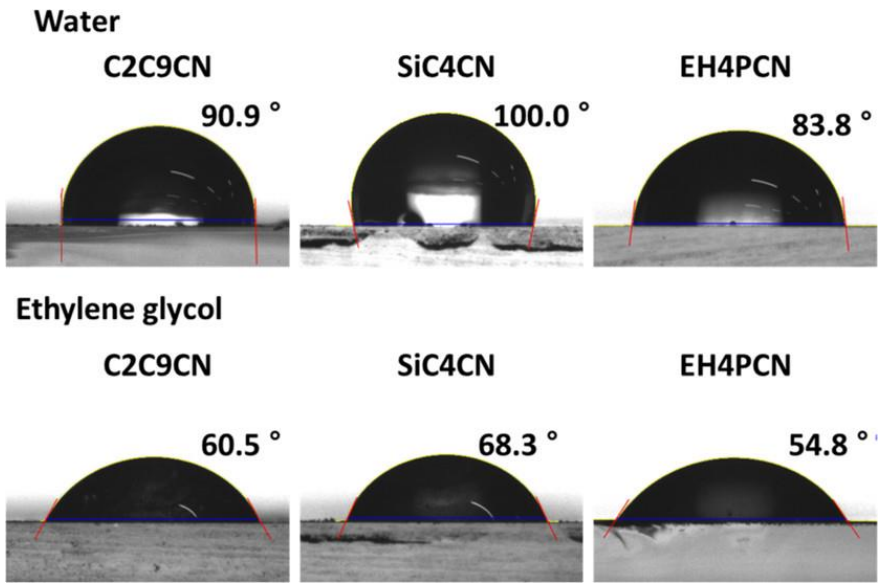

Figure 2.7. Contact angle measurements of the pristine films.

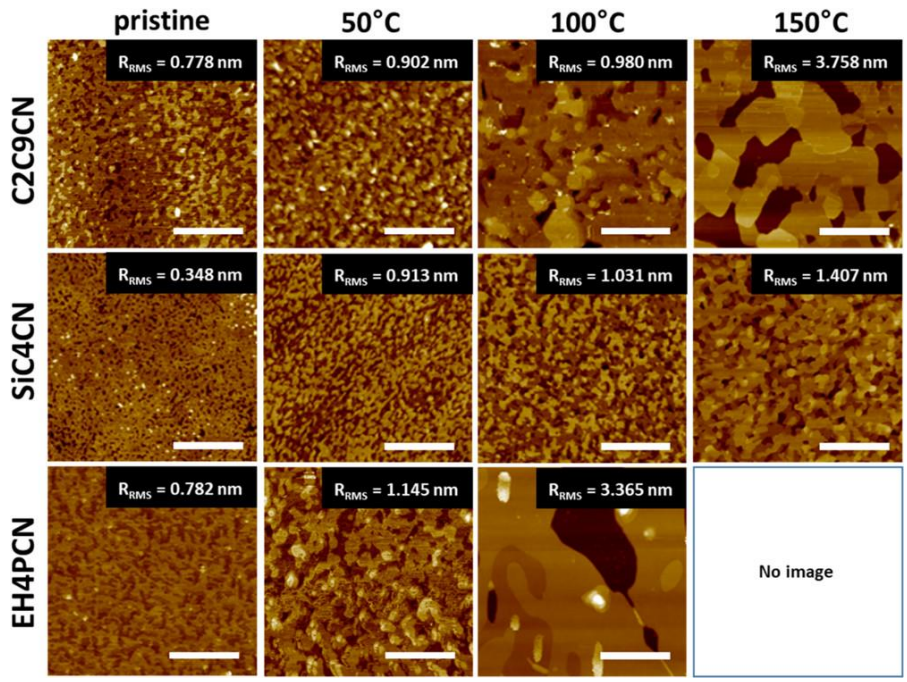

Figure 2.8. AFM height images. R_{rms} is rms roughness of film. Scale bar = 1 μm.

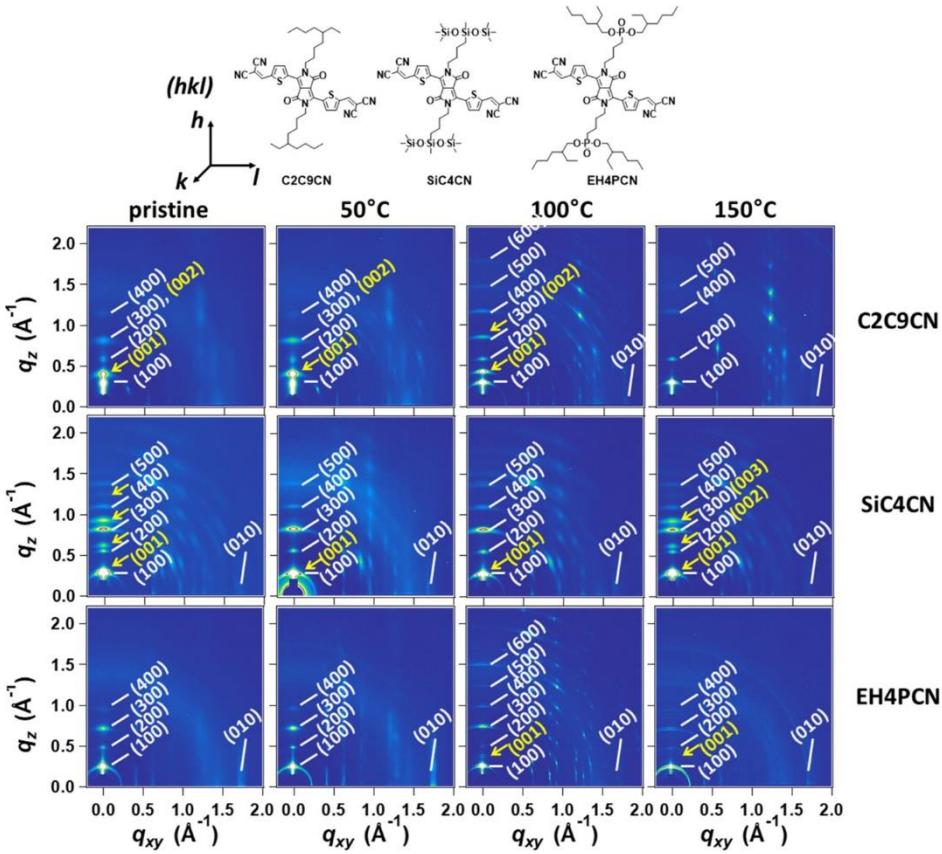

Figure 2.9. 2D-GIXD images of the films.

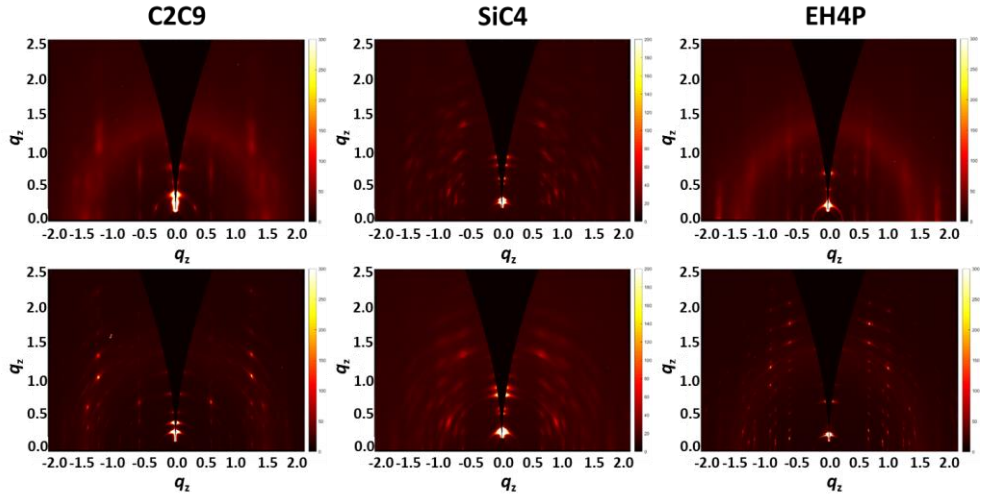

Figure 2.10. GIXD images of the DPP small molecule films converted into the planar figure of the 3D figure cut.

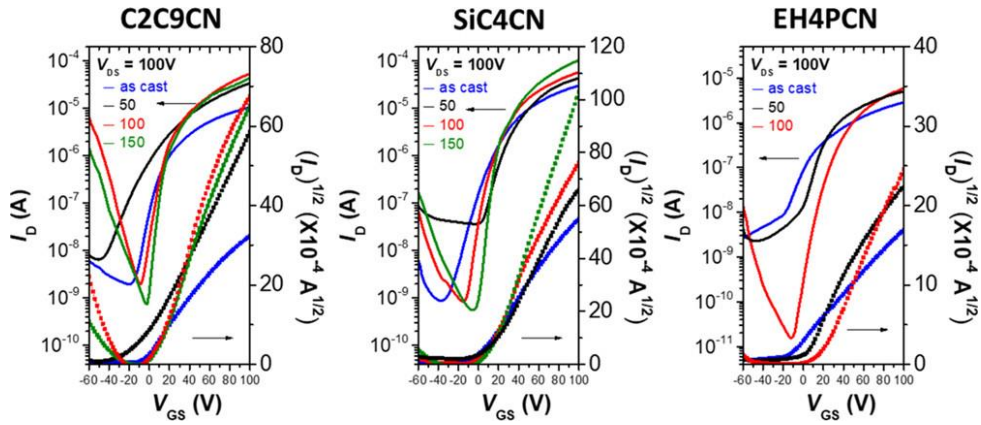

Figure 2.11. Transfer curves of the n-type devices of DPP small molecules.

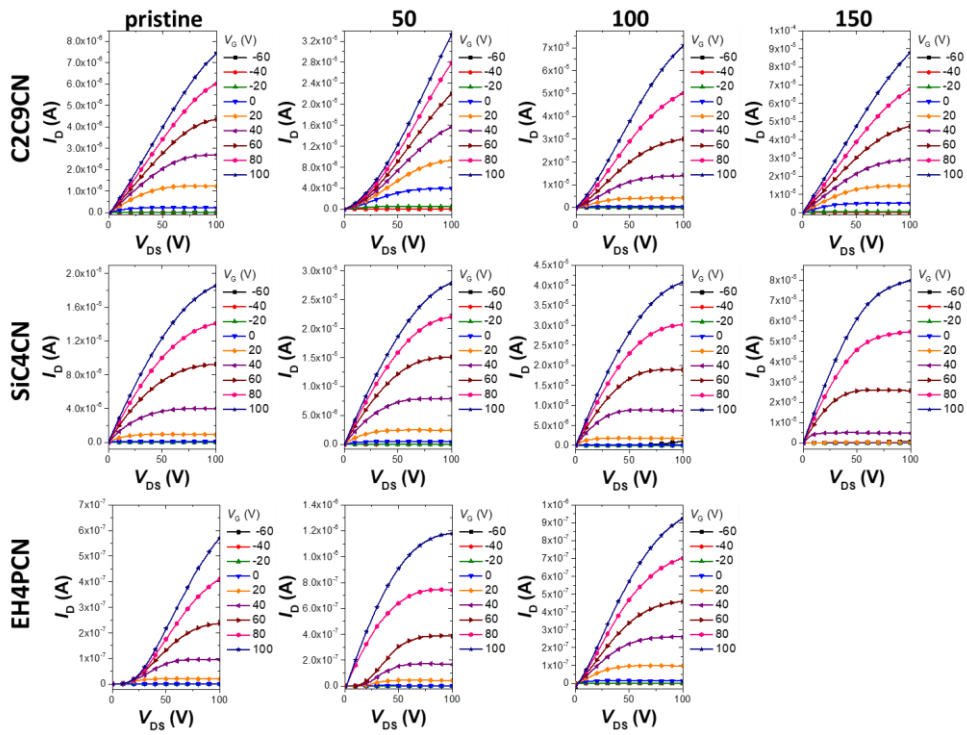

Figure 2.12. The output curves of the DPP small molecule-based FET devices.

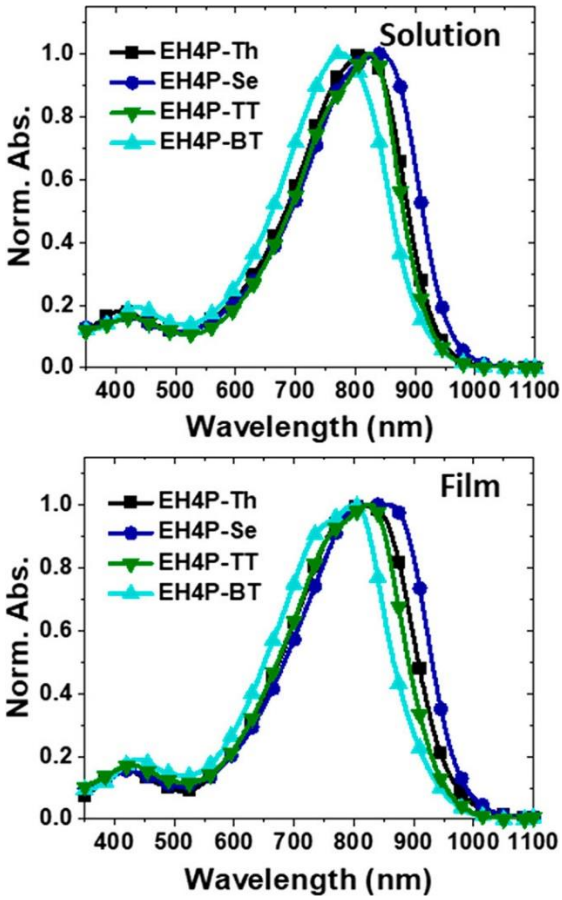

Figure 2.13. Absorption profiles of the polymers (a) in dilute chlorobenzene solution and (b) as thin films on a quartz plate.

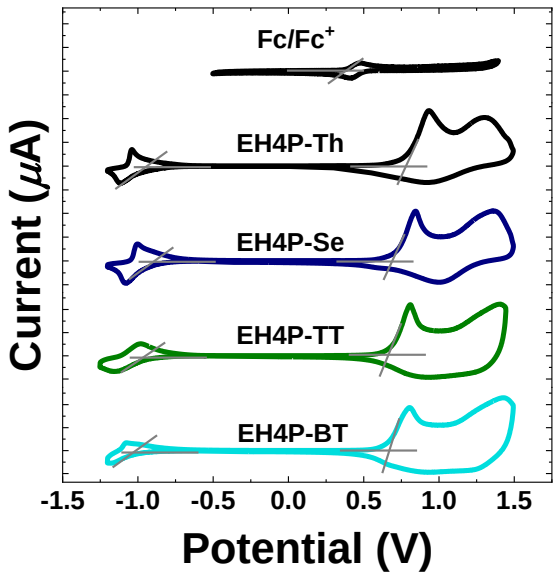

Figure 2.14. Cyclic voltammograms of the polymer films in *n*-Bu_4NPF_6/CH_3CN solution (scan rate, 100 mVs^{-1}).

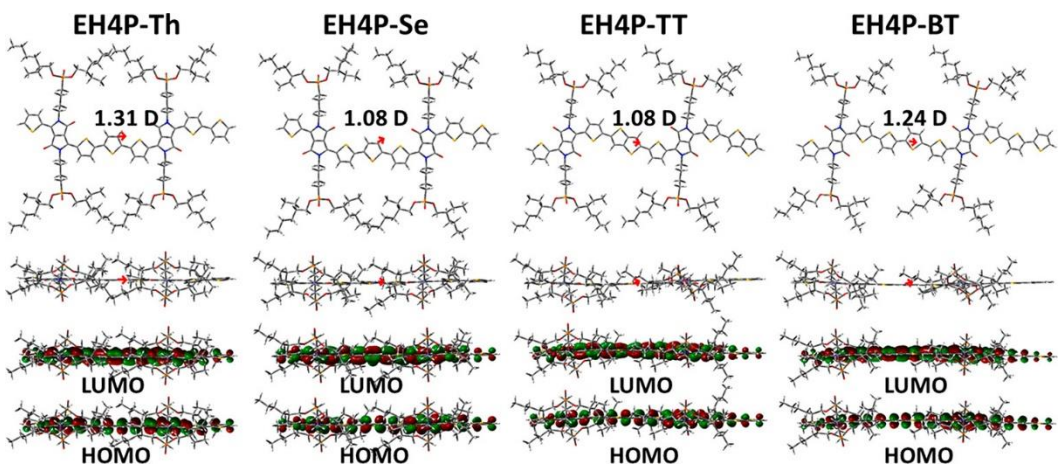

Figure 2.15. DFT calculation results: illustrated dipole moments on the energy-minimized structures (top) and charge-density isosurfaces for the model system (bottom) of the dimeric units.

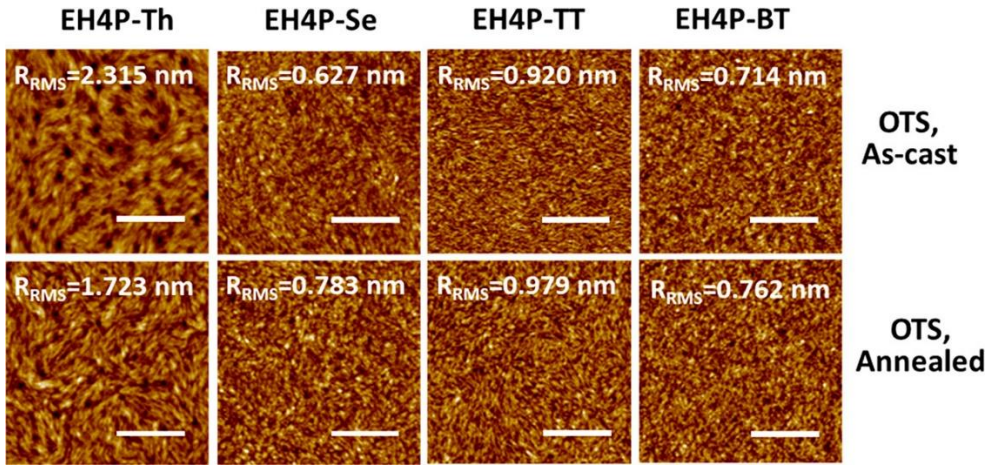

Figure 2.16. AFM height images (3 × 3 μm^2) of the polymer films. R_{RMS} is rms roughness of the film. Scale bar = 1 μm.

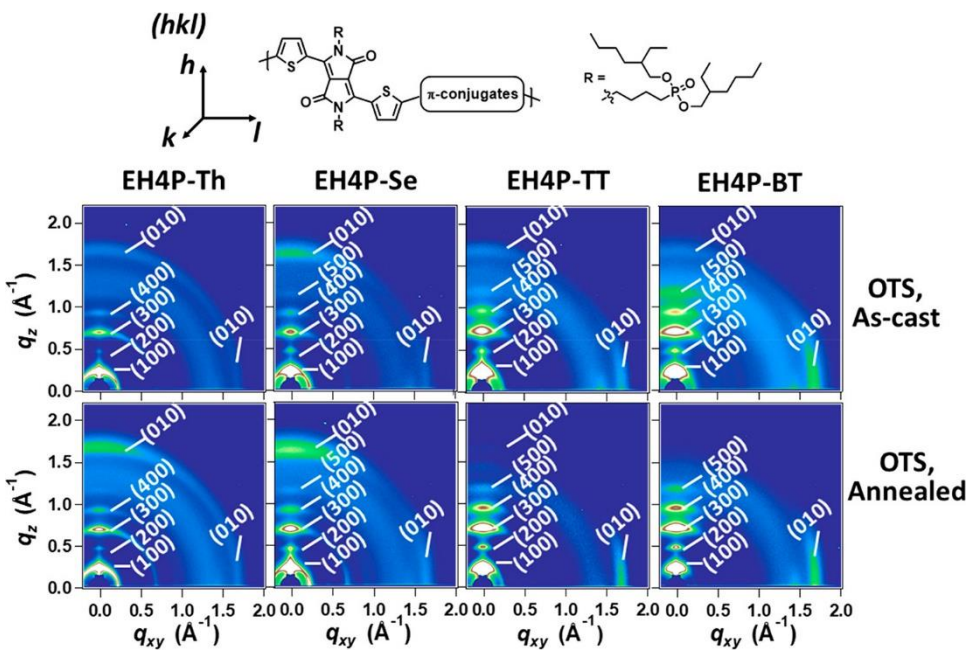

Figure 2.17. 2D-GIXD images of the polymer films.

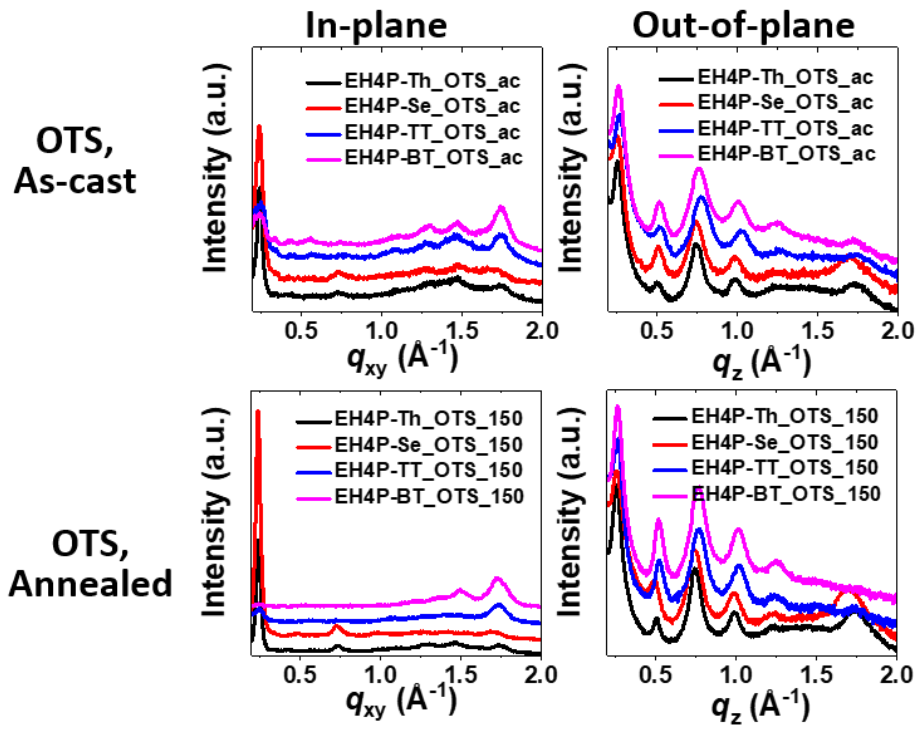

Figure 2.18. 1D linecut profiles of the 2D-GIXD images of films on OTS-treated substrates.

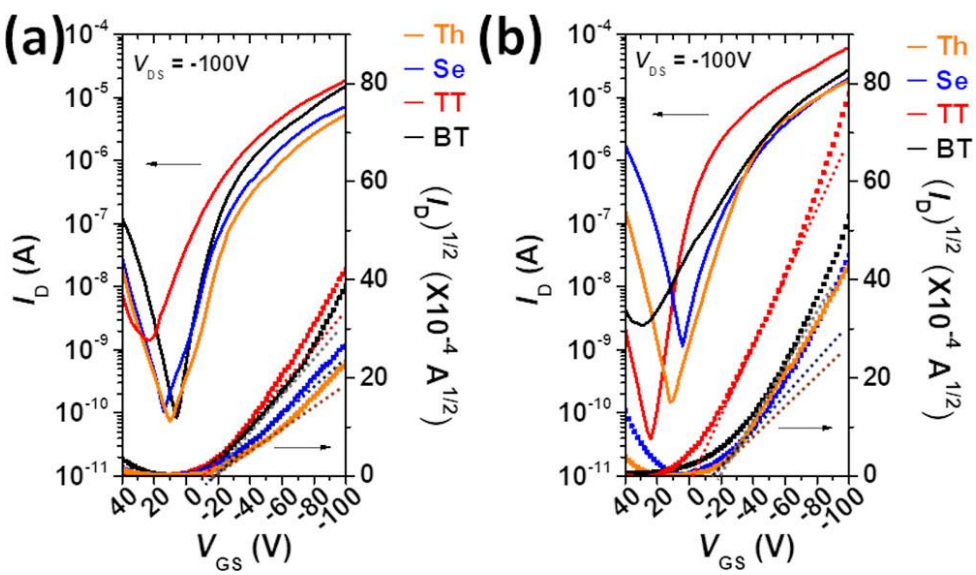

Figure 2.19. Transfer curves of the p-type devices with (a) as-spun and (b) annealed polymer films fabricated using polymer solution in chloroform on OTS-treated substrate.

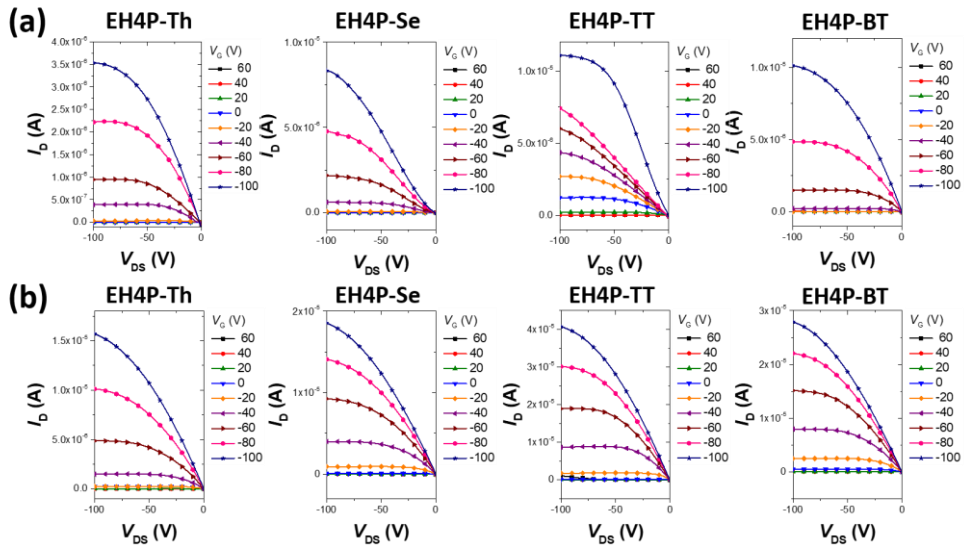

Figure 2.20. The output curves of the phosphonate polymer-based FET devices with (a) as-spun and (b) annealed polymer films.

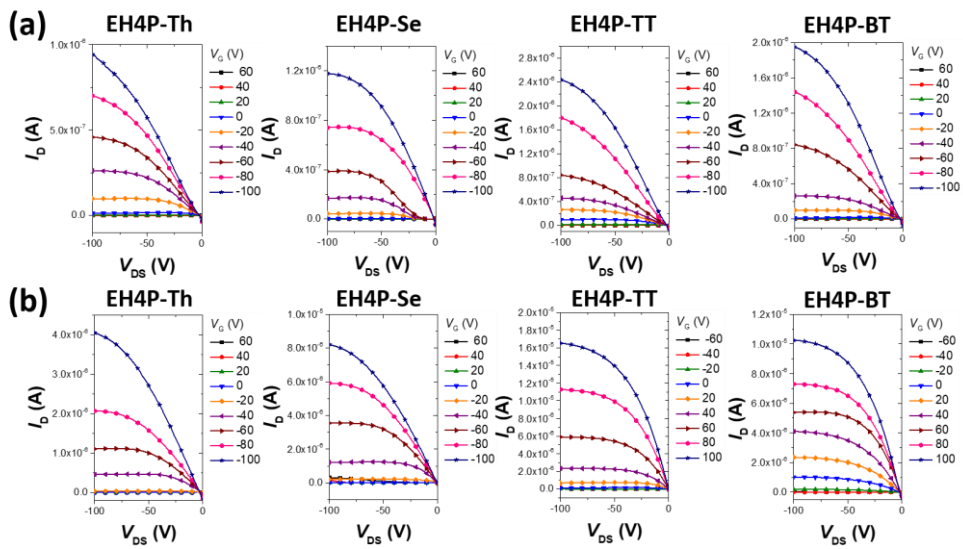

Figure 2.21. The output curves of the phosphonate polymer-based FET devices fabricated using (a) OTS-untreated substrate and (b) polymer solution in MeTHF.

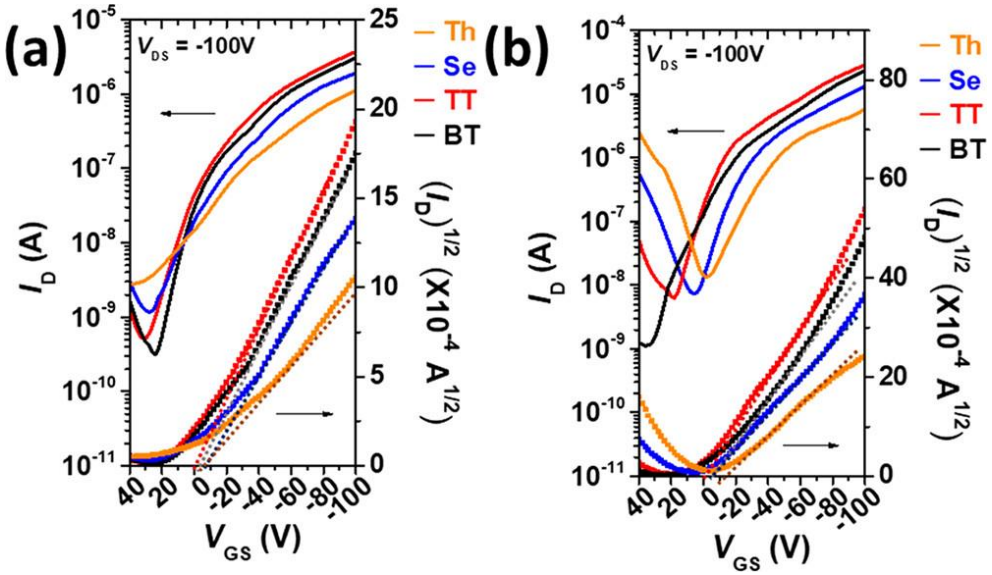

Figure 2.22. Transfer curves of the p-type devices fabricated using (a) polymer solution in chloroform and OTS-untreated substrate and (b) polymer solution in MeTHF and OTS-treated substrate.

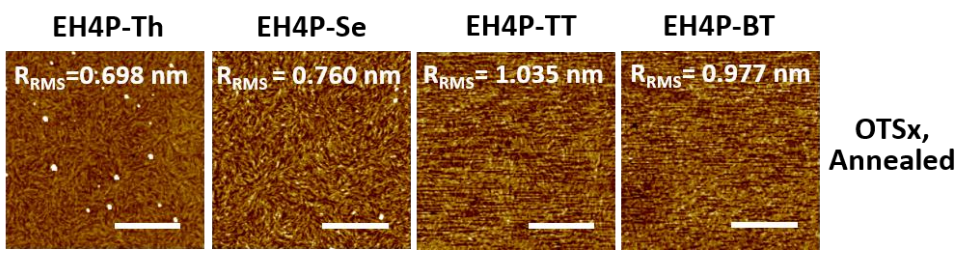

Figure 2.23. AFM height images of the polymer films on OTS-untreated substrates.

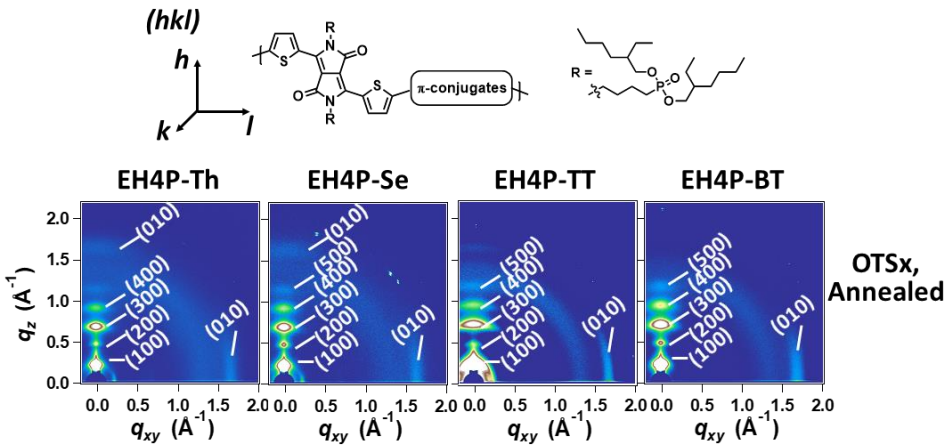

Figure 2.24. 2D-GIXD images of the polymer films on OTS-untreated substrates.

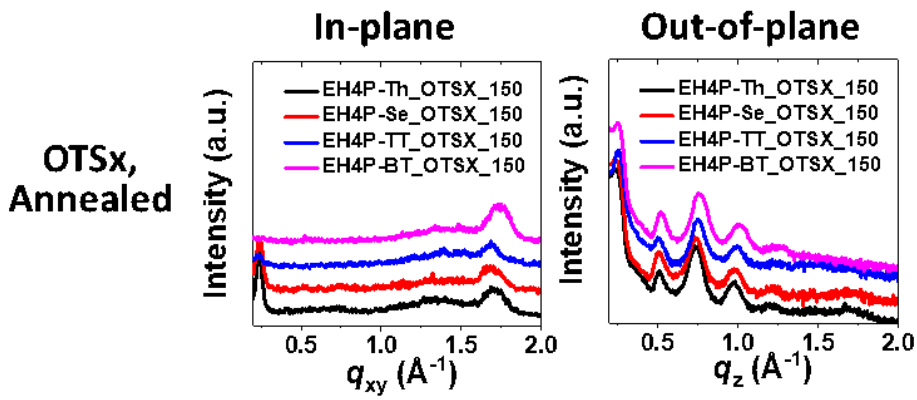

Figure 2.25. 1D linecut profiles of the 2D-GIXD images of the polymer films on OTS-untreated substrates.

	λ_{sol}^{max} (nm)	λ_{film}^{max} (nm)	redshift	λ_{onset} (nm)	E_g^{opt} (eV)	E_{HOMO}	E_{LUMO}
C2C9CN	641, 696	701, 760	+64	861	1.44	-5.59	-4.09
SiC4CN	641, 695	681, 754	+59	830	1.49	-5.60	-4.10
EH4PCN	636, 690	685, 746	+56	837	1.48	-5.66	-4.16

Table 2.1. The photophysical and electrochemical properties of DPP small molecules.

	T_a [°C]	Lamellar spacing [b]			π-π spacing [c]		
		$q_{z\,(100)}$ [Å^{-1}]	$d_{z\,(100)}$ [Å]	CCL [nm]	$q_{xy\,(010)}$ [Å^{-1}]	$d_{xy\,(010)}$ [Å]	CCL [Å]
C2C9CN	As-cast	0.304	20.67	19.42	-	-	-
	50	0.305	20.60	17.88	-	-	-
	100	0.312	20.14	41.65	-	-	-
	150	0.315	19.95	42.95	-	-	-
SiC4CN	As-cast	0.303	20.75	18.56	1.780	3.53	39.80
	50	0.303	20.75	39.95	1.740	3.61	45.06
	100	0.303	20.75	44.00	1.700	3.70	46.78
	150	0.303	20.76	54.68	1.760	3.57	48.51
EH4PCN	As-cast	0.264	23.83	39.76	1.780	3.53	15.93
	50	0.265	23.75	48.98	1.797	3.50	15.64
	100	0.265	23.71	118.19	1.788	3.51	47.07
	150	0.251	25.03	132.61	1.760	3.57	28.47

[a]The parameters were calculated from GIXD profiles; The parameters for [b]the lamellar spacing and [c]the π-π spacing were derived from the (100) and (010) peaks, respectively.

Table 2.2. 2D-GIXD crystallographic parameters of DPP small molecule films at different annealing conditions.[a]

	Annealing Condition	μ_{max}[a] [$cm^2V^{-1}s^{-1}$]	μ_{avg}[b] [$cm^2V^{-1}s^{-1}$]	μ_{eff} [$cm^2V^{-1}s^{-1}$]	r [%]	I_{on}/I_{off}	V_T [V]
C2C9CN	pristine	1.56×10^{-2}	1.51×10^{-2} (± 0.0005)[c]	4.56×10^{-3}	29	$> 10^3$	-8.0
	50 ℃	2.82×10^{-2}	2.47×10^{-2} (± 0.0025)	1.51×10^{-2}	54	$> 10^3$	-10.9
	100 ℃	8.95×10^{-2}	6.88×10^{-2} (± 0.0037)	3.31×10^{-2}	37	$> 10^3$	2.1
	150 ℃	8.63×10^{-2}	6.52×10^{-2} (± 0.0050)	2.41×10^{-2}	28	$> 10^4$	5.4
SiC4CN	pristine	4.26×10^{-2}	3.93×10^{-2} (± 0.0015)	1.35×10^{-2}	32	$> 10^4$	-3.1
	50 ℃	7.57×10^{-2}	6.49×10^{-2} (± 0.0059)	1.84×10^{-2}	24	$> 10^3$	4.8
	100 ℃	1.16×10^{-1}	9.26×10^{-2} (± 0.0102)	2.56×10^{-2}	22	$> 10^4$	1.2
	150 ℃	1.59×10^{-1}	1.25×10^{-1} (± 0.02802)	2.60×10^{-2}	16	$> 10^5$	9.8
EH4PCN	pristine	2.67×10^{-3}	2.30×10^{-3} (± 0.0002)	1.22×10^{-3}	46	$> 10^3$	-20.4
	50 ℃	1.02×10^{-2}	7.26×10^{-3} (± 0.00172)	2.15×10^{-3}	21	$> 10^3$	0.6
	100 ℃	1.15×10^{-2}	8.86×10^{-3} (± 0.0015)	3.04×10^{-3}	26	$> 10^5$	13.9
	150 ℃	-	-	-	-	-	-

Table 2.3. OFET performance of DPP-based polymer films blow-casted under different annealing conditions. [a]The maximum mobility of the FET devices (L=50 μm and W = 1000 μm). [b]The average mobility of 10 FET devices (L=50 μm and W = 1000 μm). [c]The standard deviation.

	λ_{max}^{sol} [nm]	λ_{max}^{film} [nm]	λ_{onset} [nm]	E_g^{opt} [eV]	E_{HOMO} [eV]	E_{LUMO} [eV]	M_v [kDa]
EH4P-Th	816	824	960	1.29	-5.18	-3.61	74.6
EH4P-Se	840	837	978	1.27	-5.13	-3.58	60.5
EH4P-TT	824	824	944	1.31	-5.09	-3.51	44.7
EH4P-BT	776	800	932	1.33	-5.07	-3.44	58.8

Table 2.4. Photophysical and electrochemical properties of the polymers.

	Vector			Dipole Moment [D]	E_{HOMO}^{DFT} [eV]	E_{LUMO}^{DFT} [eV]
	x	y	z			
EH4P-Th	1.3058	0.0116	-0.1159	1.3110	-4.94	-3.14
EH4P-Se	1.0001	0.4004	0.0785	1.0801	-4.91	-3.12
EH4P-TT	0.9839	-0.2632	0.3614	1.0807	-4.94	-3.16
EH4P-BT	1.1633	-0.2709	0.3521	1.2452	-4.89	-3.12

Table 2.5. Calculated dipole moments and energy levels of the dimeric units of the polymers by DFT.

	condition	Lamellar spacing[a]				π-π spacing			
		$q_{(100)}$ [Å^{-1}]	$d_{(100)}$ [Å]	FWHM [Å^{-1}]	$L_{c\,(100)}$ [Å]	$q_{(010)}$ [Å^{-1}]	$d_{(010)}$ [Å]	FWHM [Å^{-1}]	$L_{c(010)}$ [Å]
EH4P-Th	As-cast	0.243	25.89	0.038	149.79	1.744[b] /1.729[c]	3.60[b] /3.63[c]	0.115[b] /0.106[c]	49.68[b] /53.98[c]
	Annealed	0.242	25.95	0.037	151.64	1.757[b] /1.738[c]	3.58[b] /3.61[c]	0.089[b] /0.082[c]	64.64[b] /69.75[c]
EH4P-Se	As-cast	0.241	26.12	0.047	121.25	-[b] /1.699[c]	-[b] /3.70[c]	-[b] /0.108[c]	-[b] /52.96[c]
	Annealed	0.241	26.05	0.036	158.61	-[b] /1.701[c]	-[b] /3.69[c]	-[b] /0.086[c]	- /66.51[c]
EH4P-TT	As-cast	0.251	25.08	0.064	88.57	1.748[b]	3.60[b]	0.095[b]	60.50[b]
	Annealed	0.249	25.20	0.060	94.07	1.736[c]	3.62[c]	0.072[c]	78.14[c]
EH4P-BT	As-cast	0.242	25.97	0.062	90.94	1.744[b]	3.60[b]	0.040[b]	61.35[b]
	Annealed	0.251	25.03	0.057	99.95	1.737[c]	3.62[c]	0.081[c]	69.95[c]

The parameters were calculated from GIXD profiles of the as-cast films and thermally annealed films at 150 °C on OTS-treated substrates. [a]The parameters for the lamellar spacing were derived from the (100) peaks along the out-of-plane direction. The parameters for the π-π spacing were derived from the (010) peaks along the [b]in-plane and [c]out-of-plane direction.

Table 2.6. Crystallographic parameters of phosphonate DPP polymer films on OTS-treated substrates.[a]

Polymer	OTS Treatment	Annealed Condition	μ_{max} $(cm^2V^{-1}s^{-1})$	μ_{avg}[b] $(cm^2V^{-1}s^{-1})$	I_{on}/I_{off}	V_T (V)
EH4P-Th	Treated	Non-annealed	1.67×10^{-2}	1.24×10^{-2} (± 0.0030)[c]	$> 10^4$	-15.0
	Treated	150 ℃	3.69×10^{-2}	2.88×10^{-2} (± 0.0057)	$> 10^5$	-18.3
EH4P-Se	Treated	Non-annealed	2.26×10^{-2}	1.70×10^{-2} (± 0.0046)	$> 10^5$	-15.3
	Treated	150 ℃	5.81×10^{-2}	4.50×10^{-2} (± 0.0087)	$> 10^4$	-23.1
EH4P-TT	Treated	Non-annealed	9.63×10^{-2}	8.21×10^{-2} (± 0.0092)	$> 10^4$	-8.0
	Treated	150 ℃	1.46×10^{-1}	1.23×10^{-1} (± 0.016)	$> 10^6$	-1.9
EH4P-BT	Treated	Non-annealed	6.45×10^{-2}	5.67×10^{-2} (± 0.0152)	$> 10^4$	-9.8
	Treated	150 ℃	1.16×10^{-1}	9.14×10^{-2} (± 0.0120)	$> 10^4$	-21.8

Table 2.7. Electrical characteristics of *p*-type devices of phosphonate DPP polymers. [a]The maximum mobility of the FET devices (L=50 μm and W = 1000 μm). [b]The average mobility of 10 FET devices with [c]the standard deviation.

Polymer	OTS Treatment	Annealed Condition	μ_{max} $(cm^2V^{-1}s^{-1})$	μ_{avg}[b] $(cm^2V^{-1}s^{-1})$	I_{on}/I_{off}	V_T (V)
DPP-Th	Untreated	150 ℃	1.58×10^{-3}	1.05×10^{-3} (± 0.00023)	$> 10^2$	-3.5
DPP-Se	Untreated	150 ℃	2.71×10^{-3}	1.88×10^{-3} (± 0.00043)	$> 10^3$	-6.2
DPP-TT	Untreated	150 ℃	6.10×10^{-3}	4.68×10^{-3} (± 0.00080)	$> 10^3$	-0.1
DPP-BT	Untreated	150 ℃	3.73×10^{-3}	2.38×10^{-3} (± 0.00077)	$> 10^3$	-3.2

Table 2.8. Electrical characteristics of the p-type devices fabricated using OTS-untreated substrates.

	condition	Lamellar spacing[a]				π-π spacing[b]			
		$q_{(100)}$ [Å^{-1}]	$d_{(100)}$ [Å]	FWHM [Å^{-1}]	$L_{c\,(100)}$ [Å]	$q_{(010)}$ [Å^{-1}]	$d_{(010)}$ [Å]	FWHM [Å^{-1}]	$L_{c(010)}$ [Å]
EH4P-Th	Annealed	0.239	26.32	0.043	132.90	1.713	3.67	0.134	42.79
EH4P-Se	Annealed	0.240	26.13	0.046	121.35	1.699	3.70	0.142	40.37
EH4P-TT	Annealed	0.237	26.47	0.068	81.47	1.691	3.72	0.094	60.66
EH4P-BT	Annealed	0.248	25.39	0.060	96.86	1.727	3.64	0.211	57.87

The parameters were calculated from GIXD profiles of thermally annealed films at 150 ° C on OTS-treated substrates. The parameters for [a]the lamellar spacing and [b]the *π-π* spacing were derived from the (100) peaks along the out-of-plane direction and (010) peaks along the in-plane direction, respectively.

Table 2.9. Crystallographic parameters of phosphonate DPP polymer films on OTS-untreated substrates.

Polymer	OTS Treatment	Annealing Condition	μ_{max} $(cm^2V^{-1}s^{-1})$	I_{on}/I_{off}	V_T (V)
PDPP-Th	Treated	150 ann	1.76×10^{-2}	$> 10^2$	-12.7
PDPP-Se	Treated	150 ann	2.64×10^{-2}	$> 10^3$	-2.6
PDPP-TT	Treated	150 ann	4.72×10^{-2}	$> 10^3$	-0.7
PDPP-BT	Treated	150 ann	3.46×10^{-2}	$> 10^4$	-2.1

Table 2.10. Electrical characteristics of the p-type devices fabricated using MeTHF.

Chapter 3

Role of Side Chain Engineering in DAP-based OFETs and their application in optoelectronic devices

3. 1. Introduction

Low bandgap π-conjugated polymers, that absorb in the near-infrared (NIR) range (760-1100 nm) with a typical bandgap smaller than 1.6 eV, are an interesting family of semiconductor materials, and have enabled many recent exciting breakthroughs in various functional optoelectronic applications, such as organic field-effect transistors (OFETs), organic photodetectors (OPTs), electrochromic devices, and so on. In fact, incorporating a quinoid structure into the polymer backbone is a powerful strategy for reducing the bandgap, which has been verified by theoretical and experimental studies of the well-known low bandgap poly(isothianaphthene) and poly-(thieno[3,4-b]pyrazine) with low bandgaps less than 1.0 eV. However, such quinoid-type polymers typically have too small bandgap and poor stability toward oxidation, which makes them difficult to be employed in the aforementioned devices. Alternatively, utilizing donor-acceptor (D-A) interactions (so-called D-A type copolymers) is emerging as a mainstream approach for constructing low bandgap polymers in which electron-rich (donor) and electron-deficient (acceptor) building units are alternately regulated along the backbone. The D-A type copolymers offer the unique feature of almost independently tuning the energy levels (highest occupied molecular orbital (HOMO)/lowest unoccupied molecular orbital (LUMO) levels) and the bandgaps. Thus, introducing a strong acceptor unit into the main backbone can lower the LUMO while almost maintaining the low HOMO, thereby, leading to the reduced bandgap and the improved stability against oxidization of the resulting copolymers.

Imide- or amide-containing dyes have been widely studied as attractive, strong acceptor building blocks for low bandgap D-A type copolymers. In particular, diketopyrrolopyrrole (DPP), that is a symmetrical, planar, and strong acceptor molecule with pyrrole-based quinoid characteristics as well as excellent chemical and photochemical stability, is now recognized to be the most successful dye for constructing high-performance low bandgap D-A copolymers, which are widely

exploited in a wide range of the optoelectronic devices including the above-mentioned ones. With the extensive research and development activity in DPP chemistry, a bicyclic 2,5-diazapentalene (DAP) dye was recently formulated as an analogous lactim structure of DPP. The DAP has endocyclic carbon-nitrogen double bond that lacks basic lone-pair electrons on the nitrogen, leading to its lower-lying HOMO/LUMO with the reduced bandgap compared to DPP, as evidenced by our calculations (see **Figure 3.1**b). The electrostatic potential maps also represent more electron-deficient (stronger accepter) property of DAP than DPP (**Figure 3.1**a). Therefore, we believe that many low bandgap D-A copolymers with unique and interesting properties can be developed by incorporating DAP into various D-A type systems. Nevertheless, literature reports on the synthesis, characterization, and optoelectronic properties of the DAP-based copolymers are rarely seen.

With the aim of widening library and understanding of copolymers incorporating DAP unit, not only do we report the synthesis of a series of ultra-low bandgap D-A copolymers based on DAP (PDAP-Fu, PDAP-Th, and PDAP-Se), by polymerizing chalcogenophene donor moieties, furan (Fu), thiophene (Th), and selenophene (Se) with the DAP acceptor unit, but comparative studies of the resulting copolymers also represent a step toward a structure-property relationship regarding the chalcogen atoms' effects on intrinsic properties including energetics, morphology, molecular packing, charge transport, and photo-detectivity. In OFET studies, all the copolymers show high field-effect hole mobilities and high I_{on}/I_{off} ratios ($\geq 10^5$) and a best hole mobility of 4.76×10^{-1} cm^2 V^{-1} s^{-1} is achieved in PDAP-Se. Besides, we also demonstrate their high-performing NIR OPTs with excellent external quantum efficiency (EQE, η) up to 6.56×10^4 % and photodetectivity (D*) up to 1.80×10^{12} Jones under 1060 nm light illumination. Our study will revitalize the DAP accepting unit and contribute to further development of the DAP-based semiconductors, ultimately discovering its full potential merits as conjugated backbone.

3.2. Experimental Section

3.2.1. Materials and Instrument

All chemicals and reagents used for was purchased from Sigma Aldrich, Alfa Aesar Chemical Company, and Tokyo Chemical Industry Co., Ltd, and used without any further purification. All solvents are ACS and anhydrous grade by distillation. 3,6-Di(thiophen-2-yl)pyrrolo[3,4-c]pyrrole-1,4(2H,5H)-dithione and its counterpart monomers of 2,5-bis(trimethylstannyl)furan, 2,5-bis-(trimethylstannyl)thiophene, and 2,5-bis-(trimethylstannyl)selenophene were prepared according to reported procedures. Cyclic voltammetry measurements were performed on an AMETEK Versa STAT 3 with a three-electrode cell system in a nitrogen bubbled 0.1 M n-Bu4NPF6 solution in acetonitrile at a scan rate of 100 mV s^{-1} at room temperature. An Ag/Ag+ electrode, platinum wire, and platinum were used as the reference electrode, counter electrode, and working electrode, respectively. The Ag/Ag+ reference electrode was calibrated using a ferrocene/ferrocenium redox couple as an external standard, whose oxidation potential is set at –4.8 eV with respect to a zero-vacuum level. The HOMO energy levels were obtained from the equation, E_{HOMO} (eV) = $-(E_{ox}^{onset} - E_{1/2}^{ferrocene} + 4.8)$. The LUMO energy levels were calculated by the equation, E_{LUMO} (eV) = $E_{HOMO} + Eg^{opt}$. DFT calculations were performed using the Gaussian 09 package with the nonlocal hybrid Becke three-parameter Lee–Yang–Parr (B3LYP) function and the 6-31G+** and 6-31G* basis set to elucidate the theoretically calculations of the cores and copolymers.

3.2.2. Thin-Film Microstructure Analyses

Samples for thin-film microstructure analyses were prepared by spin coating the solution of copolymers (3 mg mL^{-1} in chlorobenzene (CB)) onto n-SiO_2/Si substrates. Tapping-mode atomic force microscopy (AFM) and grazing incidence X-ray diffraction (GIXD) analyses were conducted to investigate the thin-film

morphology and molecular packing. AFM images were obtained by a MultiMode 8 scanning probe microscope running with a Nanoscope-V controller with a scan size of 3 μm. GIXD data were acquired at PLS-II 9A U-SAXS beamline of Pohang Accelerator Laboratory in Korea. X-ray beam at 11.015 keV (λ = 1.12556 Å) was obtained by monochromating the X-rays coming from the in-vacuum undulator (IVU) by a double crystal monochromator. The X-ray beam was irradiated in the incidence angle of < 0.14 ° and for 1 ~ 30 s. GIXD patterns were recorded by a 2D CCD detector with the sample-to-detector distance (SDD) of 222.0 mm.

Approximate crystalline correlation length, Lc, was extracted using Scherrer equation:

$$L_{\mathrm{c}} = \frac{K \cdot \lambda}{\mathrm{FWHM} \cdot cos\theta}$$

3.2.3. OFET Fabrication and Measurement

Bottom-gate and top-contact OFETs were fabricated by solution-processing of the polymer semiconducting solutions (3 mg mL^{-1}) in anhydrous CB and spin-coating with coating speed of 1000 rpm for 60 s and 500 rpm for 30 s. After thermal annealing at 150 ℃ for 30 min, source and drain electrodes were thermally evaporated on the polymer films using Au and a shadow mask with a channel length (L) of 50 μm and a width (W) of 1000 μm. A Keithley 4200-SCS semiconductor parametric analyzer was used to measure the electrical characteristics of the developed OFETs. The charge carrier mobility was derived from the following equation in the saturation regime:

$$I_{\mathrm{DS}} = \frac{W}{2L}\mu C_{\mathrm{i}}(V_{\mathrm{G}} - V_{\mathrm{T}})$$

where I_{DS} is the drain-to-source current, μ is the charge mobility, V_{G} is the gate voltage, and V_{T} is the threshold voltage. The reliability factor (r) was derived using the follwing equation:

$$r = \left(\frac{\sqrt{|I_{DS}|^{max}} - \sqrt{|I_{DS}|^{0}}}{|V_G|^{max}} \right)^2 \Bigg/ \left(\frac{\partial \sqrt{|I_{DS}|}}{\partial V_G} \right)^2$$

where $|I_{DS}|^{max}$ is the maximum drain-to-source current at the maximum gate voltage ($|V_G|^{max}$), $|I_{DS}|^{0}$ is the drain-to-source current at $V_G = 0$.

3.3. Results and Discussion

3.3.1. Materials Synthesis and Characterization

The materials were synthesized by Seoyoung Kim from UNIST. The number-average molecular weight (M_n) and polydispersity index (PDI) were determined using high-temperature gel permeation chromatography at 100 ℃ in 1,2,4-trichlorobenzene as an eluent. They have similar, high M_ns of 64.1 to 67.1kDa with narrow PDIs of 1.70 to 1.85, which allows us to properly carry out a systematic study on the copolymer series with a minimal M_n's effect on the optical and electrochemical properties and device performances.

UV–Vis–NIR absorption spectra of the DAP-based copolymers were measured both in dilute chloroform solution and thin film (**Figure 3.2**(a) and (b)). All the copolymers have two characteristic absorption bands consisting of a sharp π–π* transition one at high energy (350−550 nm) and a broader intermolecular charge transfer (ICT) one at low energy region (600−1400 nm). As observed in many other D–A copolymers, DAP-based copolymers showed a red-shift in the maximum absorptions (λ_{max}) upon transitioning from solution to films, especially for the larger, more polarizable sulfur- and selenium-involved PDAP-Th and PDAP-Se. Additionally, we also observed slightly more red-shifted λ_{max}s with increasing the heteroatomic size of the chalcogenophene counterparts (Fu < Th < Se) in the backbones, being in accordance with their order of electron-donating strength. The copolymers have similar optical bandgaps (E_g^{opt}s) of ~1.00 eV.

Cyclic voltammetry was measured to compare the frontier energy levels of the copolymers (**Figure 3.2**c and **Table 3.1**). The copolymer films were deposited on the glassy carbon electrode in an acetonitrile solution containing 0.1 M *n*-Bu_4NPF_6, and recorded versus the Ag/Ag^+ redox couple under an inert atmosphere with ferrocene/ferrocenium redox couple as internal standard. The HOMO and LUMO calculated from each of the equations (HOMO (eV) = –4.8 –($E_{ox}^{onset} – E_{1/2}^{ferrocene}$) and

LUMO (eV) = HOMO + E_g^{opt}, respectively) are schematically described in **Figure 3.2**(c). Both the HOMO and LUMO levels gradually deepened in the order from PDAP-Se to PDAP-Fu to PDAP-Th. It is interesting to note that the above-observed results are in contrast to the previous set of chalcogenophene-based copolymers; in which replacing Th with Fu unit lowers the HOMO with a larger E_g^{opt}, whereas incorporating Se somewhat selectively lowers the LUMO with a smaller E_g^{opt}. Thus, one can conclude that the changing trend of the optical and electrochemical properties is strongly dependent on the nature of the acceptor monomers used in the chalcogenophene-based polymers.

Density functional theory (DFT) simulation (B3LYP/6-31G* basis set) of the copolymers was performed to investigate their electron density distributions and optimized molecular structures, where each of the tetrameric models was used for the calculation study. As shown in **Figure 3.2**e, in addition to their similar electron-density distributions, all the copolymer models featured a high coplanar structure with very small dihedral angle less than 0.1 °. We also note that in spite of their identical direction for all the cases, higher internal dipole moments are observed in PDAP-Fu and PDAP-Se relative to PDAP-Th, which may cause a strong intermolecular dipole interaction.

3.3.2. Thin-Film Microstructure Analysis

To address structure-property relationship in the microstructures and crystallinity, the DAP-based copolymer films were characterized by using atomic force microscopy (AFM) and grazing incidence X-ray diffraction (GIXD). The thin films were fabricated by spin-coating at 1000 rpm for 60 s on *n*-OTS-modified SiO_2/Si substrates and subsequently annealed at an optimal temperature of 150 ℃, which was determined from the following OFET devices. As seen from the AFM images in the upper right of **Figure 3.3**a-c and **Figure 3.4**, all the thin films showed increasingly textured surface morphology after the annealing process. Notably, the

annealed PDAP-Se film appears to exhibit a more isotropic nanofibrillar structure with a smaller root mean square roughness (R_{rms}) of 0.511 nm compared with the other films.

Figure 3.3a–c shows the GIXD patterns of the annealed copolymer films (see **Figure 3.5** for the as-cast films), and **Figure 3d-f** and **Table 3.2** provides the detailed diffractogram profiles (see **Figure 3.6** for the as-cast films), including packing distances and crystalline coherence lengths (L_cs). Upon annealing, the diffraction peaks of the films became sharper and stronger, suggesting an enhanced crystallinity.[45] We summarize the interesting GIXD features of the films annealed at the optimal temperature of 150 °C as follows: (i) All the films show long-ranged multi diffraction (*h00*) peaks, which is indicative of the ordered layer-by-layer lamellar packing motif. (ii) PDAP-Fu displays an intense (*010*) π–π stacking peak along the q_z plane, suggesting a preference for face-on orientation, whereas PDAP-Th favorably adopts an edge-on packing, as evidenced by the (*010*) π–π stacking peak along the q_{xy} plane. Besides, the (*010*) π–π stacking peaks along both the q_z and q_{xy} planes are clearly observed, revealing the mixed edge-on and face-on orientations of the polymer chains. (iii) Relative to the others, PDAP-Se has larger (*100*) lamellar and (*010*) π–π L_c values determined by the Scherrer equation.[46] Overall, the aforementioned GIXD data demonstrate that PDAP-Se tends to form a three-dimensional (3D) charge-conduction channel through the edge-on and face-on mixed larger crystallites, whereas both PDAP-Fu and PDAP-Th kinetically favor a two-dimensional channel formation, with the channel being parallel to the substrate for the former and perpendicular to the substrate for the latter, when used in the electronic device tests.[45, 47, 48]

3.3.3. Electrical Characteristics of OFETs

First, to estimate the charge transport abilities of the DAP-based copolymer thin films, we fabricated bottom-gate and top-contact OFETs under a nitrogen

atmosphere using Si/SiO_2 as the gate and gate dielectric layer. The copolymer-active layer was deposited via the spin coating process onto Si/SiO_2 and was then subjected to thermal annealing first at 100 °C and subsequently at 150 °C. The details of the fabrication process and measurements are described in the Experimental Section. All the DAP-based copolymers showed typical unipolar *p*-type field-effect characteristics with high I_{on}/I_{off} ratios ($\geq 10^4$). **Table 3.3** lists their superior electrical properties and average values of mobilities for all the cases. **Figure 3.7** displays the representative transfer curves for the devices annealed at 150 °C, at which temperature the DAP copolymers showed the best electrical properties (see **Figure 3.8** for the as-cast films), and **Table 3.4** summarizes the corresponding OFET data. The hole mobilities in the optimized OFETs increased according to the following relationships: PDAP-Fu (1.57×10^{-1} cm^2 V^{-1} s^{-1}) < PDAP-Th (2.08×10^{-1} cm^2 V^{-1} s^{-1}) < PDAP-Se (4.76×10^{-1} cm^2 V^{-1} s^{-1}).

The superior OFET performance of PDAP-Se originated from a combination of the formation of the 3D charge transport channel and the improved crystallinity *via* the formation of fibril-like microstructures, as revealed by morphological studies.[49, 50] Additionally, we calculated the effective charge mobility (μ_{eff}) to improve the reliability of the mobility evaluation of the OFETs reported in this study. The reliability factor (*r*) of the mobilities measured in an N_2-filled glove box was 39–44%. The nonideal behaviors of the OFETs with low *r* and effective mobilities could be due to the difference found in the threshold voltage compared with that of the ideal device (where the threshold voltage is 0 V). The nonlinearity in the transfer curves of the OFETs is known to originate from various factors, including contact effects, carrier density-dependent mobility, nonequilibrium biasing of short-channel OFETs, and minority carrier injection and trapping.[51-53]

3.3.4. NIR-Sensing OPTs

Driven by their simultaneous high NIR absorption and high carrier mobility, we investigated the photoresponse performance of NIR OFETs on the basis of DAP-based copolymers. The OPT devices were fabricated in the bottom-gate and top-contact configuration with the same conditions as for the abovementioned OFETs (**Figure 3.9**a). First, we evaluated the optoelectronic properties of the OPT devices in the dark and under monochromic NIR light illumination (λ = 1060 nm) with an intensity of 0.95–1.05 mW cm^{-2}. As expected, all the OPT devices showed *p*-type transfer curves for the OFETs, in which the drain current was significantly increased under NIR light exposure, thus demonstrating a high NIR photosensitivity (**Figure 3.9**b). Typically, the photocurrent (I_{ph}) is defined as $I_{ph} = I_{light} - I_{dark}$, where I_{light} is the drain current under light illumination, and I_{dark} is the drain current in the dark. On the basis of the measurements of I_{ph} using transfer characteristics, the photoresponsivity (R) and photocurrent/dark current ratio (P) could be obtained; R is defined as the ratio of the generated photocurrent to the incident illumination power (P_{inc}), and P represents the ratio of the photocurrent to the dark current. R and P are expressed by the following equations:

$$R = \frac{I_{ph}}{P_{inc}} = \frac{I_{light} - I_{dark}}{P_{inc}},$$

$$P = \frac{I_{light} - I_{dark}}{I_{dark}}.$$

The derived R and P values were plotted against the different gate voltages. These values were found to generally increase with increasing the gate voltage because a strong electric field led to an efficient charge separation and transfer.[54, 55] The maximum (R, P) values for PDAP-Fu, PDAP-Th, and PDAP-Se are (143.88 A W^{-1}, 8.79), (121.25 A W^{-1}, 33.36), and (560.08 A W^{-1}, 1008.12), respectively. Besides, the η, which indicates the ratio of the number of photogenerated carriers enhancing

the drain current to that of the photons irradiated onto the channel area, was calculated under different gate voltages according to

$$\eta = \frac{(I_{light} - I_{dark})hc}{eP_{inc}A\lambda_{peak}},$$

where h is the Planck constant, c is the speed of light, e is the fundamental unit of charge, A is the area of the transistor channel, and λ_{peak} is the peak wavelength of the incident light. Since η is proportional to R, the η values showed the same order as observed in the R values above (PDAP-Th < PDAP-Fu < PDAP-Se). The higher R and η values of PDAP-Se might be related to the superior hole mobility of this film.[5, 56] The D^* is another key parameter to evaluate the photoresponse properties of the OPTs. The noise-equivalent power (NEP), which is the minimum photosensitive power distinguished from noise, is considered to calculate the D^* value, which can be obtained according to

$$D^* = \frac{\sqrt{A}}{NEP},$$

$$\mathrm{NEP} = \frac{\sqrt{\overline{I_n^2}}}{R},$$

where A is the active area and $\overline{I_n^2}$ is the measured noise current. If the shot noise from the dark current is the major factor limiting D^*, then D^* can be simplified as

$$D^* = \frac{R}{\sqrt{\left(2e \cdot \frac{I_{dark}}{A}\right)}}.$$

Both η and R were modulated by the gate voltage, revealing that a more negative gate voltage mostly results in higher η and R values, as seen from **Figure 3.9**c,d. Besides, as the *EQE* values increased, the photoinduced current also increased, resulting in a higher R, which is proportional to D^*. The maximum *EQE* values of PDAP-Fu, PDAP-Th, and PDAP-Se (*i.e.*, 1.68×10^4 %, 1.42×10^4 %, and 6.56×10^4 %) were observed at gate voltages of −77, −56, and −100 V, respectively.

Conversely, as shown in **Figure 3.9**e, different sharp trends in the maximum *D** values were observed at −37 V for PDAP-Fu, −4 V for PDAP-Th, and 34 V for PDAP-Se. These results can be explained by the fact that a lower-noise current leads to a higher OPT detectivity at different gate voltages in comparison with the maximum *EQE* values.[57] This also demonstrates that the high detectivity value is related to the operation conditions for low-noise OPT devices. We note that the overestimated D* values might be obtained because we assumed that the total noise is equal to the shot noise, ignoring the thermal and flicker noise, which is commonly found in the literatures. The maximum D* value for PDAP-Se was as high as 1.8×10^{12} Jones, followed by 3.84×10^{11} and 3.23×10^{11} Jones for PDAP-Th and PDAP-Fu, respectively. The spectra of the EQE values in various wavelength (**Figure 3.10**) and plots of linear dynamic range (**Figure 3.11**) and single normalized cycle (**Figure 3.12**) also demonstrated the excellent performance of PDAP-Se compared to that of PDAP-Fu and PDAP-Th. These results are remarkable for OPT-photosensing experiments conducted under NIR light illumination.

Table 3.5 summarizes all the relevant values. These results demonstrate that NIR light facilitates the photocurrent generation in DAP-based OPTs, thus leading to high values of η and *D**. It should be highlighted that DAP-based copolymers exhibited a remarkable performance with *D** values higher than those of previously reported photodetectors based on DAP-containing polymers.[33] Moreover, this also shows the strong benefits of the high detectivity of the NIR range of light over a wavelength of 1000 nm. Furthermore, to observe photochemical stability of DAP-based copolymers, Fourier transform infrared (FT-IR) spectra was acquired before and after irradiation with 1060 nm light for 24 hours (**Figure 3.13**). In addition, the absorbance was measured every 6 hours by UV−Vis−NIR spectroscopy during the irradiation (Figure SXX). FT-IR spectra showed that the DAP-based copolymers are not chemically decomposed in the 1060 nm light, though the UV−Vis−NIR spectra is interpretated as the deteriorated molecular packing. As a result, DAP-based

copolymers also exhibit good photochemical stability under 1060 nm light illumination. Therefore, it is suggested that DAP-based materials have high potential for use in organic optoelectronics using NIR light as the incoming signal.

3.4. Conclusion

In conclusion, we synthesized a new series of ultralow-bandgap DAP-based D−A-type copolymers with chalcogenophene counterparts (Fu, Th, and Se). The resulting copolymers (PDAP-Fu, PDAP-Th, and PDAP-Se) had ultralow E_g^{opt} values of ~1.0 eV, covering the whole Vis–NIR range. In addition to the slightly more pronounced red shift in λ_{max} with increasing the heteroatomic size of the chalcogenophene counterparts, we also observed that both the HOMO and LUMO levels of the copolymers gradually deepened in energy from PDAP-Se to PDAP-Fu to PDAP-Th. The copolymers incorporated into the OFET devices show unipolar *p*-channel operation, and the PDAP-Se film shows the best hole mobility (up to 4.79×10^{-1} cm^2 V^{-1} s^{-1}), as a result of the formation of a 3D charge-conduction channel with high crystallinity, which was evidenced by morphological studies. Furthermore, the copolymers exhibited excellent NIR photoresponsive properties; particularly, the PDAP-Se-based OPT had the highest maximum values of R, P, η, and D^* of 560.08 A W^{-1}, 1008.12, 6.56×10^4 %, and 1.80×10^{12} Jones, respectively, under 1060 nm light illumination. These results show that ultralow-bandgap DAP-based copolymers are highly promising for use in NIR sensors because of their high responsivity, easy fabrication, low cost, and mechanical flexibility.

3.5. References

(1) Huang, J.; Lee, J.; Vollbrecht, J.; Brus, V. V.; Dixon, A. L.; Cao, D. X.; Zhu, Z.; Du, Z.; Wang, H.; Cho, K.; Bazan, G. C.; Nguyen, T.-Q. A High-Performance Solution-Processed Organic Photodetector for Near-Infrared Sensing. *Adv. Mater.* **2020**, *32,* 1906027.

(2) Jung, J. H.; Yoon, M. J.; Lim, J. W.; Lee, Y. H.; Lee, K. E.; Kim, D. H.; Oh, J. H. High-Performance UV–Vis–NIR Phototransistors Based on Single-Crystalline Organic Semiconductor–Gold Hybrid Nanomaterials. *Adv. Func. Mater.* **2017**, *27,* 1604528.

(3) Liu, G.; Li, T.; Zhan, X.; Wu, H.; Cao, Y. High-Sensitivity Visible–Near Infrared Organic Photodetectors Based on Non-Fullerene Acceptors. *ACS Appl. Mater. Interfaces* **2020**, *12,* 17769–17775.

(4) Peng, Y.; Lv, W.; Yao, B.; Fan, G.; Chen, D.; Gao, P.; Zhou, M.; Wang, Y. High performance near infrared photosensitive organic field-effect transistors realized by an organic hybrid planar-bulk heterojunction. *Org. Electron.* **2013**, *14,* 1045–1051.

(5) Xu, H.; Li, J.; Leung, B. H. K.; Poon, C. C. Y.; Ong, B. S.; Zhang, Y.; Zhao, N. A high-sensitivity near-infrared phototransistor based on an organic bulk heterojunction. *Nanoscale* **2013**, *5,* 11850–11855.

(6) Yen, H.-J.; Liou, G.-S. Enhanced near-infrared electrochromism in triphenylamine-based aramids bearing phenothiazine redox centers. *J. Mater. Chem.* **2010**, *20,* 9886–9894.

(7) Li, H.; Sun, S.; Salim, T.; Bomma, S.; Grimsdale, A. C.; Lam, Y. M. Conjugated polymers based on dicarboxylic imide-substituted isothianaphthene and their applications in solar cells. *J. Polym. Sci. A Polym. Chem.* **2012**, *50,* 250–260.

(8) Meng, H.; Wudl, F. A Robust Low Band Gap Processable n-Type Conducting Polymer Based on Poly(isothianaphthene). *Macromolecules* **2001**, *34,* 1810–1816.

(9) Kastner, J.; Kuzmany, H.; Vegh, D.; Landl, M.; Cuff, L.; Kertesz, M. Raman Spectra of Poly(2,3-R,R-thieno[3,4-b]pyrazine). A New Low-Band-Gap Polymer. *Macromolecules* **1995**, *28,* 2922–2929.

(10) Mikie, T.; Osaka, I. Small-bandgap quinoid-based π-conjugated polymers. *J. Mater. Chem. C* **2020**, *8,* 14262–14288.

(11) Zheng, J.; Zhou, H.; Zou, Y.; Wang, R.; Lyu, Y.; Jiang, S. P.; Wang, S. Efficiency and stability of narrow-gap semiconductor-based photoelectrodes. *Energy Environ. Sci.* **2019**, *12,* 2345–2374.

(12) Kang, S.-H.; Jeong, A.; Lee, H. R.; Oh, J. H.; Yang, C. Bioderived and Eco-Friendly Solvent-Processed High-Mobility Ambipolar Plastic Transistors through Controlled Irregularity of the Polymer Backbone. *Chem. Mater.* **2019**, *31,* 3831–3839.

(13) Kim, Y.-A.; Jeon, Y.-J.; Kang, M.; Jang, S.-Y.; Kim, I.-B.; Lim, D.-H.; Heo, Y.-J.; Kim, D.-Y. Structure-property relationship of D-A type copolymers based on thienylenevinylene for organic electronics. *Org. Electron.* **2017**, *46,* 77–87.

(14) Patil, A. V.; Lee, W.-H.; Kim, K.; Park, H.; Kang, I. N.; Lee, S.-H. Synthesis and photovoltaic properties of narrow band gap copolymers of dithieno[3,2-b:2′,3′-d]thiophene and diketopyrrolopyrrole. *Polym. Chem.* **2011**, *2,* 2907–2916.

(15) Pei, J.; Wen, S.; Zhou, Y.; Dong, Q.; Liu, Z.; Zhang, J.; Tian, W. A low band gap donor–acceptor copolymer containing fluorene and benzothiadiazole units: synthesis and photovoltaic properties. *New J. Chem.* **2011**, *35,* 385–393.

(16) Raheem, A. A.; Kamaraj, S.; Sannasi, V.; Praveen, C. New D–π-A push–pull chromophores as low band gap molecular semiconductors for organic small molecule solar cell applications. *Org. Chem. Front.* **2018**, *5,* 777–787.

(17) Zhang, Z.-G.; Yang, Y.; Yao, J.; Xue, L.; Chen, S.; Li, X.; Morrison, W.; Yang, C.; Li, Y. Constructing a Strongly Absorbing Low-Bandgap Polymer Acceptor for High-Performance All-Polymer Solar Cells. *Angew. Chem. Int. Ed.* **2017**, *56,* 13503–13507.

(18) Keyworth, C. W.; Chan, K. L.; Labram, J. G.; Anthopoulos, T. D.; Watkins, S. E.; McKiernan, M.; White, A. J. P.; Holmes, A. B.; Williams, C. K. The tuning of the energy levels of dibenzosilole copolymers and applications in organic electronics. *J. Mater. Chem.* **2011**, *21,* 11800–11814.

(19) Popere, B. C.; Della Pelle, A. M.; Poe, A.; Balaji, G.; Thayumanavan, S. Predictably tuning the frontier molecular orbital energy levels of panchromatic low band gap BODIPY-based conjugated polymers. *Chem. Sci.* **2012**, *3,* 3093–3102.

(20) Geng, Y.; Huang, J.; Tajima, K.; Zeng, Q.; Zhou, E. A low band gap n-type polymer based on dithienosilole and naphthalene diimide for all-polymer solar cells application. *Polymer* **2015**, *63,* 164–169.

(21) Guo, X.; Kim, F. S.; Seger, M. J.; Jenekhe, S. A.; Watson, M. D. Naphthalene Diimide-Based Polymer Semiconductors: Synthesis, Structure–Property Correlations, and n-Channel and Ambipolar Field-Effect Transistors. *Chem. Mater.* **2012**, *24,* 1434–1442.

(22) Jiang, T.; Xue, Z.; Ford, M.; Shaw, J.; Cao, X.; Tao, Y.; Hu, Y.; Huang, W. An ultra-low bandgap diketopyrrolopyrrole (DPP)-based polymer with balanced ambipolar charge transport for organic field-effect transistors. *RSC Adv.* **2016**, *6,* 78720–78726.

(23) Shi, S.; Chen, P.; Chen, Y.; Feng, K.; Liu, B.; Chen, J.; Liao, Q.; Tu, B.; Luo, J.; Su, M.; Guo, H.; Kim, M.-G.; Facchetti, A.; Guo, X. A Narrow-Bandgap n-Type Polymer Semiconductor Enabling Efficient All-Polymer Solar Cells. *Adv. Mater.* **2019**, *31,* 1905161.

(24) Würthner, F.; Stolte, M. Naphthalene and perylene diimides for organic transistors. *Chem. Commun.* **2011**, *47,* 5109–5115.

(25) Yi, Z.; Wang, S.; Liu, Y. Design of High-Mobility Diketopyrrolopyrrole-Based π-Conjugated Copolymers for Organic Thin-Film Transistors. *Adv. Mater.* **2015**, *27,* 3589–3606.

(26) A, V.; Liu, S.-W.; Wong, K.-T. Organic polymeric and small molecular electron acceptors for organic solar cells. *Mater. Sci. Eng. R Rep.* **2018**, *124,* 1–57.

(27) Shi, H.; Fu, W.; Shi, M.; Ling, J.; Chen, H. A solution-processable bipolar diketopyrrolopyrrole molecule used as both electron donor and acceptor for efficient organic solar cells. *J. Mater. Chem. A* **2015**, *3,* 1902–1905.

(28) Sonar, P.; Ng, G.-M.; Lin, T. T.; Dodabalapur, A.; Chen, Z.-K. Solution processable low bandgap diketopyrrolopyrrole (DPP) based derivatives: novel acceptors for organic solar cells. *J. Mater. Chem.* **2010**, *20,* 3626–3636.

(29) Khelifi, W.; Awada, H.; Brymora, K.; Blanc, S.; Hirsch, L.; Castet, F.; Bousquet, A.; Lartigau-Dagron, C. Halochromic Switch from the 1st to 2nd Near-Infrared Window of Diazapentalene–Dithienosilole Copolymers. *Macromolecules* **2019**, *52,* 4820–4827.

(30) Qian, G.; Qi, J.; Wang, Z. Y. Synthesis and study of low-bandgap polymers containing the diazapentalene and diketopyrrolopyrrole chromophores for potential use in solar cells and near-infrared photodetectors. *J. Mater. Chem.* **2012**, *22,* 12867–12873.

(31) Yurovskaya, M. A.; Karchava, A. V. Stereoselective reduction of endocyclic carbon–nitrogen double bond: application to the synthesis of biomolecules. *Tetrahedron: Asymmetry* **1998**, *9,* 3331–3352.

(32) Ni, Z.; Wang, H.; Zhao, Q.; Zhang, J.; Wei, Z.; Dong, H.; Hu, W. Ambipolar Conjugated Polymers with Ultrahigh Balanced Hole and Electron Mobility for Printed Organic Complementary Logic via a Two-Step C–H Activation Strategy. *Adv. Mater.* **2019**, *31,* 1806010.

(33) Qian, G.; Qi, J.; Davey, J. A.; Wright, J. S.; Wang, Z. Y. Family of Diazapentalene Chromophores and Narrow-Band-Gap Polymers: Synthesis, Halochromism, Halofluorism, and Visible–Near Infrared Photodetectivity. *Chem. Mater.* **2012**, *24,* 2364–2372.

(34) Woo, C. H.; Beaujuge, P. M.; Holcombe, T. W.; Lee, O. P.; Fréchet, J. M. J. Incorporation of Furan into Low Band-Gap Polymers for Efficient Solar Cells. *J. Am. Chem. Soc.* **2010**, *132,* 15547–15549.

(35) Bridges, C. R.; Ford, M. J.; Thomas, E. M.; Gomez, C.; Bazan, G. C.; Segalman, R. A. Effects of Side Chain Branch Point on Self Assembly, Structure, and Electronic Properties of High Mobility Semiconducting Polymers. *Macromolecules* **2018**, *51,* 8597–8604.

(36) Raj, M. R.; Kim, Y.; Park, C. E.; An, T. K.; Park, T. Effect of the length of a symmetric branched side chain on charge transport in thienoisoindigo-based polymer field-effect transistors. *Org. Electron.* **2019**, *65,* 251–258.

(37) Ashraf, R. S.; Meager, I.; Nikolka, M.; Kirkus, M.; Planells, M.; Schroeder, B. C.; Holliday, S.; Hurhangee, M.; Nielsen, C. B.; Sirringhaus, H.; McCulloch, I. Chalcogenophene Comonomer Comparison in Small Band Gap Diketopyrrolopyrrole-Based Conjugated Polymers for High-Performing Field-Effect Transistors and Organic Solar Cells. *J. Am. Chem. Soc.* **2015**, *137,* 1314–1321.

(38) Jeffries-El, M.; Kobilka, B. M.; Hale, B. J. Optimizing the Performance of Conjugated Polymers in Organic Photovoltaic Cells by Traversing Group 16. *Macromolecules* **2014**, *47,* 7253–7271.

(39) Lee, S. M.; Lee, H. R.; Dutta, G. K.; Lee, J.; Oh, J. H.; Yang, C. Furan-flanked diketopyrrolopyrrole-based chalcogenophene copolymers with siloxane hybrid side chains for organic field-effect transistors. *Polym. Chem.* **2019**, *10,* 2854–2862.

(40) Jung, E. H.; Bae, S.; Yoo, T. W.; Jo, W. H. The effect of different chalcogenophenes in isoindigo-based conjugated copolymers on photovoltaic properties. *Polym. Chem.* **2014**, *5,* 6545–6550.

(41) Kaur, M.; Seul Yang, D.; Shin, J.; Wan Lee, T.; Choi, K.; Ju Cho, M.; Hoon Choi, D. A novel tellurophene-containing conjugated polymer with a dithiophenyl diketopyrrolopyrrole unit for use in organic thin film transistors. *Chem. Commun.* **2013**, *49,* 5495–5497.

(42) Planells, M.; Schroeder, B. C.; McCulloch, I. Effect of Chalcogen Atom Substitution on the Optoelectronic Properties in Cyclopentadithiophene Polymers. *Macromolecules* **2014**, *47,* 5889–5894.

(43) Kim, J.; Chae, S.; Yi, A.; Hong, S.; Kim, H. J.; Suh, H. Characterization of push-pull type of conjugated polymers containing 8H-thieno[2,3-b]indole for organic photovoltaics. *Synth. Met.* **2018**, *245,* 267–275.

(44) Wang, M.; Ford, M. J.; Lill, A. T.; Phan, H.; Nguyen, T.-Q.; Bazan, G. C. Hole Mobility and Electron Injection Properties of D-A Conjugated Copolymers with Fluorinated Phenylene Acceptor Units. *Adv. Mater.* **2017**, *29,* 1603830.

(45) Kang, S.-H.; Lee, H. R.; Dutta, G. K.; Lee, J.; Oh, J. H.; Yang, C. A Role of Side-Chain Regiochemistry of Thienylene–Vinylene–Thienylene (TVT) in the Transistor Performance of Isomeric Polymers. *Macromolecules* **2017**, *50,* 884–890.

(46) Patterson, A. L. The Scherrer Formula for X-Ray Particle Size Determination. *Phys. Rev.* **1939**, *56,* 978–982.

(47) Lee, G.-Y.; Han, A. R.; Kim, T.; Lee, H. R.; Oh, J. H.; Park, T. Requirements for Forming Efficient 3-D Charge Transport Pathway in Diketopyrrolopyrrole-Based Copolymers: Film Morphology vs Molecular Packing. *ACS Appl. Mater. Interfaces* **2016**, *8,* 12307–12315.

(48) Lee, J.; Han, A. R.; Yu, H.; Shin, T. J.; Yang, C.; Oh, J. H. Boosting the Ambipolar Performance of Solution-Processable Polymer Semiconductors via Hybrid Side-Chain Engineering. *J. Am. Chem. Soc.* **2013**, *135,* 9540–9547.

(49) Ge, G.-Y.; Xiong, W.; Liu, K.-K.; Ryu, H. S.; Wan, S.-S.; Liu, B.; Mahmood, A.; Bai, H.-R.; Wang, J.-F.; Wang, Z.; Woo, H. Y.; Sun, Y.; Wang, J.-L. Synergistic effect of the selenophene-containing central core and the regioisomeric monochlorinated terminals on the molecular packing, crystallinity, film morphology, and photovoltaic performance of selenophene-based nonfullerene acceptors. *J. Mater. Chem. C* **2021**, *9,* 1923–1935.

(50) Yang, J.; Zhao, Z.; Wang, S.; Guo, Y.; Liu, Y. Insight into High-Performance Conjugated Polymers for Organic Field-Effect Transistors. *Chem* **2018**, *4,* 2748–2785.

(51) Bittle, E. G.; Basham, J. I.; Jackson, T. N.; Jurchescu, O. D.; Gundlach, D. J. Mobility overestimation due to gated contacts in organic field-effect transistors. *Nat. Commun.* **2016**, *7,* 10908.

(52) Choi, H. H.; Cho, K.; Frisbie, C. D.; Sirringhaus, H.; Podzorov, V. Critical assessment of charge mobility extraction in FETs. *Nat. Mater.* **2018**, *17,* 2–7.

(53) McCulloch, I.; Salleo, A.; Chabinyc, M. Avoid the kinks when measuring mobility. *Science* **2016**, *352,* 1521.

(54) Fang, Y.; Armin, A.; Meredith, P.; Huang, J. Accurate characterization of next-generation thin-film photodetectors. *Nat. Photon.* **2019**, *13,* 1–4.

(55) Saran, R.; Curry, R. J. Lead sulphide nanocrystal photodetector technologies. *Nat. Photon.* **2016**, *10,* 81–92.

(56) Chow, P. C. Y.; Matsuhisa, N.; Zalar, P.; Koizumi, M.; Yokota, T.; Someya, T. Dual-gate organic phototransistor with high-gain and linear photoresponse. *Nat. Commun.* **2018**, *9,* 4546.

(57) Ji, D.; Li, T.; Liu, J.; Amirjalayer, S.; Zhong, M.; Zhang, Z.-Y.; Huang, X.; Wei, Z.; Dong, H.; Hu, W.; Fuchs, H. Band-like transport in small-molecule thin films toward high mobility and ultrahigh detectivity phototransistor arrays. *Nat. Commun.* **2019**, *10,* 12.

3.6. Figures and Tables

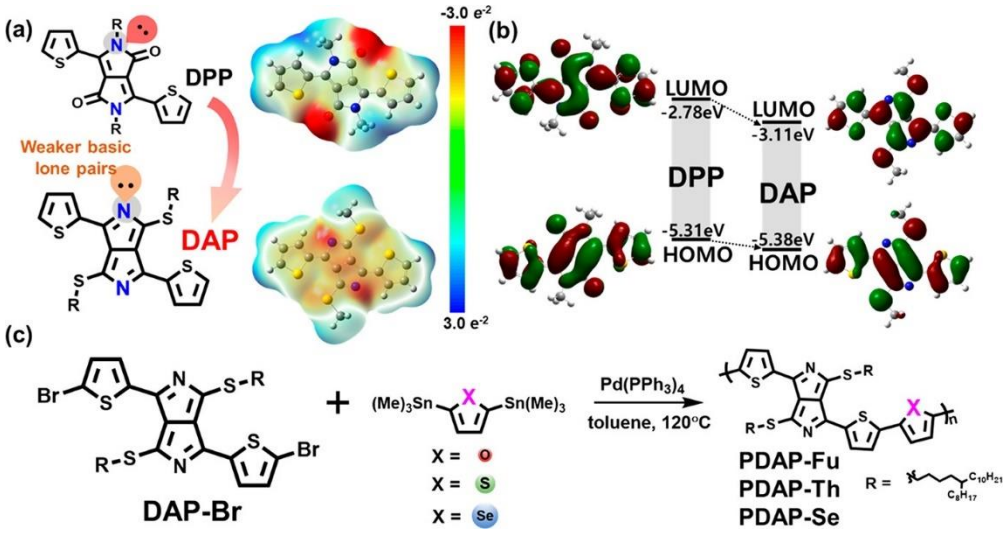

Figure 3.1. (a) Distribution of frontier molecular orbitals and their energy levels. (b) Electrostatic surface potential for DPP and DAP. (c) Synthetic routes and chemical structures of DAP-based copolymers.

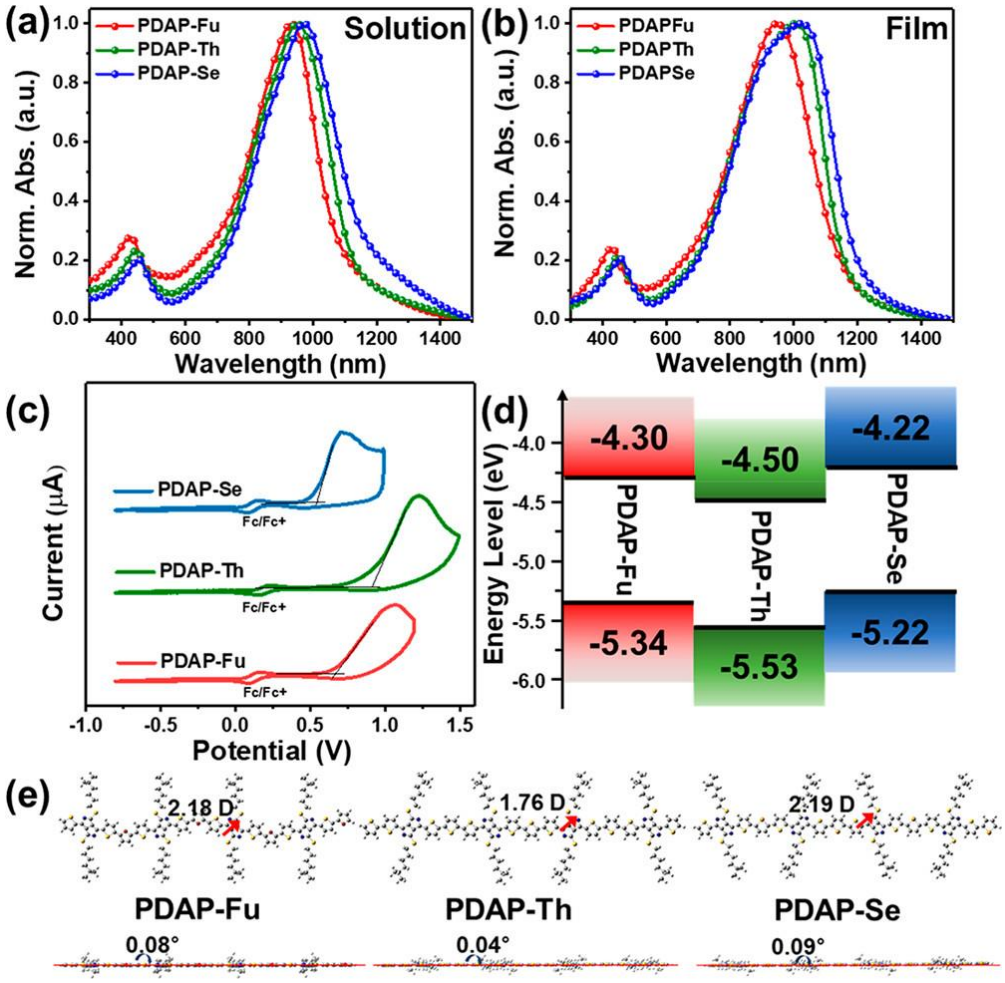

Figure 3.2. Normalized UV–vis–NIR absorption spectra (a) in chloroform solution and (b) as thin films. (c) Cyclic voltammograms with the internal standard of ferrocene/ferrocenium. (d) Energy level diagram of DAP-based copolymers. (e) Optimized front geometries with illustration of the net dipole moment (top) and side view for the tetramer models (bottom) from the DFT calculation results.

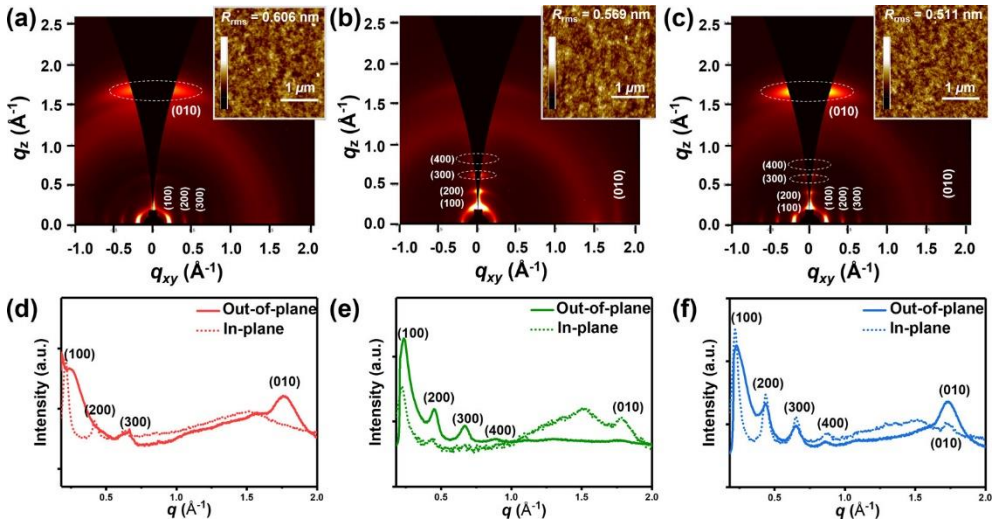

Figure 3.3. Two-dimensional GIXD images and 3 × 3 μm scaled AFM height images (upper-right) of (a) PDAP–Fu, (b) PDAP–Th, and (c) PDAP–Se thin films thermally annealed at 150 °C. Rrms is the roughness of the films. Scale bar = 1 μm. Corresponding GIXD diffractogram profiles along the out-of-plane and in-plane directions of (d) PDAP–Fu, (e) PDAP–Th, and (f) PDAP–Se polymer films. Polymer films were prepared by the spin-coating method on OTS-modified SiO2/Si substrates.

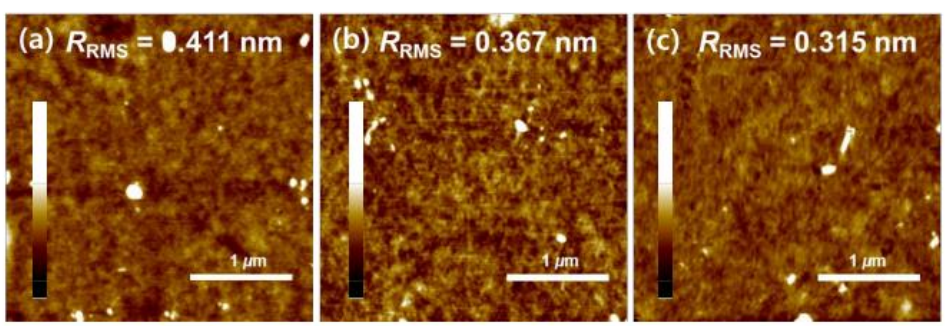

Figure 3.4. AFM height images (3 × 3 μm) of before (bottom) thermal treatment of (a)PDAP-Fu, (b) PDAP-Th, and (c) PDAP-Se films. The polymer films were formed by spin-coating on OTS-modified SiO2/Si substrates. RRMS is rms roughness of film. Scale bar = 1 μm.

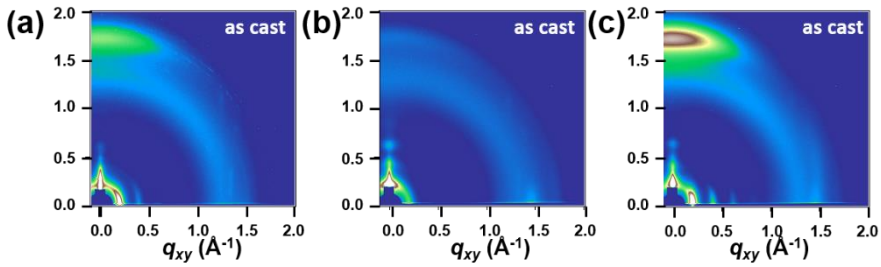

Figure 3.5. 2D-GIXD images for as-cast films of (a) PDAP-Fu (b) PDAP-Th, and (c) PDAP-Se. The films are fabricated by the spin-coating method on OTS modified SiO_2/Si substrates.

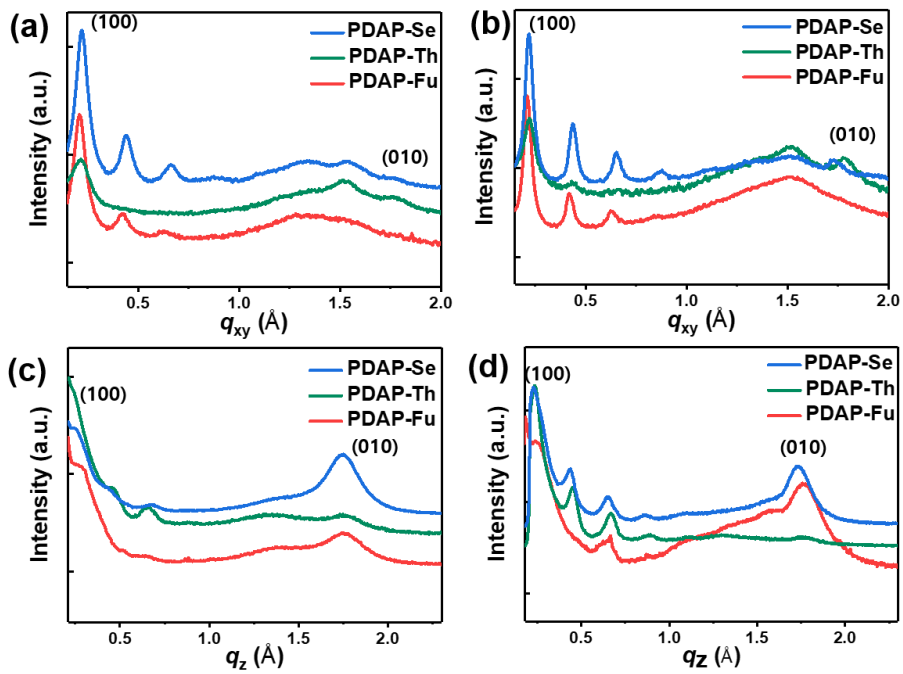

Figure 3.6. X-ray diffractogram profiles of (a) in-plane and (b) out-of-plane of as-cast thin films of DAP-based copolymers.

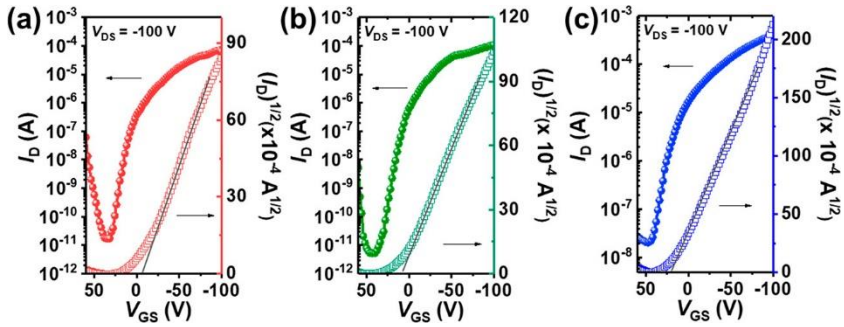

Figure 3.7. Transfer characteristics of (a) PDAP−Fu, (b) PDAP−Th, and (c) PDAP−Se.

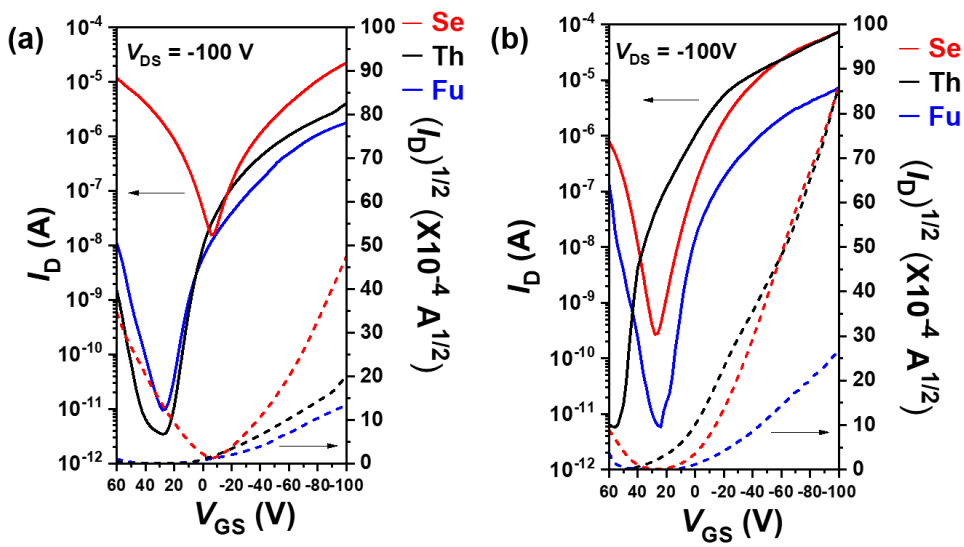

Figure 3.8. Transfer characteristics of PDAP-Fu, PDAP-Th, and PDAP-Se in (a) as cast films and (b) annealed films at 100 °C. The polymer films were formed by spin-coating method on OTS-modified SiO_2/Si substrates.

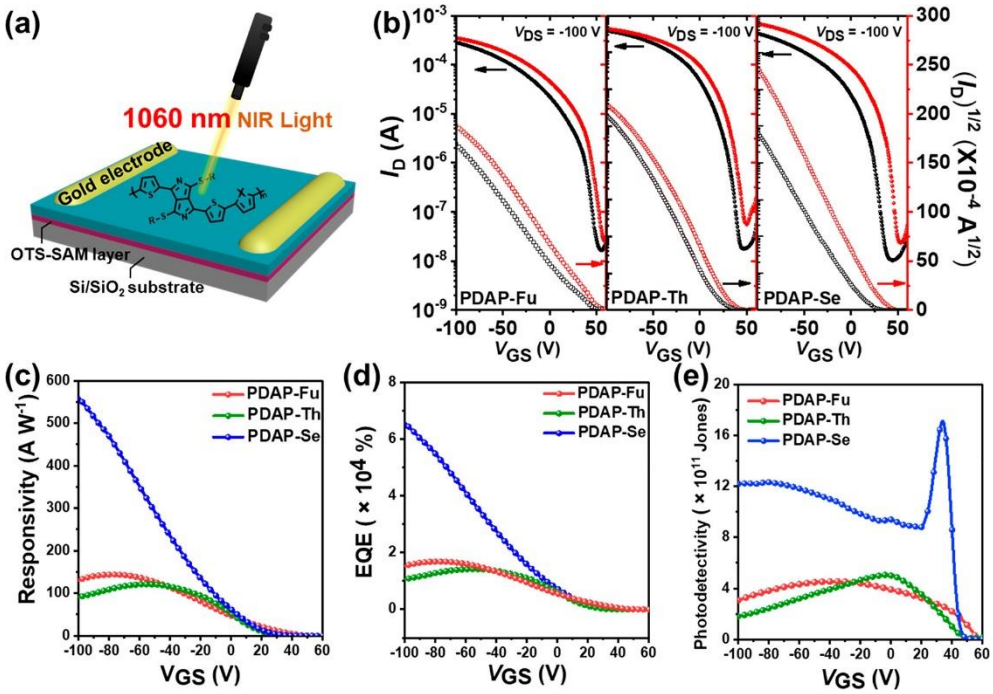

Figure 3.9. (a) Schematic illustration of BGTC phototransistor devices. (b) Transfer curves in the dark (black line) and under 1060 nm light irradiation (red line) of PDAP−Fu, PDAP−Th, and PDAP−Se. (c) Photoresponsivity (R), (d) external quantum efficiency (EQE), and (e) photodetectivity (D*) of DAP-based copolymers under 1060 nm light illumination (light intensity = 1 mW cm^{-2})

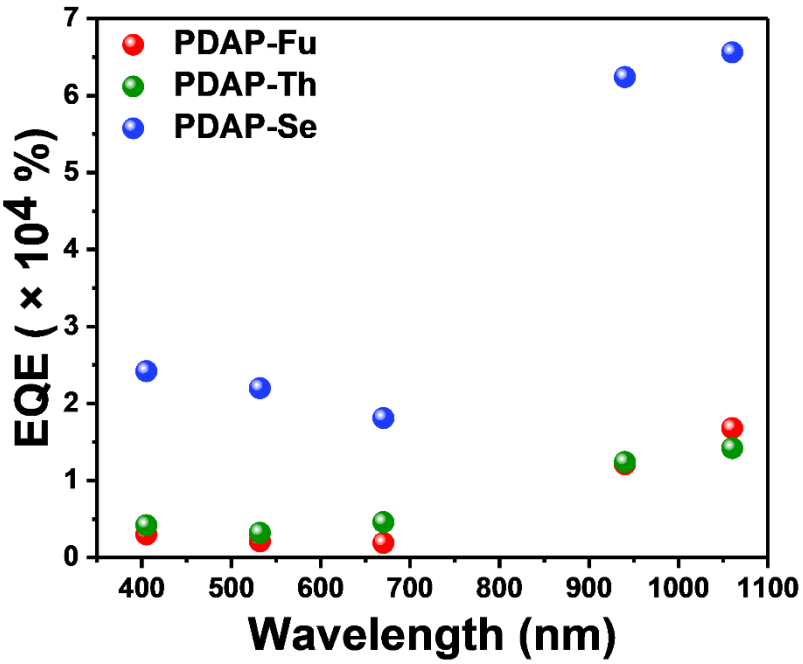

Figure 3.10. EQE spectra of the DAP-based photodetectors at −100V in various wavelengths (405 nm, 532 nm, 670 nm, 940 nm, and 1060 nm).

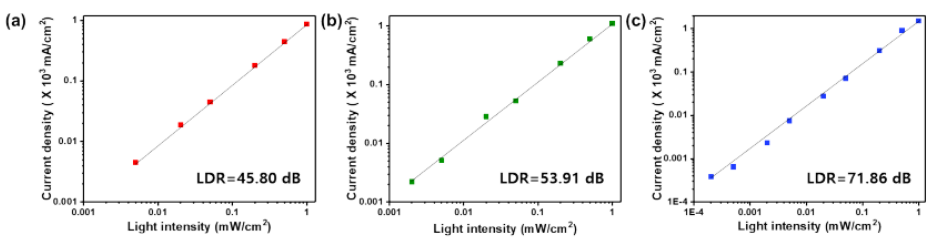

Figure 3.11. The linear dynamic range (LDR) for the OPTs measured at −100V with 1060 nm, (a) PDAP-Fu, (b) PDAP-Th, and (c) PDAP-Se.

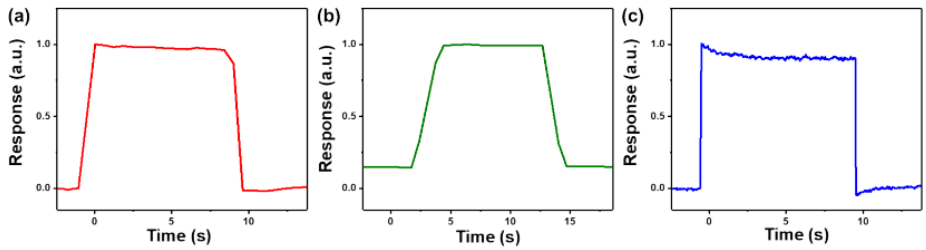

Figure 3.12. Single normalized cycle of the phototransistor for estimating both rise time and fall time. (a) PDAP-Fu, (b) PDAP-Th, and (c) PDAP-Se.

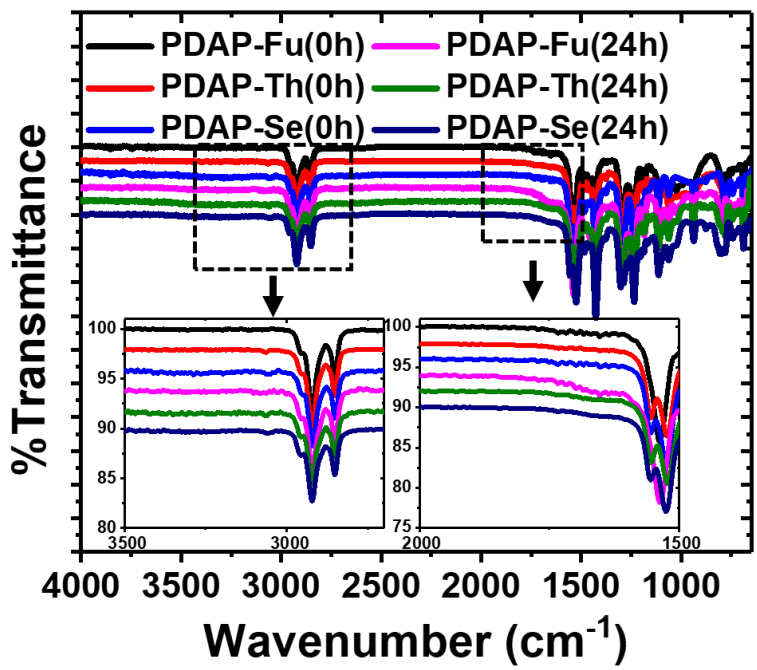

Figure 3.13. FT-IR spectra of DAP-based copolymers under 1060 nm light and ambient condition.

	λ_{sol}^{max} [nm]	λ_{film}^{max} [nm]	λ_{onset} [nm]	E_g^{opt} [eV]	E_{HOMO} [eV]	E_{LUMO} [eV]	M_n [kDa]	PDI
PDAP-Fu	933	948	1188	1.04	-5.34	-4.30	64.1	1.75
PDAP-Th	952	1005	1202	1.03	-5.53	-4.50	67.1	1.70
PDAP-Se	973	1032	1245	1.00	-5.22	-4.22	60.8	1.85

[a] Determined from the onset of the UV−vis−NIR absorption plots of the copolymer films. [b] Determined from the onset of the Tauc plots of the copolymers.

Table 3.1. Photophysical and Electrochemical Properties of DAP-Based Copolymers.

(a)

Polymer film	T_a [°C]	Lamellar stacking [b]			π-π stacking [c]		
		q_z [Å^{-1}]	d_z [Å]	L_c [Å]	q_z [Å^{-1}]	d_z [Å]	L_c [Å]
PDAP-Fu	N/A	0.252	25.13	76.07	1.737	3.62	56.57
	150	0.238	26.34	94.75	1.762	3.57	69.69
PDAP-Th	N/A	0.442	14.22	97.96	-	-	-
	150	0.450	13.96	323.98	-	-	-
PDAP-Se	N/A	0.352	17.85	44.34	1.743	3.60	89.07
	150	0.433	14.49	363.73	1.732	3.63	121.75

(b)

Polymer film	T_a [°C]	Lamellar stacking [b]			π-π stacking [c]		
		q_{xy} [Å^{-1}]	d_{xy} [Å]	L_c [Å]	q_{xy} [Å^{-1}]	d_{xy} [Å]	L_c [Å]
PDAP-Fu	N/A	0.211	29.81	309.36	-	-	-
	150	0.212	29.68	495.13	-	-	-
PDAP-Th	N/A	0.213	29.42	200.31	1.744	3.60	53.73
	150	0.221	28.38	343.94	1.781	3.53	137.83
PDAP-Se	N/A	0.222	28.33	330.85	1.714	3.66	18.72
	150	0.220	28.57	499.98	1.730	3.63	230.22

Table 3.2. Crystallographic parameters of as-cast films and films annealed at 150 °C.

Polymer	Annealed Condition	μ_{max}[a] [$cm^2V^{-1}s^{-1}$]	μ_{avg}[b] [$cm^2V^{-1}s^{-1}$]	μ_{eff} [$cm^2V^{-1}s^{-1}$]	r [%]	I_{on}/I_{off}	V_T [V]
PDAP-Fu	As cast	4.00×10^{-3}	1.32×10^{-3} (± 0.001)[c]	1.59×10^{-3}	40	$> 10^5$	-14.8
	Annealed at 100 °C	2.50×10^{-2}	1.47×10^{-2} (± 0.005)	6.67×10^{-3}	27	$> 10^6$	-9.3
	Annealed at 150 °C	1.57×10^{-1}	1.13×10^{-1} (± 0.032)	6.10×10^{-2}	39	$> 10^6$	-6.2
PDAP-Th	As cast	1.97×10^{-2}	1.02×10^{-2} (± 0.004)	3.69×10^{-3}	19	$> 10^6$	-4.2
	Annealed at 100 °C	1.16×10^{-1}	7.28×10^{-2} (± 0.021)	3.85×10^{-2}	33	$> 10^6$	1.5
	Annealed at 150 °C	2.08×10^{-1}	1.47×10^{-1} (± 0.028)	9.11×10^{-2}	44	$> 10^7$	7.9
PDAP-Se	As cast	5.60×10^{-2}	4.03×10^{-2} (± 0.007)	2.05×10^{-2}	37	$> 10^3$	-7.1
	Annealed at 100 °C	1.73×10^{-1}	1.14×10^{-1} (± 0.037)	7.01×10^{-2}	41	$> 10^6$	-3.7
	Annealed at 150 °C	4.76×10^{-1}	3.79×10^{-1} (± 0.099)	1.07×10^{-1}	43	$> 10^4$	17.8

Table 3.3. Summary of hole mobility, reliability factors and threshold voltage of PDAP-based OFETs with different annealing temperature. [a]The maximum mobility of the FET devices (L=50 μm and W = 1000 μm). [b]The average mobility of 10 FET devices (L=50 μm and W = 1000 μm). [c]The standard deviation.

Polymer	Annealed Condition	μ_{max}[a] [$cm^2V^{-1}s^{-1}$]	μ_{avg}[b] [$cm^2V^{-1}s^{-1}$]	μ_{eff} [$cm^2V^{-1}s^{-1}$]	r [%]	I_{on}/I_{off}	V_T [V]
PDAP-Fu	150 °C	1.57×10^{-1}	1.13×10^{-1} (± 0.032)[c]	6.10×10^{-2}	39	$>10^6$	-6.2
PDAP-Th	150 °C	2.08×10^{-1}	1.48×10^{-1} (± 0.028)	9.11×10^{-2}	44	$>10^7$	7.9
PDAP-Se	150 °C	4.76×10^{-1}	3.79×10^{-1} (± 0.099)	2.05×10^{-1}	43	$>10^4$	17.8

[a]The maximum mobility of the FET devices (L = 50 μm and W = 1000 μm). [b] The average mobility of 10 FET devices (L = 50 μm and W = 1000 μm). [c] The standard deviation.

Table 3.4. Summary of hole mobility, reliability factors, and threshold voltage of PDAP-based OFETs.

Polymer	R^a [$A W^{-1}$]	P^a	EQE^a [%]	D^*[a] [Jones]
PDAP-Fu	143.88	8.79	1.68×10^4	3.23×10^{11}
PDAP-Th	121.25	33.36	1.42×10^4	3.84×10^{11}
PDAP-Se	560.08	1008.12	6.56×10^4	1.80×10^{12}

[a] Maximum values obtained in the gate voltage sweep (from 60 to −100 V) under monochromic light illumination (λ = 1060 nm, 1 mW cm^{-2}).

Table 3.5. Optoelectronic characteristics of phototransistors based on PDAP−Fu, PDAP−Th, and PDAP−Se films.

Chapter 4

Studies on Side Chain Engineering in chirality and stacking of PDI-based monomers

4. 1. Introduction

The development of organic semiconducting materials has seen significant advancements in recent years, driven by the increasing demand for renewable and sustainable energy sources. Among these, perylene diimides (PDIs) have emerged as a promising class of materials due to their excellent electronic and optical properties. PDIs possess high electron affinity, good thermal stability, and the ability to form ordered structures. These characteristics make PDIs an attractive option for use in organic photovoltaic (OPV) devices, as they can enhance the efficiency of charge transport and reduce energy loss.

Despite their many advantages, the performance of PDIs in OPV devices is often limited by their low solubility and tendency to aggregate, which can reduce the efficiency of charge transport. To address these issues, one approach is to modify the structure of PDIs through side chain engineering. This involves introducing different functional groups onto the core PDI molecule to tune its properties, such as solubility, packing, and electronic structure. Side chain engineering has been shown to improve the solubility and processability of PDIs and enable the formation of well-ordered structures, which can enhance the efficiency of charge transport in OPV devices.

Furthermore, chirality has been identified as a critical parameter that influences the optoelectronic properties of PDIs. Chiral PDIs exhibit enhanced circular dichroism (CD) signals and improved performance in OPV devices, making them an attractive option for use in such devices. The use of chiral PDIs in OPV devices can also enable the design of enantiomerically pure materials, which can enhance the efficiency and stability of the devices. Therefore, the development of chiral PDI-based materials through side chain engineering represents an exciting avenue for improving the performance of OPV devices.

In this doctoral thesis, I present a comprehensive study on side chain engineering in the chirality of PDI-based monomers. I explore the effects of different types of chiral side chains on the optical and electronic properties of PDIs and investigate the

impact of chirality on the performance of OFET devices. Specifically, I investigate the synthesis and characterization of a range of chiral PDIs with different side chain designs and evaluate their stacking manners related to chirality. I also study the underlying mechanisms that govern the optical and electronic properties of chiral PDIs through a combination of experimental and theoretical techniques.

First, the concept of chirality and its importance in organic materials is highlighted, and a detailed discussion of the different side chain designs that have been used to modify the properties of PDIs, including alkyl, aromatic, and chiral side chains is provided. Then, the impact of side chain engineering on the optical and electronic properties of PDIs and the effect of chirality is discussed.

Overall, I aim to contribute to the development of chiral PDI-based materials through side chain engineering, and highlight the critical role of substituted side chains in the relationships among structure, supramolecular chirality, and device performance.

4.2. Experimental Section

4.2.1. Synthesis of asymmetric PDI-based chiral molecules

For the synthesis of a set of asymmetric PDI-based chiral molecules, all chemicals were used as received without any further purification : perylene-3,4,9,10-tetracarboxylic acid dianhydride (PTCDA, TCI, 98%), n-Octylamine (DAEJUNG, >99.5%), methanol anhydrous (Sigma Aldrich, 99.8%), ethanol (DAEJUNG, >94.5), chloroform anhydrous (Sigma Aldrich, >99%), R-(+)-1-Phenylethylamine (TCI, >99%), (R)-(-)-1-Cyclohexylethylamine (Sigma Aldrich, 98%), (R)-1-(2-Naphthyl)ethylamine (TCI, >98%), S-(-)-1-Phenylethylamine (TCI, >98%), (S)-(-)-2-Phenyl-1-Propylamine (Angene, 97%), (S)-(+)-1-Cyclohexylethylamine (Sigma Aldrich, 98%), (S)-1-(2-Naphthyl)ethyllamine (TCI, >98%), imidazole (SAMCHUN, >99.5%).

For mono-substituted PDI, PTCDA (784.64 mg, 2 mmol) and n-octylamine (3.707 g, 20 mmol) were mixed in 80 mL of methanol and refluxed for 7 h. The resulting mixture was cooled to room temperature and acidified by 20 mL concentrated HCl. After stirring overnight, the resulting red solid was collected by vacuum filtration through a 0.45 μm membrane filter. The solid was washed thoroughly with ethanol and distilled water until the pH of the washings turned neutral. Then the raw product containing was used directly for the following reactions.

The mixture containing mono-substituted PDI and chiral monomer (R-(+)-1-Phenylethylamine , (R)-(-)-1-Cyclohexylethylamine, (R)-1-(2-Naphthyl)ethyl amine , S-(-)-1-Phenylethylamine, (S)-(+)-1-Cyclohexylethylamine , (S)-1-(2-Naphthyl)ethylamine) and imidazole (20 g) were heated to 145 °C and stirred for 8 h under N_2. The resulting mixture was cooled to room temperature and dispersed in 25 mL of ethanol, followed by addition of 30 mL of concentrated HCl. After stirring overnight, the resulting red solid was collected by vacuum filtration through a 0.45 μm membrane filter, followed by thoroughly washing with ethanol and distilled

water. The raw product was purified by column chromatography (silica, hexane:ethylacetate=3:1, chloroform: ethylacetate=30:1) to afford compound (R)-1-asy, (R)-1-asyCH, (R)-1-asyNT, (S)-1-asy, (S)-1-asyCH, and (S)-1-asyNT.

4.2.2. Synthesis of symmetric PDI-based chiral molecules and nanowires

For the synthesis of a set of symmetric PDI-based chiral molecules, all chemicals were used as received without any further purification : same materials in 4.2.1. (R)-2-Phenyl-1-Propylamine and (S)-(-)-2-Phenyl-1-Propylamine (Angene, 97%) were added to synthesize (R)-2-sym and (S)-2-sym, respectively. In the synthesis process, PTCDA and chiral molecules were added to imidazole (20g) and were heated under N2 for 1h at 160°C. When the mixture cooled to 90°C, ethanol (200mL) and 2N HCl (400mL) were subsequently added and stirred for 1h to form the precipitate. Then, the mixture was filtered, washed with DI water, and dried under vacuum overnight. The crude product was purified by column chromatography (silica, chloroform: ethylacetate=30:1) to afford (R)-1-sym, (R)-1-symCH, (R)-1-symNT, (R)-2-sym, (S)-1-sym, (S)-1-symCH, (S)-1-symNT, (S)-2-sym.

For the formation of PDI nanowires, a non-solvent-mediated recrystallization method was employed. Nonsolvent methanol was injected into a chloroform solution of PDI-monomer solutions (all 1mg mL^{-1}). After shaking for a few seconds, the solution was kept overnight to form NWs. Then, the mixture was filtered under a vacuum with a porous anodized aluminum oxide (AAO) membrane and dispersed in ethanol.

4.2.3. Thin-Film Microstructure Analyses

Samples for thin-film microstructure analyses were prepared by thermal evaporation. Tapping-mode atomic force microscopy were conducted to investigate the thin-film morphology and roughness.

4.2.4. Structural Characterizations

The morphologies and microstructures of the nanowires were inspected by scanning electron microscopy (FE-SEM). UV-vis absorption spectra of the samples were obtained by a UV-vis spectrometer with quartz cells. 1H-NMR spectrum were recorded on a 300 MHz Bruker spectrometer. CD spectra were recorded using a J-815 (JASCO).

4.2.5. Molecular Dynamics (MD)

MD simulations for self-assembly of the PDI molecules were carried out by Chanui Park from Pf. Won Bo Lee's lab (Theroetical and Computational Soft Matters Laboratory) in Seoul National University. The simulations were conducted using the GROMACS simulation package with the OPLS-AA force field. For each type of the PDI molecules, an initial configuration was generated by randomly packing 50 PDI molecules and 5000 methanol molecules in a cubic box with periodic boundary conditions. An energy minimization run was conducted by the steepest descent algorithm. To relax the bulk system, two consecutive equilibration runs followed under the NPT ensemble with the Berendsen barostat for 0.1 ns, and with the Parrinello-Rahman barostat for 5 ns, under 1 atm with isotropic pressure coupling for both runs. After relaxing the systems, a production run was carried out under the NVT ensemble for 50 ns, and trajectory data were extracted every 10 ps. For the equilibration runs and the production run, the V-rescale thermostat was applied for temperature coupling at 298 K. With the trajectory data, we calculated the center of mass (COM) distance, COM vertical distance, plane angle, sliding angle and offset

angle, which could exhibit the stacking manners of the two adjacent PDI molecules in a self-assembly process.

4.3. Results & Discussion

4.3.1. Effect of the spacer length on chirality and stacking manner

Π-conjugated chiral molecules based on a perylene core bearing a point chirality, (R)-1-sym and (R)-2-sym were synthesized from PTCDA, following the aforementioned synthetic steps in **Figure 4.1**. All of these homochiral PDI molecules can be well solubilized in $CHCl_3$ as monomers with a concentration of 0.1mM. UV-vis absorption spectra of the PDI molecules show the typical monomeric Π-Π transition band with three resolved peaks at 459, 489, 525 nm, respectively, denoted as 0-0, 0-1, and 0-2 electronic transitions. Aggregation of these chiral (R)-1-sym and R-2-sym NWs via Π-Π interactions were fabricated using non-solvent mediated recrystallization from CF/methanol (MeOH) systems. The limited solubility of two monomers under these conditions induced self-assembly into 1D NWs. Characterization of the NW morphology was performed using scanning electron microscope (SEM) as in **Figure 4.2**.

While R-1-sym and S-1-sym showed a nanofibril structure, R-2-sym and S-2-sym showed a combination of helical nanowires and nanosheet. From **Figure 4.2**, helical nanowires seem to emerge from the edge of the nanosheets. R-2-sym shows a left-handed M helical structure, while S-2-sym shows a right-handed P helical structure.

CD spectroscopy is a well-established method for investigating molecular chirality through the differential absorption of left and right circularly polarized light. CD features are highly sensitive to chromophores and molecular packing, making it an ideal tool for monitoring self-assembly processes and investigating the formation dynamics of chiral nanostructures. In this study, CD spectra in **Figure 4.3** were acquired to examine the influence of spacer length on the chirality of R-1-sym and R-2-sym in both their monomeric and aggregated states. As in **Figure 4.3**a,b, slight CD signals were observed below 400 nm using a solution of R-1-sym and R-2-sym dissolved in CF (10^{-4} M). Both monomers show a negative peak around 375 nm and

a positive peak around 320 nm. CD peaks are generally now observed if the molecules do not contain a chromophore or if the absorption band is outside the wavelength region of the spectrometer. Therefore, we hypothesize that the CD peaks of dilute monomers below 400 nm are related to the chromophoric phenyl substituent. Thus, the two solutions did not show any clear difference in the range of 300-400 nm, implying that the length of the spacer does not have a clear impact on point chirality. Weak CD signals were observed in the range of over 400nm, indicating that chirality was not transferred from the chiral substituents to the PDI core. In contrast with the monomers, the CD spectrum of NWs exhibited remarkably different supramolecular chirality as in **Figure 4.3**c. For R-1-sym NWs, CD spectrum exhibited a bisignated Cotton effect with two main negative peaks at 572 nm and 453 nm, and two main positive peaks at 409 nm and 355 nm. R-2-sym NWs showed a CD inversion of R-1-sym NWs, indicating different intermolecular interactions between the molecules. Intriguingly, chirality of R-2-sym were amplified as double as R-1-sym. This is due to helically stacked R-2-sym molecules, which had a favorable stacking distance, and a larger favorable absorbance orientation, leading to amplified difference between LCPL and RCPL. In the monomeric state, chirality originates from intramolecular interactions. After self-assembly, both intra- and intermolecular interactions contribute to the supramolecular chirality of aggregated NWs, which amplifies the intensity of the CD peaks, showing that the point chirality from the chiral pendent has been successfully transferred to the PDI backbone.

We evaluated the electronic performance of our PDI derivatives as a function of the spacer of the chiral pendent. Bottom gate top contact OFETs were fabricated via thermal evaporation of the PDI molecules. A heavily doped n-type Si substrate and a 300 nm SiO_2 layer were used as the gate electrode and gate dielectric layer, respectively. Gold shadow masks were used to deposit gold source/drain electrodes. **Figure 4.4** illustrates the typical charge transfer characteristics of R-1-sym and R-2-sym based OFETs. Table 4.1 summarizes the performance of these devices, in which

the field-effect mobility was calculated in the saturation regime using the following equation:

$$I_D = \frac{W}{2L} C_i \mu (V_G - V_T)^2$$

Where I_D is the drain-source current, W and L are the channel width and length, respectively, C_i is the dielectric capacitance per unit area, μ is the field-effect mobility, V_G is the gate-source voltage, and V_T is the threshold voltage.

To investigate the electrical performance of R-1-sym and R-2-sym, average electron mobilities were obtained for at least ten devices. R-2-sym exhibited excellent n-type characteristics with max mobility of 9.11×10^{-2} $cm^2V^{-1}s^{-1}$. R-1-sym showed approximately half of R-2-sym, with max mobility of 4.98×10^{-2} $cm^2V^{-1}s^{-1}$. This difference is due to the parallel stacking of R-2-sym molecules during self-assembly process, which is possible due to the free space made by the additional methylene group. In contrast, R-1-sym has only one methylene group, which makes the phenyl group point upwards, disrupting the stacking between PDI molecules. This stacking is characterized via AFM images, and **Figure 4.5** shows that R-2-sym had a bigger grain size compared to R-1-sym, leading to larger roughness of 5.2 nm.

The effect of the spacer length on chirality and electron mobility was investigated through MD simulations. To figure out the stacked manner of the neighboring stacked PDI molecules, we explored four factors : plane angle (angle between normal vectors of a PDI pair), Center of Mass (COM) vertical distance, sliding angle (angle between normal vector and COM-COM vector), and offset angle (angle between N-N vectors of a PDI pair). (Still in analysis)

4.3.2. Effect of conjugation length and alkyl chain on chirality and stacking manner

Chiral PDI molecules, as shown in **Figure 4.6**, featuring a point chirality at imide positions were synthesized from PTCDA through a 1-step reaction and denoted as R/S-1-sym, R/S-1-symCH, R/S-1-symNT, respectively. Asymmetric PDI molecules were also synthesized to investigate the effect of alkyl chain on molecular stacking, All of these homochiral PDI molecules can be dissolved in chloroform with a concentration of 0.1 mM. The two imide nitrogen atoms correspond to π orbital nodes, and substitution at this position with various side chains does not change the electronic structure of the PDI molecule. Therefore, the UV-vis absorption spectra of monomeric PDI molecules in chloroform (CF) are similar as in **Figure 4.7**, with three pronounce peaks at 526 nm, 490 nm, and 459 nm and a shoulder peak around 430 nm, which correspond to 0-0, 0-1, 0-2, and 0-3 electronic transitions, respectively. However, dramatic changes in these absorbance spectra were observed after self-assembly into PDI nanowires. The absorbance spectra of NWs exhibited red-shifted peaks, indicating J aggregate and strong and effective π-π interactions in a cofacial configuration of molecular stacking between the PDI cores. Cyclic voltammetry and density functional theory (DFT) were used to investigate the energy levels of R-1-sym, R-1-symCH, and R-1-symNT. The DFT calculations in **Figure 4.8** show the lowest unoccupied molecular orbital (LUMO) levels for R-1-sym, R-1-symCH, R-1-symNT at -3.56, -3.59, and -3.60 eV. Interestingly, DFT calculations with R-1-symNT show the LUMO and HOMO primarily on the PDI core and aromatic naphthalene, respectively, which may be related to the strong electron-donating ability of naphthalene. In contrast, both the LUMO and HOMO of both R-1-sym and R-1-symCH appear primarily on the PDI core.

CD spectra in **Figure 4.9** were observed for three monomers to investigate the effect of side chain and molecular chirality. In the region of 400-600 nm, the monomers did now show any discernible peaks, indicating that the chirality has not yet been transferred to the PDI core. In the region of 300-400 nm, peaks coming from the chromophoric substituents of point chirality are shown. Interestingly, the

peaks showed a similar manner, with a negative peak at 360 nm and a positive peak at 319 nm, however, in the order of cyclohexane, phenyl, and naphthalene (as the conjugation length of the substituents increased) point chirality increased. To elucidate that this point chirality really came from the choromophoric substituents, point chirality of the asymmetric counterparts, R-1-asyCH, R-1-asy and R-1-asyNT are shown. Since the asymmetric monomers have only one point chirality region on one substituted side and a long alkyl chain on the other, their point chirality in the 300-400 nm were approximately half of that in the symmetric molecules. However, their chirality increased in the same order of symmetric counterparts.

In order to characterize the CD property of the molecules, time-dependent density functional theory (TD-DFT) calculation was performed at the CAM-B3LYP/def2-TZVP level with chloroform as the solvent state. In the region of 300-400 nm transition state, R-1-symNT had the transition electric dipole moment (TEDM) of 0.0448, and R-1-sym then R-1-symCH followed next, with TEDM of 0.0216, and 0.0166, respectively. (See **Table 4.1**) Rotational strength is related to chirality because it arises due to the molecule's ability to interact differently with left and right circularly polarized light. So, the magnitude of this difference depends on the extent of chirality of the molecule. It is also calculated through dot product of TEDM and TMDM, and the results showed that R-1-symNT showed the biggest strength of 0.0165. (**Figure 4.10**) This is due to the different localization of HOMO and LUMO in R-1-symNT. Since HOMO and LUMO are located on different parts of a molecule, this results in a larger spatial separation between the electron density distributions associated with the two states. This can lead to a larger overlap integral and therefore a larger TDM, which in turn can result in a stronger rotational transition and increased rotational strength.

PDI NWs were fabricated following the non-solvent-mediated recrystallization method shown in 4.2.2, and the CD spectroscopy of self-assembly of R-1-sym, R-1-symCH, and R-1-symNT showed a different manner, as illustrated in **Figure 4.11**.

When the molecules are supramolecular-assembled, the point chirality is no longer a dominant factor in CD spectroscopy; instead, it only works as a driving force to direct the stacking of the monomers and the stacking degree or handedness from whole stacked molecules play an important role in determining the chirality. R/S-1-symCH, R/S-1-sym, R/S-1-symNT showed a mirror image between enantiomers, and the peaks in 400-600 nm showed that the chiral transcription were successful from the chiral substituents to the PDI core. CD peaks from 300-400 nm show absolutely different manners, and they even show an inverted sign, opposite to that of monomers, implying that point chirality is no longer a considerable factor. Since both intra- and intermolecular interactions contribute to the supramolecular chirality of aggregated NWs, we need to take a deeper look at how the molecules are assembled and how the PDI cores are Π-Π stacked under the effect of the side chains.

Characterizations of NW morphologies were performed using OM and SEM. OM image in **Figure 4.12** shows that R-1-symCH nanowires with no conjugation in the side chain exhibit long nanofibers (>300 μm) with an aspect ratio over 50. In contrast, molecules with conjugated side length on both sides show much shorter nanorods. R-1-sym exhibits nanorods with a length of 20-30 μm while R-1-symNT is shorter than 10 μm. (S) enantiomers show a similar trend, with smaller aspect ratio in both S-1-sym and S-1-symNT. In SEM images, as shown in **Figure 4.13**, R-1-symNT shows chopped off nanowires of a length of 2-3 μm, much shorter than cyclohexane and phenyl counterparts. Molecular packing was determined from powder X-ray diffraction analyses. The different peak positions in these data are indicative of different crystal structures. From d-spacing calculations, R-1-symCH shows peaks at 24.6° and 25.3°, corresponding to 3.61 and 3.51 Å, respectively, which are typical for Π-Π stacking distances. R-1-sym shows a similar pattern, with peaks at 24.8°, corresponding to 3.59 Å. However, R-1-symNT, due to its low crystallinity, does not show discernible peak, compared to R-1-sym and R-1-symCH, showing that Π-Π stacking is not extended much.

To investigate the charge transport of PDI self-assembly, OFETs with bottom-gate top-contact configuration were fabricated. Since PDI based NWs had a large range of mobility due to contact issue, thermally evaporated self-assembly films were used instead for comparing the mobilities of symmetric PDIs. **Figure 4.14** illustrates the typical transfer characteristics of R-1-sym, R-1-symCH, and R-1-symNT based OFETs. Due to their different stacking manners, the three films exhibited different max mobility of 8.7×10^{-2}, 4.98×10^{-2}, and 2.13×10^{-2} $cm^2\ V^{-1}\ s^{-1}$ in the saturation regime, respectively. The topography of evaporated films was investigated through AFM. In **Figure 4.15**, R-1-symCH with best crystallinity showed largest grain size, and R-1-sym followed next, with similar roughness of 3.5 nm. In contrast, R-1-symNT exhibited the smallest grain size, showing the disordered stacking between the molecules and due to its inferior packing, larger roughness of 20.97 nm was found.

Asymmetric PDI molecules with alkyl chain on one side showed facilitated better stacking compared to their symmetric counterparts. Octyl chains are not long compared to PDI cores and are more flexible and have a higher propensity for intermolecular interactions, such as Van der Waals forces, which promote stacking. Phenyl or naphthalene groups on both sides are more rigid and with a higher electron density, so they disrupt stacking. SEM images of R-1-asyCH, R-1-asy, and R-1-asyNT in **Figure 4.16** showed that these three nanowires had a much better stacking structure than the symmetric ones. In AFM images (See **Figure 4.17**), R-1-asyCH shows similar fibril structures as in R-1-symCH, while molecules that have conjugated systems like R-1-asy and R-1-asyNT show bigger grains compared to R-1-sym and R-1-symNT. R-1-asyNT showed the biggest change, in which grains were interconnected leading to smaller roughness.

Owing to their enhanced stacked structures, charge transport mobilities were also enhanced compared to their symmetric counterparts. **Figure 4.18** shows that R-1-asyCH exhibited the biggest electron mobility of 1.88×10^{-1} $cm^2\ V^{-1}\ s^{-1}$ which was

more than double of R-1-symCH. R-1-asy and R-1-asyNT also showed mobilities as nearly double as R-1-sym and R-1-symNT, with mobilities of 8.07×10^{-2} and 4.87×10^{-2} $cm^2 V^{-1} s^{-1}$, respectively.

These results show that flexible alkyl chain provides additional space around the PDI core, affecting their abilities to stack more efficiently in the solid-state.

4.4. Conclusion

In conclusion, we have successfully synthesized and characterized a series of chiral PDI derivatives bearing a chiral pendant with various spacer lengths. We also synthesized chiral PDI molecules with various chiral pendants in asymmetric and symmetric positions. The chirality from the chiral pendant was successfully transferred to the PDI core after self-assembly, resulting in the formation of chiral nanostructures. The chirality of the NWs was found to be dependent on the intermolecular stacking manner, and the chirality of R-2-sym was amplified compared to R-1-sym due to helical stacking. TD-DFT calculations showed that the magnitude of rotational strength, related to chirality, depends on the extent of chirality of the molecule, and R-1-symNT showed the biggest strength. The electronic properties of the PDI derivatives were also evaluated by fabricating OFETs. R-2-sym exhibited excellent n-type characteristics with high mobility, and asymmetric PDI molecules showed enhanced charge transport compared to symmetric counterparts. These findings provide insights into the design and synthesis of chiral PDI molecules and their CD spectroscopy, which could be useful for the development of novel functional materials.

4.5. References

(1) Shirakawa, H.; Louis, E. J.; MacDiarmid, A. G.; Chiang, C. K.; Heeger, A. J. Synthesis of Electrically Conducting Organic Polymers: Halogen Derivatives of Polyacetylene, (Ch). *J. Chem. Soc., Chem. Commun.* **1977**, 578-580.

(2) Hembury, G. A.; Borovkov, V. V.; Inoue, Y. Chirality-Sensing Supramolecular Systems. *Chem. Rev.* **2008,** *108*, 1-73.

(3) Prins, L. J.; Timmerman, P.; Reinhoudt, D. N. Amplification of Chirality: The "Sergeants and Soldiers" Principle Applied to Dynamic Hydrogen-Bonded Assemblies. *J. Am. Chem. Soc.* **2001,** *123*, 10153-10163.

(4) Li, W.; Coppens, Z. J.; Besteiro, L. V.; Wang, W.; Govorov, A. O.; Valentine, J. Circularly Polarized Light Detection with Hot Electrons in Chiral Plasmonic Metamaterials. *Nat. Commun.* **2015,** *6*, 8379.

(5) Shang, X.; Song, I.; Ohtsu, H.; Tong, J.; Zhang, H.; Oh, J. H. Morphogenesis and Optoelectronic Properties of Supramolecular Assemblies of Chiral Perylene Diimides in a Binary Solvent System. *Sci. Rep.* **2017,** *7*, 5508.

(6) Shang, X.; Song, I.; Lee, J. H.; Choi, W.; Ahn, J.; Ohtsu, H.; Kim, J. C.; Koo, J. Y.; Kwak, S. K.; Oh, J. H. Surface-Doped Quasi-2D Chiral Organic Single Crystals for Chiroptical Sensing. *ACS Nano* **2020,** *14*, 14146-14156.

(7) Bredas J.-L.; Beljonne D.; Coropceanu, V.; Cornil, J. Charge-Transfer and Energy-Transfer Processes in π-Conjugated Oligomers and Polymers: A Molecular Picture, *Chem. Rev.* **2004**, *104*, 4971-5003.

(8) Han, H.; Lee, Y. J.; Kyhm, J.; Jeong, J. S.; Han, J.-H.; Yang, M. K.; Lee, K. M.; Choi, Y.; Yoon, T.-H.; Ju, H.; Ahn, S.-k.; Lim, J. A. High-Performance Circularly Polarized Light-Sensing near-Infrared Organic Phototransistors for Optoelectronic Cryptographic Primitives. *Adv. Funct. Mater.* **2020,** *30*, 2006236.

(9) Jiang, W.; Li, Y.; Yue, W.; Zhen, Y.; Qu, J.; Wang, Z. One-Pot Facile Synthesis of Pyridyl Annelated Perylene Bisimides. *Org. Lett.* **2010,** *12*, 228-231.

(10) Lee, C.; Yang, W.; Parr, R. G. Development of the Colle-Salvetti Correlation-Energy Formula into a Functional of the Electron Density. *Phys. Rev. B* **1988,** *37*, 785-789.

(11) Huang, J.; Du, J.; Cevher, Z.; Ren, Y.; Wu, X.; Chu, Y. Printable and Flexible Phototransistors Based on Blend of Organic Semiconductor and Biopolymer. *Adv. Funct. Mater.* **2017,** *27*, 1604163.

(12) Shang, X.; Song, I.; Ohtsu, H.; Lee, Y. H.; Zhao, T.; Kojima, T.; Jung, J. H.; Kawano, M.; Oh, J. H. Supramolecular Nanostructures of Chiral Perylene Diimides with Amplified Chirality for High-Performance Chiroptical Sensing. *Adv. Mater.* **2017,** *29*, 1605828.

(13) Shang, X.; Song, I.; Ohtsu, H.; Tong, J.; Zhang, H.; Oh, J. H. Morphogenesis and Optoelectronic Properties of Supramolecular Assemblies of Chiral Perylene Diimides in a Binary Solvent System. *Sci. Rep.* **2017,** *7*, 5508.

(14) Lee, W.-Y.; Oh, J. H.; Suraru, S.-L.; Chen, W.-C.; Würthner, F.; Bao, Z. High-Mobility Air-Stable Solution-Shear-Processed N-Channel Organic Transistors Based on Core-Chlorinated Naphthalene Diimides. *Adv. Funct. Mater.* **2011,** *21*, 4173-4181.

(15) Oh, J. H.; Sun, Y.-S.; Schmidt, R.; Toney, M. F.; Nordlund, D.; Könemann, M.; Würthner, F.; Bao, Z. Interplay between Energetic and Kinetic Factors on the Ambient Stability of N-Channel Organic Transistors Based on Perylene Diimide Derivatives. *Chem. Mater.* **2009,** *21*, 5508-5518.

(16) Weitz, R. T.; Amsharov, K.; Zschieschang, U.; Villas, E. B.; Goswami, D. K.; Burghard, M.; Dosch, H.; Jansen, M.; Kern, K.; Klauk, H. Organic N-Channel Transistors Based on Core-Cyanated Perylene Carboxylic Diimide Derivatives. *J. Am. Chem. Soc.* **2008,** *130*, 4637-4645.

(17) Sung, J.; Kim, P.; Fimmel, B.; Würthner, F.; Kim, D. Direct Observation of Ultrafast Coherent Exciton Dynamics in Helical Π-Stacks of Self-Assembled Perylene Bisimides. *Nat. Commun.* **2015,** *6*, 8646.

(18) Kim, N. Y.; Kyhm, J.; Han, H.; Kim, S. J.; Ahn, J.; Hwang, D. K.; Jang, H. W.; Ju, B.-K.; Lim, J. A. Chiroptical-Conjugated Polymer/Chiral Small Molecule Hybrid Thin Films for Circularly Polarized Light-Detecting Heterojunction Devices. *Adv. Funct. Mater.* **2019,** *29*, 1808668.

(19) Xu, L.; Wang, C.; Li, Y.-X.; Xu, X.-H.; Zhou, L.; Liu, N.; Wu, Z.-Q. Crystallization-Driven Asymmetric Helical Assembly of Conjugated Block Copolymers and the Aggregation Induced White-Light Emission and Circularly Polarized Luminescence. *Angew. Chem. Int. Ed.* **2020,** *59*, 16675-16682.

(20) Kim, N. Y.; Kyhm, J.; Han, H.; Kim, S. J.; Ahn, J.; Hwang, D. K.; Jang, H. W.; Ju, B.-K.; Lim, J. A. Chiroptical-Conjugated Polymer/Chiral Small Molecule Hybrid Thin Films for Circularly Polarized Light-Detecting Heterojunction Devices. *Adv. Funct. Mater.* **2019,** *29*, 1808668.

(21) Maity, S.; Bedi, A.; Patil, S. Side-Chain Induced Chirality in Diketopyrrolopyrrole Based Polymers. *J. Polym. Sci.* **2021,** *59*, 3181-3188.

(22) Lee, D.-M.; Song, J.-W.; Lee, Y.-J.; Yu, C.-J.; Kim, J.-H. Control of Circularly Polarized Electroluminescence in Induced Twist Structure of Conjugate Polymer. *Adv. Mater.* **2017,** *29*, 1700907.

(23) Samanta, S. K.; Song, I.; Yoo, J. H.; Oh, J. H. Organic N-Channel Transistors Based on [1]Benzothieno[3,2-B]Benzothiophene–Rylene Diimide Donor–Acceptor Conjugated Polymers. *ACS Appl. Mater. Interfaces* **2018,** *10*, 32444-32453.

(24) Di Nuzzo, D.; Kulkarni, C.; Zhao, B.; Smolinsky, E.; Tassinari, F.; Meskers, S. C. J.; Naaman, R.; Meijer, E. W.; Friend, R. H. High Circular Polarization of Electroluminescence Achieved Via Self-Assembly of a Light-Emitting Chiral Conjugated Polymer into Multidomain Cholesteric Films. *ACS Nano* **2017,** *11*, 12713-12722.

(25) Wan, L.; Wade, J.; Salerno, F.; Arteaga, O.; Laidlaw, B.; Wang, X.; Penfold, T.; Fuchter, M. J.; Campbell, A. J. Inverting the Handedness of Circularly Polarized

Luminescence from Light-Emitting Polymers Using Film Thickness. *ACS Nano* **2019,** *13*, 8099-8105.

(26) Ma, J.; Fang, C.; Chen, C.; Jin, L.; Wang, J.; Wang, S.; Tang, J.; Li, D. Chiral 2d Perovskites with a High Degree of Circularly Polarized Photoluminescence. *ACS Nano* **2019,** *13*, 3659-3665.

(27) Armin, A.; Chen, Z.; Jin, Y.; Zhang, K.; Huang, F.; Shoaee, S. A Shockley-Type Polymer: Fullerene Solar Cell. *Adv. Energy Mater.* **2018,** *8*, 1701450.

4.6. Figures and Tables

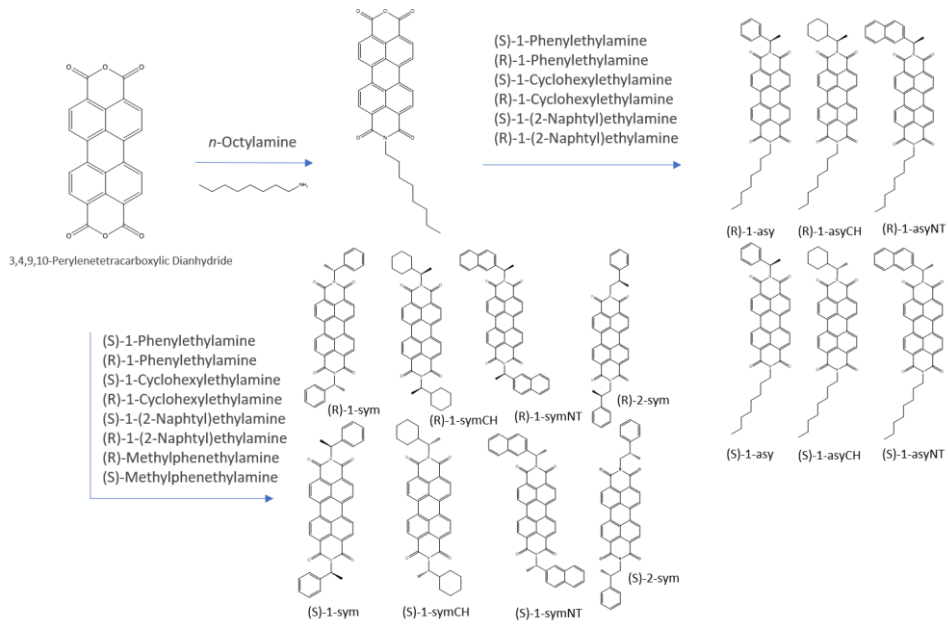

Figure 4.1. Schematic illustration of the synthetic procedures of chiral PDI molecules starting from PTCDA.

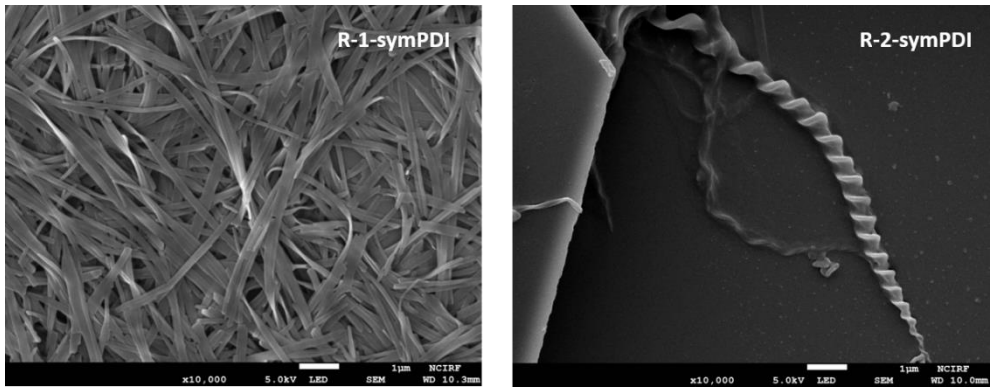

Figure 4.2. SEM images of R-1-symPDI and R-2-symPDI.

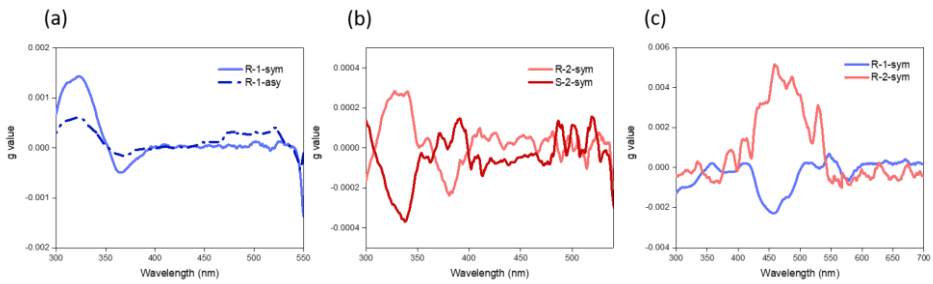

Figure 4.3. CD spectroscopy of the PDI molecules in monomeric state. All molecules were dissolved in CF (10^{-4} M). (a) Monomer chirality of R-1-sym (light blue). (b) Monomer chirality of R-2-sym and S-2-sym. (c) Supramolecular chirality of R-1-sym and R-2-sym.

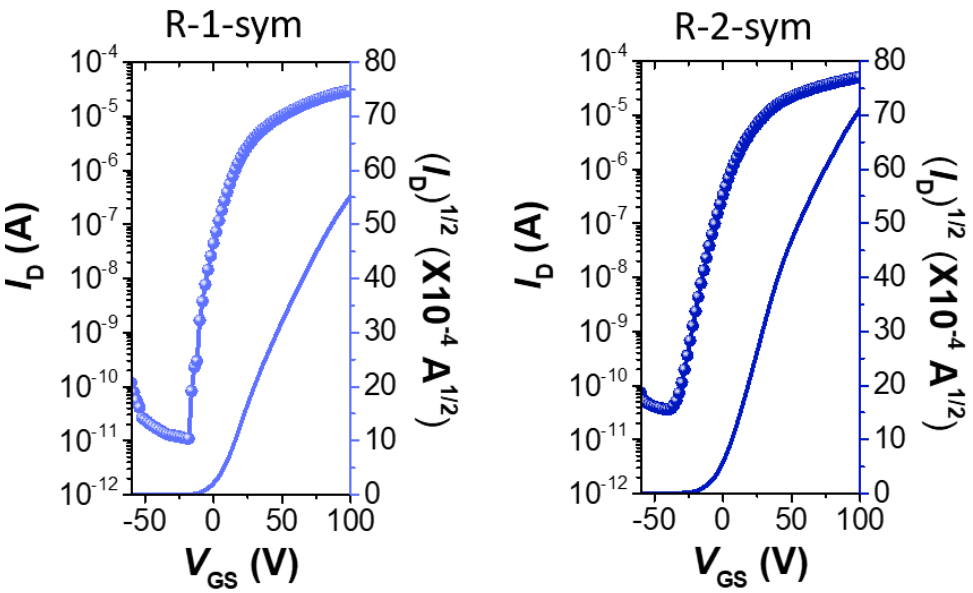

Figure 4.4. Transfer characteristics of OFETs fabricated with R-1-sym (left) and R-2-sym (right), via thermal evaporation.

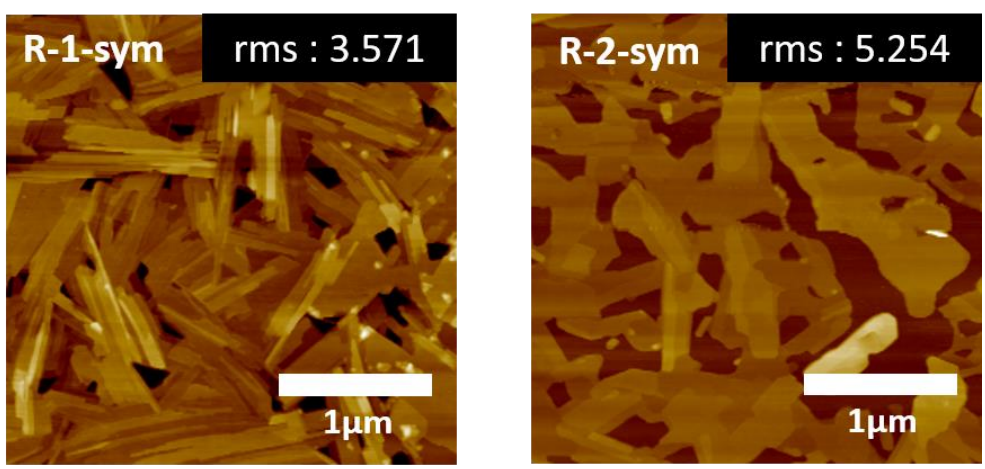

Figure 4.5. AFM images of thermally evaporated films of R-1-sym (left) and R-2-sym (right). Scale bar=1μm.

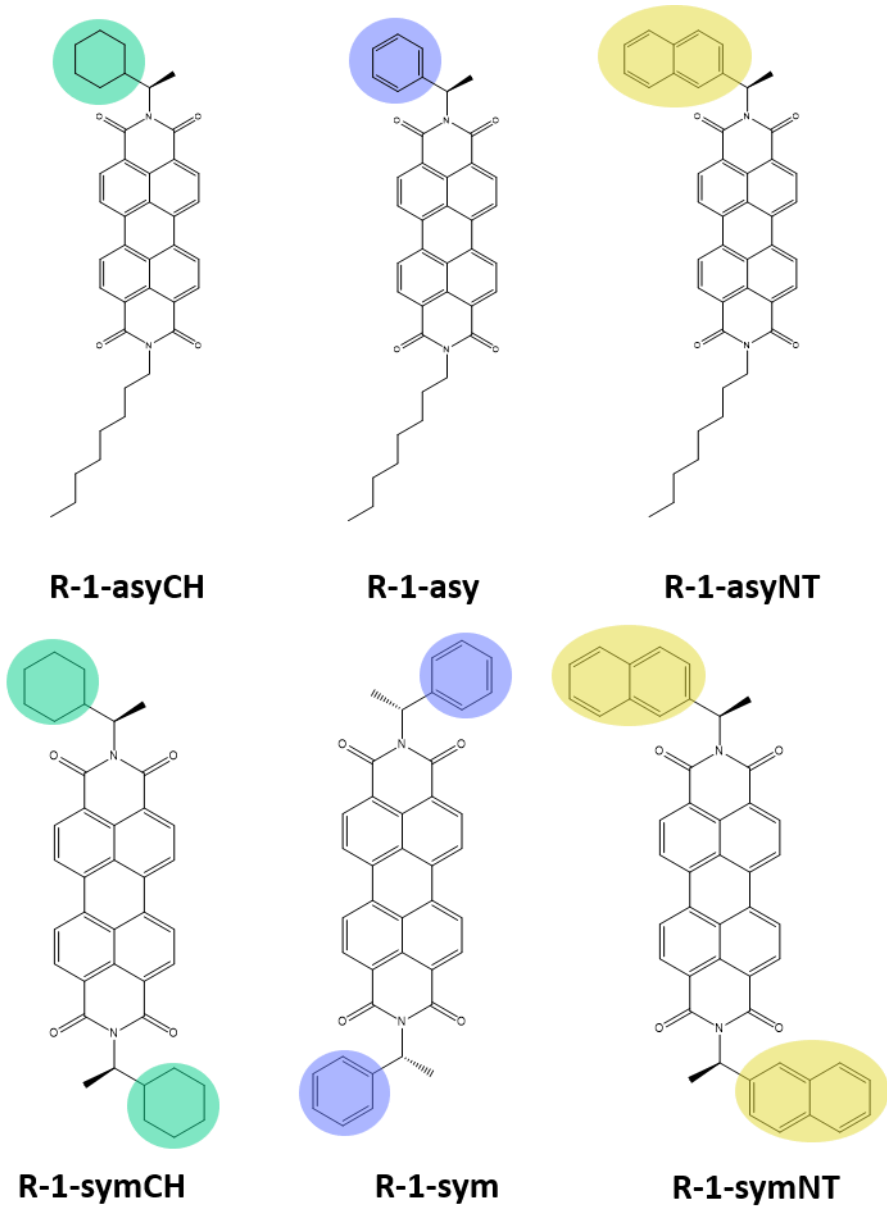

Figure 4.6. Molecular design of asymmetric and symmetric chiral PDI molecules. Colored circles indicate the point chirality of each monomer. (green : cyclohexane, blue : phenyl, yellow : naphthalene).

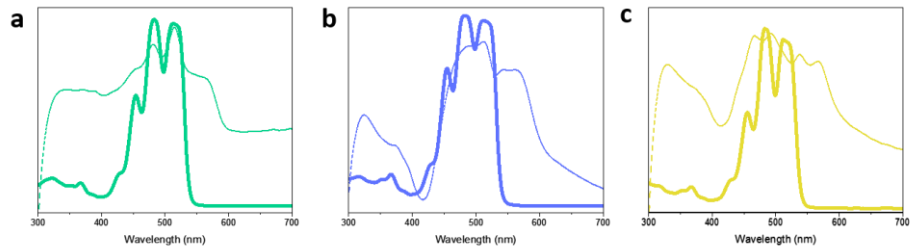

Figure 4.7. Normalized UV-vis absorption spectra of symmetric PDI molecules. Solid lines show monomer state, and dashed lines show NW state. (a) R-1-symCH, (b) R-1-sym, (c) R-1-symNT.

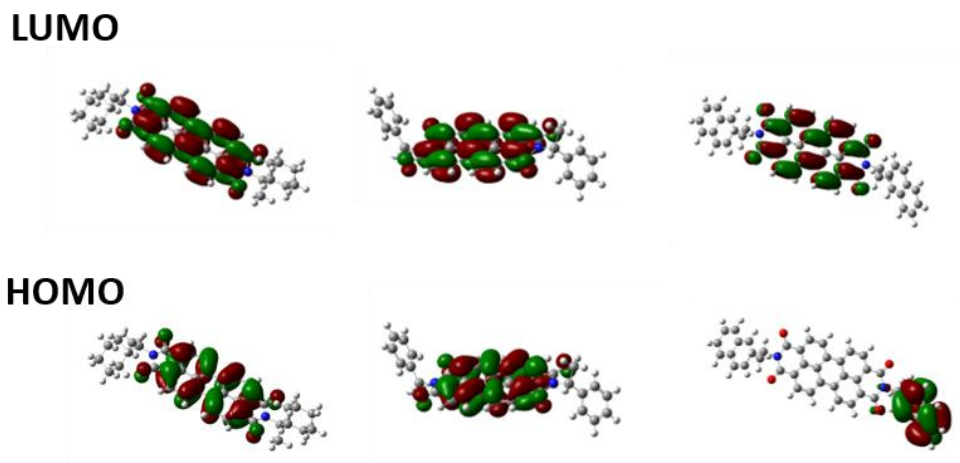

Figure 4.8. DFT calculations (LUMO, HOMO) of R-1-symCH (left), R-1-sym (middle), and R-1-symNT (right).

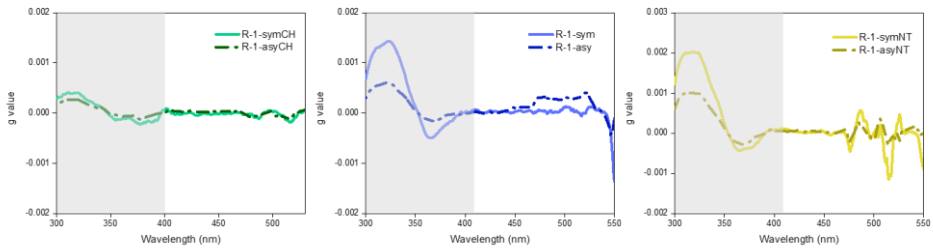

Figure 4.9. Monomer chirality of R-1-symCH/R-1-asyCH, R-1-sym/R-1-asy, R-1-symNT/R-1-asyNT. Symmetric molecules are shown in light solid lines while asymmetric molecules are shown in deep dashed lines.

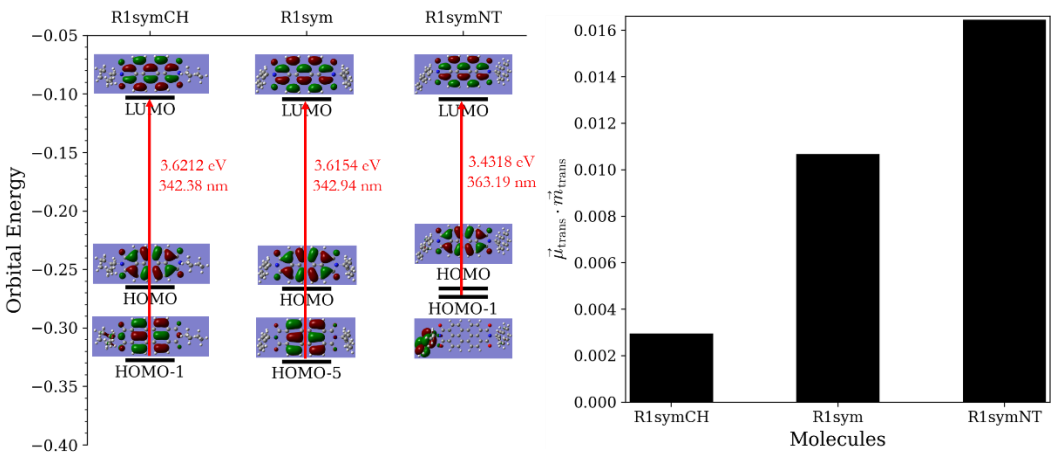

Figure 4.10. Orbital correlation diagram and rotational strength calculated with TD-DFT.

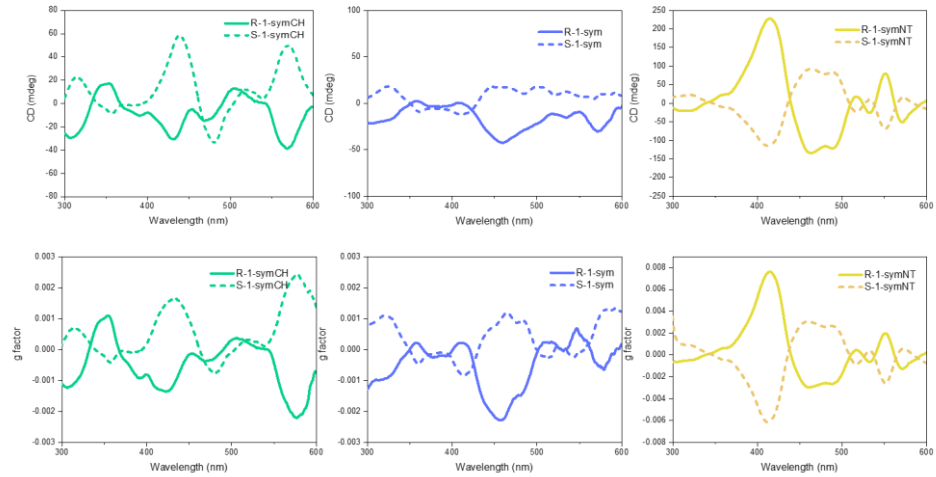

Figure 4.11. NW chirality of symmetric PDI molecules. Solid line : R enantiomers, dashed line : S enantiomers.

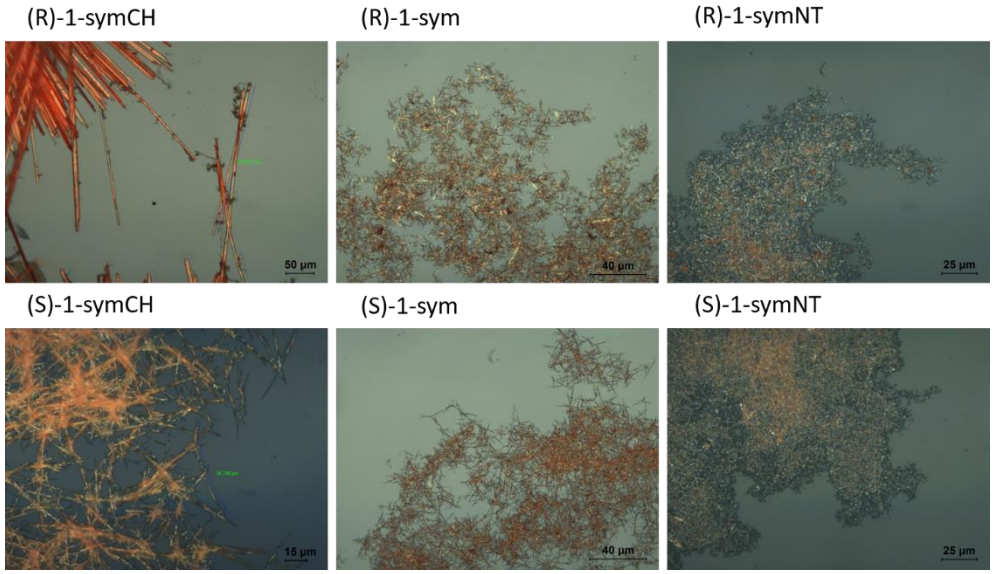

Figure 4.12. OM images of symmetric PDI molecules.

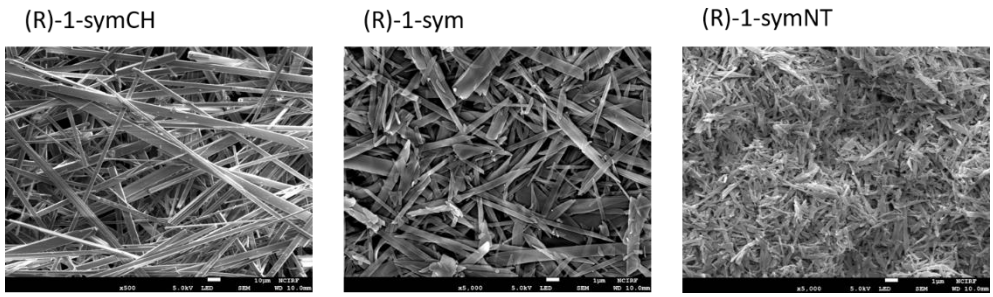

Figure 4.13. SEM images of symmetric PDI molecules.

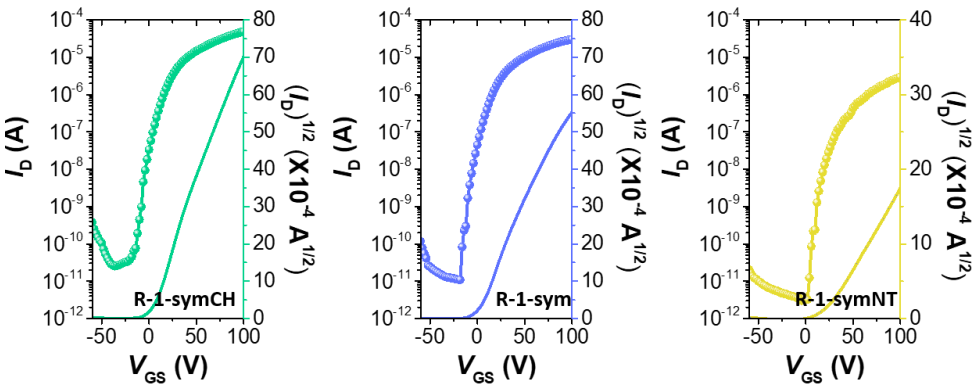

Figure 4.14. Transfer characteristics of symmetric PDI molecules.

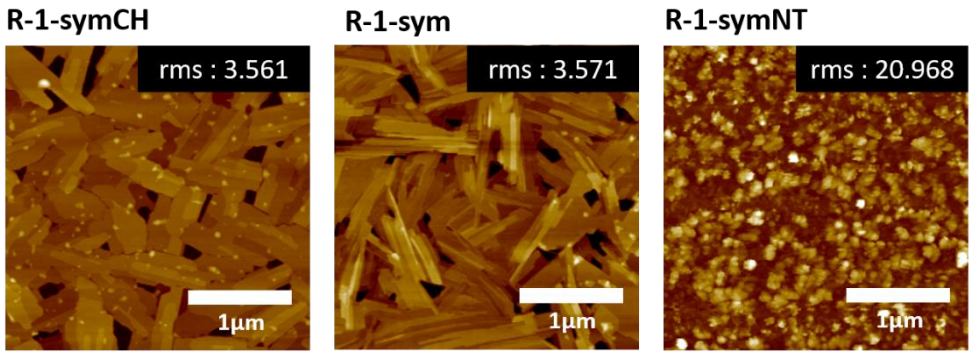

Figure 4.15. AFM images of symmetric PDI molecules. Scale bar = 1μm.

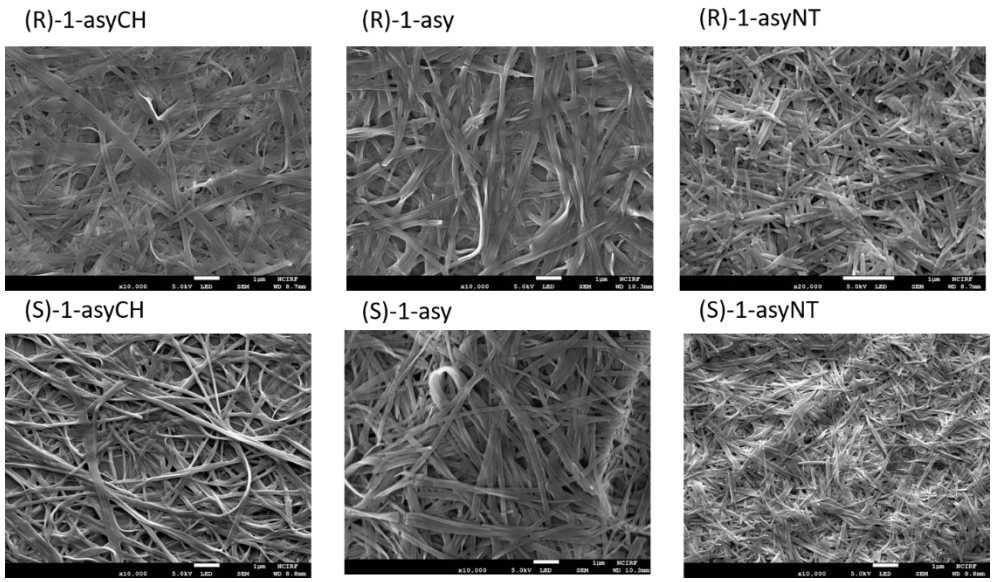

Figure 4.16. SEM images of asymmetric PDI molecules. Top : R enantiomers, bottom : S enantiomers.

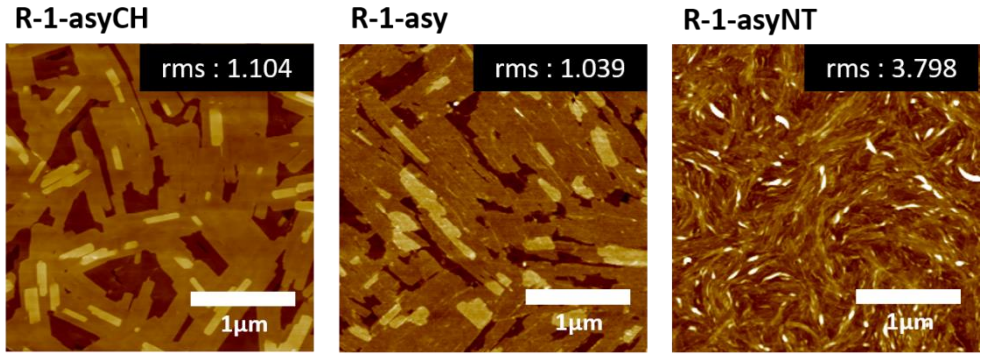

Figure 4.17. AFM images of asymmetric PDI molecules. Scale bar = 1μm.

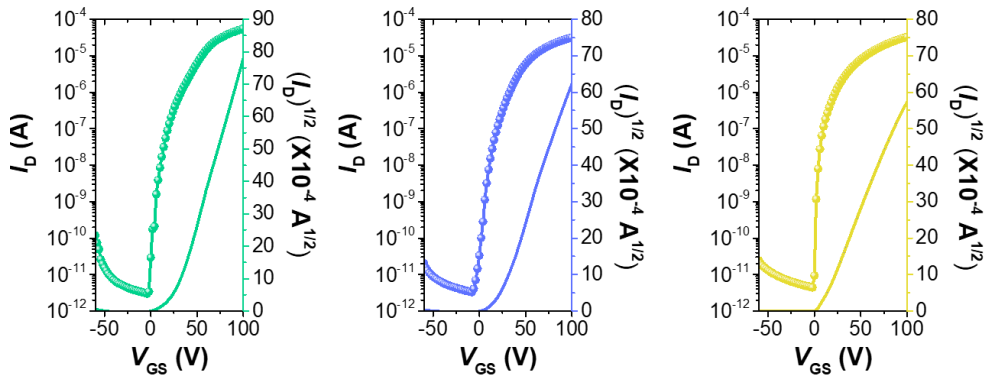

Figure 4.18. Transfer characteristics of asymmetric PDI molecules.

PDI	$\lvert\boldsymbol{\mu}\rvert/\mathrm{au}_{\mathrm{TEDM}}$	$\lvert\boldsymbol{m}\rvert/\mathrm{au}_{\mathrm{TMDM}}$	$\cos\theta_{\boldsymbol{\mu},\boldsymbol{m}}$	$R/(\mathrm{au}_{\mathrm{TEDM}}\cdot\mathrm{au}_{\mathrm{TMDM}})$
R1symCH	0.0166	1.1967	-0.1489	-0.0030
R1sym	0.0216	1.2424	-0.3975	-0.0107
R1symNT	0.0448	0.4545	-0.8080	-0.0165

Table 4.1. TD-DFT calculations of symmetric PDI molecules.

요 약 문

지난 수십 년 동안 유기 전계 효과 트랜지스터의 전하 이동성을 향상시키기 위해 많은 연구가 진행되어 왔다. 최근 유기 트랜지스터 성능이 비정질 실리콘 및 다결정 실리콘 기반 트랜지스터의 성능을 초과한다는 보고에도 불구하고, 유기 반도체는 유기물질의 약한 반 데르 발스 결합으로 인해 종종 이상적이지 않은 작동을 보인다. 이러한 문제점을 해결하기 위해서는 유기 반도체의 전기적 특성과 미세구조 및 가공기술과의 관계를 규명하고, 고성능 유기 반도체 제조를 위한 가이드라인을 개발할 필요가 있다.

공액 고분자는 빛을 흡수/방출하고 전류를 전도할 수 있는 플라스틱의 일종으로, 유기 광전지, 전계효과 트랜지스터, 발광 다이오드, 전자크롬 소자 등 다양한 유기 전자 제품에 사용되어 왔다. 유연하고 인쇄된 전자제품의 등장으로 공액 고분자에 대한 관심이 높아졌고, 그 결과 합성된 공액 고분자의 수가 최근 기하급수적으로 증가했다. 이러한 재료는 향상된 성능을 입증했으며 상용 애플리케이션이 곧 출시될 것으로 보인다. 이러한 성능 향상은 재료 설계, 가공 및 장치 제작에 대한 더 나은 연구를 통해 달성되었다. 공액 폴리머를 설계할 때, 사이드 체인의 선택은 공액 백본의 선택만큼이나 중요하다. 용액공정이 가능한 중합체는 일반적으로 파이결합된 골격과 주변 유연한 사이드체인 두 부분으로 구성된다. 결과 폴리머의 광전자 특성은 대부분의 연구 노력의 초점이 되어온 파이결합 백본에 의해 결정된다. 그러나 사이드 체인 대체물이 수년간 테스트되었음에도 불구하고 사이드 체인은 충분히 연구되지 않았다. 이 박사 논문에서, 이 전략의 중요성에 대해 강조하려 한다.

제 1 장에서는 사이드 체인 엔지니어링, 유기 전자 공학, 전하 수송 및 초분자 키랄성에 대한 기초 정보를 포함하여 연구 배경과 본 논문의 목적에 대한 간략한 개요를 제시한다.

제 2 장에서는 DPP 기반의 소분자와 고분자를 합성하여 OFET 소자에 적용하였다. DPP 단분자에서 실록세인 사이드체인은 최상의 소자 성능을 보였고 포스포네이트 말단 사이드체인은 전하 수송 특성에 부정적인 영향을 미쳤다. DPP 공액 고분자에서 다양한 코모노머가 도입되었고 에지온 패킹, 피브릴 인터칼레이션 네트워크 및 큰 결정성 파이스태킹의 조합으로 인해 두 개의 연속적인 싸이오펜 코모노머가 있는 분자로 제작한 소자가 최고의 전하 수송을 보였다.

제 3 장에서는 칼코제노펜 대응물을 포함한 일련의 작은 갭 DAP 기반 공여체 공중합체를 합성했다. 공중합체들은 단극 p-채널 작동을 보여주었고, 셀레노펜이 들어간 소자는 높은 결정성을 가진 3D 전하-전도 채널의 결과 4.79×10^{-1} cm^2 V^{-1} s^{-1} 까지 최고의 홀 이동성을 보여주었다. 또한 가장 높은 근적외선 광적 특성을 가지고 있어 DAP 기반 공중합체가 NIR 센서에 사용될 가능성이 매우 높다는 것을 보여주었다.

제 4 장에서는 PDI 기반 단량체 세트를 합성하여 1 차원 나노와이어로 자가 조립했다. 구조-키랄성 관계를 탐구하기 위해 키랄 포인트, 키랄 대체물의 유형 및 대칭(한 쪽에만 키랄 펜던트가 있거나 양쪽에 키랄 펜던트가 있는지 여부), 그리고 스페이서의 길이를 변경했다. 준비된 와이어의 원형 이분법 스펙트럼 분석을 통해 키랄성이 증폭된 나선형 와이어에 적층된 분자의 적층 방식을 결정하는 데 스페이서 길이가 중요하다는 것을 알 수 있었다. 또한 컨주게이션 길이가 길어지면 분자 키랄성이 두 배로 증가했지만, 분자 적층이 중요한 결정 요인인 초분자

키랄성은 컨주게이션 길이에 비례하지 않았다. 마지막으로, PDI 코어의 한 쪽에 치환된 알킬 체인은 추가 공간을 마련함으로써 분자의 더 정렬된 적층을 도와 OFET 소자로 제작되었을 때 높은 전자 이동성으로 이어졌다.

주요어: 반도체, 유기 전자 소자, 초분자 키랄성, 사이드체인 조절

학 번: 2019-31012